#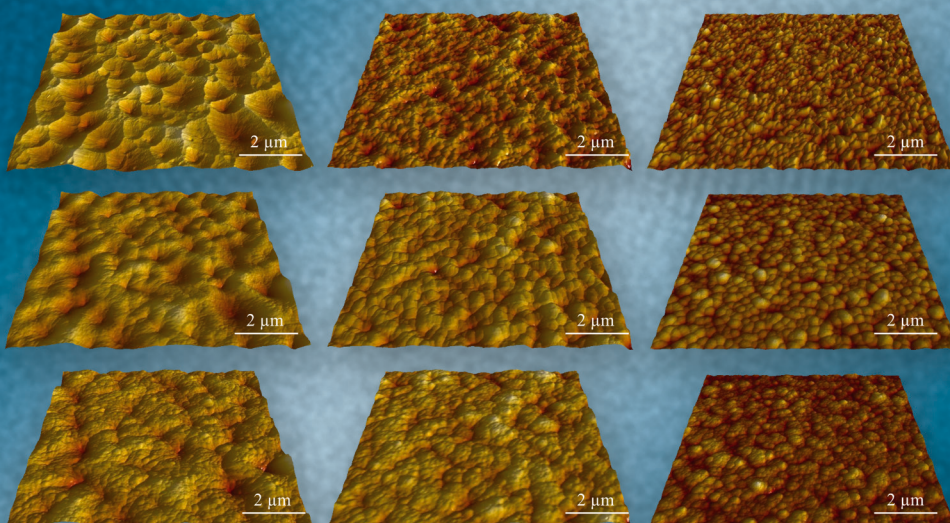 Interface and Topography Optimization for Thin-Film Silicon Solar Cells with Doped Microcrystalline Silicon Oxide Layers

Chao Zhang

JÜLICH
FORSCHUNGSZENTRUM

Interface and Topography Optimization for Thin-Film Silicon Solar Cells with Doped Microcrystalline Silicon Oxide Layers

Chao Zhang

"Calvin & Hobbes" by Bill Watterson

Zusammenfassung

Geringe Kosten und niedriger Materialverbrauch sind die herausragenden Vorzüge von Dünnschicht Silizium Solarzellen. Die zusätzliche Möglichkeit in großem Maßstab zu produzieren, macht diese Technologie zu einer Alternative gegenüber multi- oder monokristallinen Silizium-Solarzellen. Verglichen mit anderen Dünnschichtsolarzellen basierend auf CdTe oder CIGS gibt es wiederum eine weit größere Verfügbarkeit in Bezug auf verwendete Rohstoffe. Darüber hinaus werden bei Dünnschichtsilizium-Solarzellen keine toxischen Elemente eingesetzt. Nichtsdestotrotz befindet sich die Effizienz auf einem niedrigen Niveau. Die Verbesserung der Solarzelleffizienz durch die Verwendung von optisch verbesserten Materialien wie hydrierten mikrokristallinen Siliziumoxiden und eine effiziente Nutzung der Solarzell-Topographie sind Themen der vorliegenden Arbeit. Darüber hinaus werden optische und elektrische Verlustmechanismen in Dünnschichtsilizium-Solarzellen untersucht und diskutiert. Die Verwendung von verbesserten Materialien sowie der Einsatz optimierter Topographien stellen den Schlüssel für die Entwicklung effizienterer und ökonomischerer Solarzellen dar.

In der vorliegenden Arbeit wurden n- und p-Typ des hydrierten mikrokristallinen Siliziumoxids (μc-SiO$_x$:H) entwickelt und an unterschiedlichen Positionen innerhalb einer Solarzelle eingebaut. Diese Schichten wurden beispielsweise als transparente Fensterschicht, als Zwischenreflektor in Tandem-Solarzellen oder als Teil eines verbesserten Rückseitenreflektors implementiert. Herausragende optische Eigenschaften in Kombination mit gleichbleibend guten elektrischen Eigenschaften machen n- und p-Typ μc-SiO$_x$:H zu vielfältig anwendbaren Dotierschichten. Im Rahmen dieser Arbeit wurden dotierte μc-SiO$_x$:H Filme mit einer Leitfähigkeit von bis zu 10^{-2} S/cm und einer Raman-Kristallinität von ~60% hergestellt. Zusätzlich konnte eine breite Spanne in Bezug auf die optischen Eigenschaften realisiert werden. So konnte die optische Bandlücke E_{04} von 2.0 bis 2.7 eV und der Brechungsindex n von 1.8 bis 3.2 für den n-Typ und ein E_{04} von 2.1 bis 2.8 eV und der Brechungsindex n von 1.6 bis 2.6 für den p-Typ variiert werden. Die Schichteigenschaften lassen sich durch Anpassung der Depositionsparameter wie z.B. dem Verhältnis des CO_2/SiH_4 Anteils verändern. Eine

detaillierte Untersuchung des Einflusses der Dotiergaskonzentration von Monophosphan und Trimethylboran wurde ebenfalls durchgeführt. Schließlich wurden Parameterstudien bezüglich der Leistungsdichte, Druck und Temperatur durchgeführt. Im Rahmen dieser Arbeit wurde eine Effizienzsteigerung von a-Si:H Solarzellen von 9.4% auf 10.3% und die Effizienz von µc-Si:H Solarzellen von 8.4% auf 10.4% durch den Einsatz von p-Typ µc-SiO$_x$:H als Fensterschicht erzielt. Die Gründe für eine Effizienzerhöhung liegen einerseits in einer deutlich verbesserten Quanteneffizienz und andererseits in der Verbesserung von Spannung und Füllfaktor.

Der zweite Teil dieser Arbeit befasst sich mit dem optoelektronischen Zusammenspiel zwischen einem rauen Frontkontakt und der Solarzellleistung. Die Topographie bestimmt die Lichtstreuung und somit wird auch das Lichtmanagement der Solarzelle im Wesentlichen durch die Struktur des Frontkontaktes festgelegt. Ein breites Spektrum von verschiedenen Topographien wurde hier untersucht. Die durch die Rasterkraftmikroskopie gewonnenen Topographiedaten fungierten als Grundlage für dreidimensionale optische Simulationen. Diese Simulationen machen es möglich, ein tieferes Verständnis zwischen der Textur und dem Lichtmanagement zu entwickeln. Außerdem lassen sich so experimentelle Grenzen überwinden. Aus den Versuchen und Simulationen wurde schließlich klar ersichtlich, dass sowohl Strukturtyp als auch Strukturgröße den Stromdichtegewinn der Top-Solarzelle sowie den Stromdichteverlust der Bottom-Solarzelle bestimmen, wenn ein Zwischenreflektor eingebaut wurde. Die Effektivität des Zwischenreflektors ist außerdem stark abhängig von Reflexionsverlusten, die wiederum mit der Textur zusammenhängen. Insbesondere die Steilheit der Strukturen zeigt einen starken Einfluss.

Sehr raue Texturen können die elektrischen Eigenschaften von Solarzellen beeinträchtigen. Ein Aspekt der vorliegenden Arbeit gilt der Untersuchung dieses Einflusses und der Ausbildung rissreicher Regionen sowie den daraus resultierenden Verlusten. Es wurde herausgefunden, dass die Reduzierung der offenen Klemmspannung bei a-Si:H Solarzellen, welche auf sehr rauen Oberflächen abgeschieden wurden, der Ausbildung einer defektreichen Region in den ersten 100 - 200 nm der Absorberschicht resultiert.

Die Vorliegende Arbeit befasst sich mit Dünnschichtsilizium-Solarzellen mit dotiertem hydriertem mikrokristallinem Siliziumoxid sowie dem Einfluss der Frontkontakttopographie auf optische sowie elektrische Eigenschaften.

Abstract

Low cost and low material consumption are the most import advantages of thin-film silicon solar cells. The possibility to manufacture in large scale makes this technology an alternative photovoltaic technology that is suitable for mass production comparable to multi- and monocrystalline silicon solar cells. Also, compared to other thin-film solar cells that are based on CdTe or CIGS there is neither a limitation in supply of rare elements like tellurium and indium, nor toxic cadmium is used. However, conversion efficiency remains in a rather low level. The improvement of conversion efficiency due to application of optically advanced materials as hydrogenated microcrystalline silicon oxide and the efficient usage of solar cell textures are topics of this work. Moreover, optical and electrical loss mechanisms in thin-film silicon solar cells are discussed. The application of superior materials combined with optimized front textures can contribute to the development of more efficient and economically competitive future thin-film silicon solar cells.

In this work n- and p-type hydrogenated microcrystalline silicon oxide (μc-SiO$_x$:H) films were developed and implemented at different positions within a solar cell. This can be as a transparent contact or window layer in hydrogenated amorphous (a-Si:H) or microcrystalline silicon (μc-Si:H) single junction solar cells; as intermediate reflector layer in a-Si:H/μc-Si:H tandem solar cells or as part of a more effective back reflector in single and tandem solar cells. Higher transparency, solar grade electrical conductivity, low-ohmic contact to sputtered ZnO:Al and tunable refractive index make n- and p-type μc-SiO$_x$:H a versatile and advanced material compared to commonly used doped layers. In this work n- and p-type μc-SiO$_x$:H layers were fabricated with a conductivity of up to 10^{-2} S/cm and a Raman crystallinity of $\sim$60%. Furthermore, a broad range of optical properties (band gap E_{04} from 2.0 eV to 2.7 eV and refractive index n from 1.8 to 3.2) for n-type μc-SiO$_x$:H (E_{04} from 2.1 eV to 2.8 eV and n 1.6 to 2.6) for p-type μc-SiO$_x$:H films are presented. These properties can be tuned by adapting deposition parameters e.g. the CO$_2$/SiH$_4$ deposition gas ratio. Detailed work on the influence of the phosphine and trimethylborane concentration is also carried out. Finally, parameter studies regarding the power density, pressure and temperature are investigated for p-type μc-SiO$_x$:H films. In

the scope of this thesis the conversion efficiency of a-Si:H solar cells was improved by applying a p-type μc-SiO$_x$:H contact layer. Compared to the standard p-type μc-Si:H contact layer the conversion efficiency was increased from 9.4% to 10.3%. Absorption loss in the p-type layer was reduced, while the electrical contact was improved which resulted in a higher fill factor. Also, a conversion efficiency improvement of μc-Si:H solar cells was achieved by applying a p-type μc-SiO$_x$:H layer from 8.4% to 10.4%. Here, the external quantum efficiency was strongly improved. Also, a clear enhancement of the open circuit voltage was seen which is attributed to a reduced crystalline growth on top of the p-type μc-SiO$_x$:H layer.

In a second part of this work, thin-film silicon solar cells were deposited on differently textured transparent conductive oxide coated glass substrates. The focus here is on various aspects of light-management, as the light scattering is strongly influenced by the substrate textures. A broad range of surface topographies based on various state-of-the-art front side contacts were investigated. Additionally, using topography data obtained by AFM 3D rigorous optical simulations were conducted. Those simulations contribute to a deeper understanding of light scattering within tandem solar cells deposited on rough surfaces. From experiments and simulations it was found that there is a large impact of structure type and feature size on the enhancement of the top cell current density and of the current density loss in the bottom solar cell with an additional intermediate reflector layer. It is seen that the effectiveness of the intermediate reflector layer is highly linked to the solar cell reflectance. Especially the steepness of the texture shows large effects on the utilization of incident light.

Very rough morphologies can influence the electrical properties of a solar cell. One aspect of this work was to investigate the formation of defective-regions, growth behavior and recombination that are associated with the topography and material. From the electrical point of view it was seen that it is possible to obtain high quality contact layers between the TCO and p-type layer while improving the transparency. Furthermore, it was found that reduction of the open circuit voltages in a-Si:H thin film solar cells deposited on very rough front textures are mainly due to defective regions in the first 100 – 200 nm of the bulk material.

The present work deals with thin-film silicon solar cells containing doped hydrogenated microcrystalline silicon oxide with various functions and discusses the impact of the front side topography on optical and electrical properties.

Contents

Chapter 1

Introduction

The very first p-i-n solar cell with amorphous silicon (a-Si) as an absorber material deposited by glow discharge of silane (SiH_4) was presented in 1976 [1]. The solar cell showed an initial efficiency of 2.4%. As substrate indium tin oxide (ITO) coated glass was used. Since then, great efforts have been made on the thin-film silicon technology. The goal was to establish an alternative and resource saving technology to multi- and monocrystalline silicon solar cells. A variety of concepts including broadening of the absorption spectra by using germanium doped amorphous silicon [2] and microcrystalline silicon [3][4] has been very successful. With an improved absorptance in the long wavelength range those materials are suitable for the application as a bottom solar cell in thin-film silicon multi-junction solar cells. With an a-Si:H top and μc-Si:H bottom cell connected in series higher voltages as compared to single-junction solar cells are achieved while a broad light spectrum is utilized. Today the world record of initial conversion efficiency of tandem silicon solar cells amounts to 14.4% [5]. One key for implementation of this outstanding result is the application of n- and p-doped microcrystalline silicon oxide at different positions of the solar cells.

This dissertation will deal with different aspects of thin-film silicon solar cells. The results are presented in four chapters. They include material development and parameter studies on n- and p-type microcrystalline silicon oxides ($\mu c\text{-}SiO_x\text{:}H$); solar cells with implemented doped $\mu c\text{-}SiO_x\text{:}H$ for various applications; impact of interface topographies on the optical performance of solar cells; and electrical issues that occur when applying doped $\mu c\text{-}SiO_x\text{:}H$ or using differently rough front textures.

In Chapter 2 a short introduction on fundamental issues of thin-film silicon solar cells is given. While Chapter 3 deals with fabrication processes and sample preparation Chapter 4 is about various characterization and simulation methods. The experimental results of this thesis are structured in Chapter 5 - 8 and are introduced as following.

Chapter 5

In Chapter 5 results of the development of doped hydrogenated microcrystalline silicon oxide (μc-SiO$_x$:H) are presented. n- and p-type films are deposited by plasma enhanced chemical vapor deposition (PECVD) on glass substrates. Parameter studies concerning the variation of CO_2/SiH_4, SiH_4/H_2 and dopant gas/SiH_4 ratios are presented. Also, the impact of power density, pressure and temperature on the material properties are studied. In this chapter the interplay between optical properties i.e. optical band gap E_{04} and refractive index n and the electrical conductivity σ are discussed.

Chapter 6

n- and p-type microcrystalline silicon oxide μc-SiO$_x$:H are applied at different positions in single and multijunction solar cells. The impact of doped μc-SiO$_x$:H on the JV-characteristics, the external quantum efficiencies (EQE) as well as the reflectance are investigated. n- and p-type μc-SiO$_x$:H is applied in tandem solar cells as an intermediate reflector layer IRL between the hydrogenated amorphous silicon (a-Si:H) top and the hydrogenated microcrystalline silicon (μc-Si:H) bottom cell. With its lower refractive index compared to silicon, a portion of the incident light can be reflected back into the top cell and therefore, improve the top cell current density, while the a-Si:H i-layer thickness is kept thin. That way, electrical deteriorations associated by the light-induced degradation of a-Si:H material, known as the Staebler-Wronski Effect [6], can be minimized. This also renders possible current matching of both sub-cells in a higher level.

As another important application p-type μc-SiO$_x$:H can be used as window layers in a-Si:H and μc-Si:H solar cells. The state-of-the-art p-type layer stack, included a p-type μc-Si:H contact layer and an amorphous silicon carbide (a-SiC:H) p-layer. This contact layer provides a low-ohmic contact to the front contact, while rather large absorptions reduce the utilization of incident light. In order to improve the transparency, p-type μc-SiO$_x$:H layers are applied as a window layer for a-Si:H and μc-Si:H solar cells.

Finally, n-type μc-SiO$_x$:H was investigated to work as part of an advanced back reflector stack. Also at the back side a microcrystalline silicon oxide layer can improve

the utilization of light in a solar cell due to its superior optical properties. In this chapter, the application of n-type µc-SiO$_x$:H as back reflector in thin-film silicon single junction and tandem solar cells is discussed.

Chapter 7

In Chapter 7 the interplay between solar cell topography and short-circuit current density of tandem silicon solar cells, with and without an IRL fabricated on different front contact textures, is investigated. The focus here is on the impact of a large range of applied textures on the top and bottom cell short-circuit current densities and the associated optical losses. Also the influence of the IRL layer thickness for different front side topographies is discussed.

In order to gain deeper understanding on textured substrates and their impact on optical and electrical solar cell properties, a series of electromagnetic simulations was performed. The three-dimensional rigorous optical simulations uses AFM measurements of different interfaces taken from tandem solar cell devices deposited on various front contact textures. The optical simulations over a wide wavelength range allow a detailed study of computed modified textures. They make it possible to go beyond experimental limitations and investigate parasitic losses which occur in tandem solar cell devices.

Chapter 8

The last chapter deals with various electrical issues occurring in thin film silicon solar cell devices in p-i-n configuration. Particularly, the TCO/p and p/i-interface are investigated in detail. As a sensitive region the TCO/p contact problem occurring for solar cells deposited on aluminum doped zinc oxide is investigated. A deterioration of the fill factor is a mandatory problem when depositing a p-type a-SiC:H layer on top of ZnO:Al. By the application of different layer stacks including p-type µc-SiO$_x$:H the electrical performance of a-Si:H solar cells is studied.

Next, the p/i-interface is investigated. Here, the goal is to improve of the open circuit voltage V_{oc} by insertion of additional intrinsic silicon oxide buffer layers. In this chapter results concerning the impact of various intrinsic buffer layers inserted between the p-layer (p-type µc-SiO$_x$:H) and the a-Si:H i-layer are discussed.

As a final point, the effect of the front morphology on the open circuit voltage of a-Si:H single junction solar cells is investigated. Solar cells deposited on differently

textured front TCOs show differences in terms of the V_{oc}. Reasons for the deterioration of voltage seen for very rough front textures are discussed.

Finally, Chapter 9 gives a summary of all key results und conclusions of this thesis.

Chapter 2

Fundamental Considerations

2.1 Plasma Enhanced Chemical Vapor Deposition

Plasma-enhanced chemical vapor deposition (PECVD) is the most commonly used technology to fabricate thin-film silicon solar cells. It is a well-established technology to deposit thin films from the gas phase. In contrast to other technologies like the hot-wire CVD, where the thermal decomposition on silane (SiH_4) starts from 450°C, by help of a plasma low temperatures (< 200°C) are enough to create precursors out of silane. The plasma is formed by accelerated electrons induced by an external electrical field. Interactions between electrons and gas molecules result in formation of ions and radicals. Here, direct and alternating fields are possible, while commonly an alternating field with a RF-frequency of 13.56 MHz (Radio frequency) is applied in between two capacitor plates. An overview on the deposition technologies with focus on PECVD as well as on the thin-film silicon device technology is given in the monograph of R. Schropp and M. Zeman [8].

In the plasma, between the two electrodes electrons and ions experience differently strong accelerations due to different masses. Therefore, a characteristic potential profile is formed as shown in Figure 2.1.1. While the potential at the grounded electrode is always zero, the potential at the RF-electrode alters with the phase angle. Due to larger inertia of the positive ions compared to the electrons they remain more likely in the center of the plasma. Therefore, the potential in the plasma is always higher or equal to the potential of the electrodes. V_0 denotes the potential at the RF-electrode surface and ωt is the phase

angle of the alternating current. The plasma potential V_p is the potential that builds up in the center of the plasma region due to de distribution of cations and electrons.
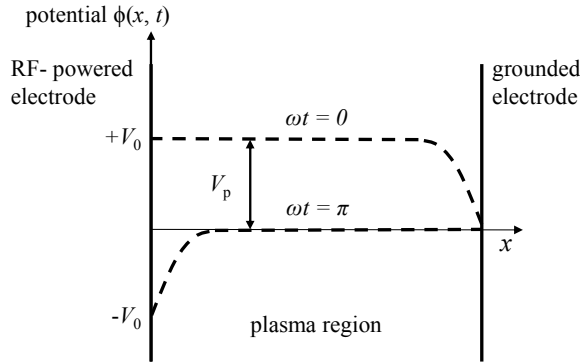
Figure 2.1.1: Spatial and time dependent potential distribution $\phi(x, t)$ between the RF- and grounded electrode inside a PECVD chamber for two different phase angles during an RF-cycle. With: V_0 = potential at the RF-electrode surface, ωt = phase angle and V_p = plasma potential [9].

The chemistry inside the plasma is complex. For fabrication of thin-film silicon solar cells the most common source gases are SiH_4 and H_2. Different reactions like ionization, radicalization, excitation and recombination take place simultaneously during the plasma process. The formation of the precursor SiH_3 required for a film-growth is given by the following formula:

$$2SiH_4 + 2e^- \rightarrow 2SiH_3 + 2H + 2e^- \rightarrow 2SiH_3 + H_2. \tag{2.1}$$
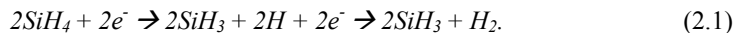
For film formation the following mechanism has been proposed. The SiH_3 precursor with one unsaturated bond diffuses to a hydrogen-terminated surface molecule and abstracts a hydrogen atom. A dangling bond is left over with which another SiH_3 can now form a Si-Si bond [10]. A sketch of the film-growth mechanism is shown in Figure 2.1.1.
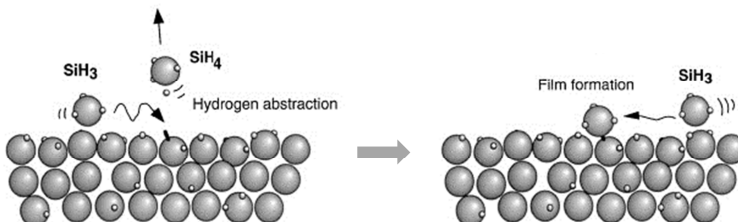
Figure 2.1.2: Silicon film growth mechanism with SiH_3 as precursor [10].

Important process parameters for PECVD are gas pressure p, gas composition, power density ψ, substrate temperature T_s and the frequency f of the alternating field.

2.2.   Silicon Thin-Film Solar Cells

2.2.1   Amorphous silicon

The first p-i-n thin-film solar cell with amorphous silicon a-Si as an absorber material was presented in 1976 by Carlson and Wronski [1]. The initial efficiency was 2.4% and from then, there has been an increasing interest on thin-film silicon technologies.

In contrast to crystalline silicon (c-Si) where a strict tetrahedron structure is formed by covalent bonds to four neighboring silicon atoms, amorphous silicon shows a lack of far order. It means that both bond length and bond angle vary in the lattice. The lattice disorder generates localized energy states within the band gap. Defect states at the edge of the energy gap are referred to as band tails. Moreover, the rather defective structure of a-Si contains a number of unsaturated bonds (dangling bonds) which create additional localized energy states within the band gap. Those defective states can act as recombination centers and are a reason for poor electrical properties of the a-Si material. One successful approach to improve the material is to hydrogenate and passivate the so called dangling bonds with hydrogen and therefore, to reduce the number defective states by several orders of magnitude. A schematic of the lattice of c-Si, a-Si and a-Si:H is presented in Figure 2.2.1.
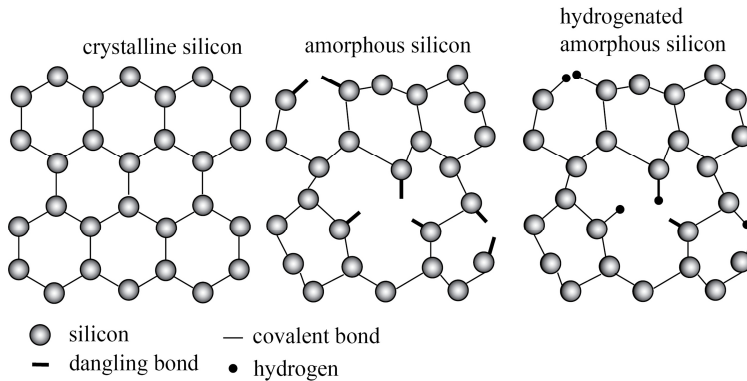
Figure 2.2.1: Schematic of silicon lattices: crystalline silicon, amorphous silicon and hydrogenated amorphous silicon.

Unlike in crystalline semiconductors where conduction band and valence band are well defined, in amorphous semiconductors they appear "blurry" and vary spatially. Defective states in disordered semiconductors cause a scattering of the periodicity of the wave function of electrons. The distortion of the wave vector results in an absorption spectrum that is similar to direct semiconductors. The energy dependent density of states in a-Si is shown in Figure 2.2.2. Instead of defined band edges due to the disrupted coherence of Bloch waves, localized extended states as tail states and states associated with dangling bonds (D-center) are indicated in the schematic. D-centers can be found in three different charge states: +, 0, – and vary for intrinsic layers with different defect densities and doped layers. These localized states have far lower carrier mobility as compared to delocalized states in the conduction and valence band. Due to the sharp separation in terms of the mobility of charge carriers for a-Si the term "band edge" is substituted by "mobility edge". Correspondingly, the term "band gap" is replaced by "mobility gap" [11][12][13].

The doping efficiency for a-Si materials is very low which is because doping itself works rather differently as compared to crystalline silicon. While in c-Si the fourfold coordinated sites of Si leaves one electron free from the five valence electrons of phosphorus (P) inducing a shift of the Fermi level, P is mainly threefold coordinated in a-Si. That allows the remaining two electrons to pair in an s-orbital. These two electrons are therefore not free as in the fourfold case and do not induce a shift of the Fermi level. Additionally, the small proportion of P-atoms that is fourfold coordinated in a-Si is companioned by a D^- dangling bond that can consume the free electron. Also, dangling bonds function as traps for holes leading to a reduced bipolar transport for electrons and

holes in doped a-Si [14]. Thus, charge carriers generated in doped a-Si layers do not contribute to the current of a solar cell.
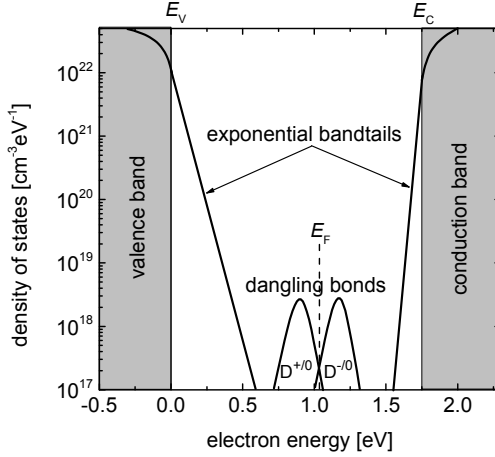
Figure 2.2.2: Schematic of density of electronic states in a-Si:H as a function of the electron energy. Delocalized states in the bands are indicated by the grey shaded area; localized states as bandtails with exponential distribution and states originating from dangling bonds ($D^{+/0}$ and $D^{-/0}$) are shown in the mid-gap area [12].

The optical absorption coefficient α as a function of the photon energy E of a-Si:H and c-Si is shown in Figure 2.2.3. a-Si:H, as a quasi-direct semiconductor, show a higher absorption coefficient for higher energies as c-Si as an indirect semiconductor. Since the tail state distribution near the band edges is exponential, it gives rise to an exponential part in the absorption spectrum of a-Si:H in a range from 1.4 eV – 1.7 eV which is called "Urbach-edge". Below the photon energy of 1.4 eV absorption is assigned to defects originating from dangling bonds. A conventional procedure to describe the optical band gap is the use of E_{04}. It is defined as the photon energy at which the absorption coefficient equals 10^4 cm^{-1} and amounts to ~1.75 eV for a-Si:H [12][14].
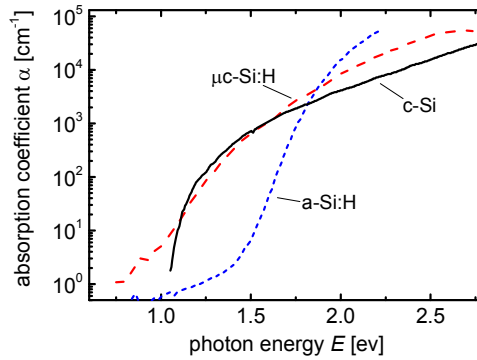
Figure 2.2.3: Absorption coefficient α of a-Si:H, µc-Si:H and c-Si as a function of photon energy E.

2.2.2   Microcrystalline silicon

When changing deposition parameters to lower SiH_4/H_2 ratios a transition from amorphous to microcrystalline silicon (µc-Si:H) takes place. µc-Si:H material can be seen as a two phase material with nano-sized crystalline silicon grains embedded within an a-Si:H matrix. Dependent on deposition parameters the crystallites can differ in size from several nanometers to several micrometers. Also, formation of voids as well as grain boundaries are found in µc-Si:H films. A schematic model of the structure for various crystalline volume fractions of µc-Si:H material is shown in Figure 2.2.4. Like crystalline silicon, microcrystalline silicon acts like an indirect semiconductor. The absorption spectrum is similar to c-Si as shown in Figure 2.2.3. Compared to a-Si:H α is lower for photon energies above 1.8 eV. Due to a smaller band gap the absorption coefficient raises for photon energies >1.1 eV. That makes µc-Si:H a suitable material for a bottom solar cell. More details on the structural properties are reported in [15][16][17].
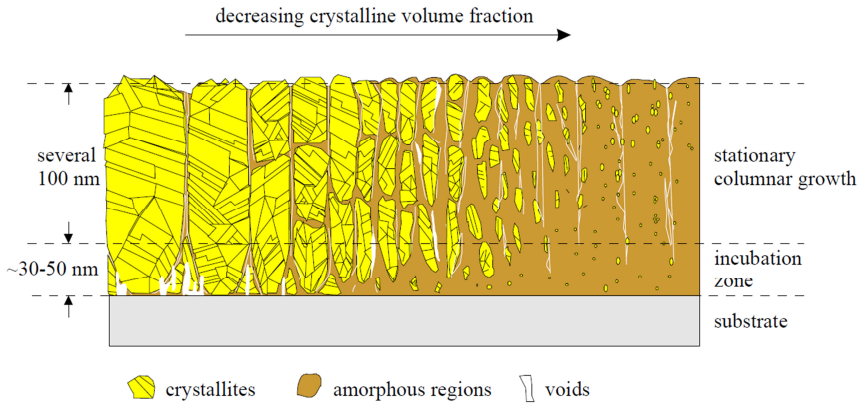
Figure 2.2.4: Schematic model of the volumetric microstructure of µc-Si:H as a function of decreasing crystallinity [15][17].

2.2.3 Staebler-Wronski effect

One of the most important disadvantages that the a-Si:H thin-film solar cell technology has to face is the photo-electronic effect called "Staebler-Wronski effect". It denotes the metastable behavior of amorphous silicon and is linked to a deterioration of electrical properties after exposure to light. Thus, illuminating a-Si:H based solar cells is associated with a light-induced formation of additional defects that are ascribed as dangling bonds. The photo as well as the dark conductivity of a-Si:H is reduced by several orders of magnitude [6]. Commonly after 1000 h of "light-soaking" the solar cells are regarded as stabilized, which means that further illumination does not lead to a worsening of the electric properties any further. Till now, there is no general agreement on the mechanism of the Staebler–Wronski effect. It has been proposed that the recombination of generated electrons and holes may set free enough energy to break a weak Si–Si bond nearby [18] and leave a dangling bond behind. Another proposed model suggests that emission of hydrogen atoms from Si–H bonds lead to formation of dangling bonds [19]. Interestingly the Staebler-Wronski effect is reversible which means that the electric properties can be almost completely restored by annealing for several minutes above 150°C. The light induced degradation can be reduced for thinner a-Si:H absorber layers. Also, for multijunction solar cells the relative worsening of the conversion efficiency is lower as compared to a-Si:H single junction solar cells [20].

2.3. Current-voltage-characteristics

For a pn-diode the dark current-voltage-characteristics (*IV*-characteristics) can be described by Formula (2.2) where I_0 is the dark saturation current, T the temperature, n the ideality factor, q the elementary charge and k the Boltzmann constant.

$$I_{dark}(V) = I_0 \cdot \left[e^{\left(\frac{qV}{nkT}\right)} - 1 \right] \tag{2.2}$$

A p-i-n diode can also be described by that formula. However, a p-i-n solar cell device is more complex. Figure 2.4.1 shows a simplified equivalent circuit to define the electric characteristics of a p-i-n solar cell. This model consists of a photo current I_{ph} (power source) a diode, a shunt or parallel resistance R_{sh} and a series resistance R_s. The resistances represent parasitic losses within a solar cell. R_s are ohmic losses originating primarily from contact resistances. R_{sh} is driven by the silicon bulk material and is also affected by shunts thought the solar cell.
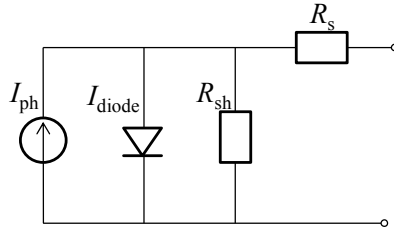
Figure 2.3.1: Equivalent circuit of a solar cell device including a photo current I_{ph}, diode current I_{diode}, series resistance R_s and shunt-resistance R_{sh}.

The dark *IV*-characteristics consist therefore of an overlap between diode term and the current-flow though R_{sh} and R_s.

$$I_{dark}(V) = I_0 \cdot \left[e^{\left(\frac{q \cdot (V - I_{dark}(V) \cdot R_S)}{nkT}\right)} - 1 \right] + \frac{V - I_{dark}(V) \cdot R_S}{R_{sh}} \tag{2.3}$$

The current density J denotes the current per area. For solar cells it stands for the generated current per solar cell area. In the following the term current density will be used.

A typical dark *JV*-curve of an a-Si:H p-i-n solar cell is shown in Figure 2.3.2. The dark *JV*-curve can be divided in three voltage dependent characteristic sections which are marked in the figure.
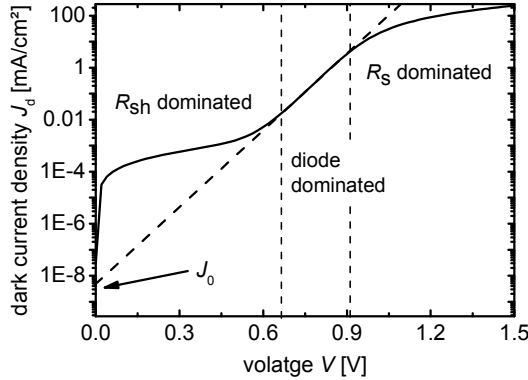
Figure 2.3.2: Dark *JV*-curve for an a-Si:H solar cell. By extrapolation the reverse bias saturation current density J_0 is obtained. The diode ideality factor *n* is inversely proportional to the slope of the extrapolated line.

The current-flow in the first section (low voltage) is determined by the shunt resistance. In the intermediate section it is dominated by the diode because the current-flow in the diode is much larger than in the parallel resistance. The third section (high voltage) is limited by the series resistance, because the current-flow through the diode is so high that the dark *JV*-characteristics are determined by series resistance. Also, from the dark *JV*-curve the diode quality factor *n* and the reverse bias saturation current density J_0 are obtained. *n* is inversely proportional to the slope of the extrapolation. The intersection between extrapolation and the *y*-axis corresponds to J_0.

The *JV*-characteristics under illumination can be described as a superposition of the dark current density J_{dark} and the photo current density $J_{ph.}$

$$J(V) = J_{dark}(V) - J_{ph}(V) \tag{2.4}$$

Figure 2.3.3 shows a *JV*-curve of a single junction solar cell under illumination. The short-circuit current density J_{sc} is defined as the current density at which the voltage is zero. Since J_{dark} is zero under this condition J_{sc} corresponds to J_{ph} and is the maximal current that can be exacted from a solar cell.

$$J_{sc} = J(V = 0) = J_{ph}(V = 0) \qquad (2.5)$$

The open circuit voltage V_{oc} describes the voltage for which the current flow is zero and J_{dark} is equal to J_{ph}. It denotes the maximum possible voltage. For $R_s = 0$ and very large R_{sh} the V_{oc} can be approximated by:

$$V_{oc} = \frac{nkT}{q} \cdot ln\left[\frac{J_{ph}}{J_0} + 1\right] \qquad (2.6)$$

The maximum power point MPP is the working point in which the maximal power output is gained. The fill factor FF is a measure for the efficiency of collection of charge carriers in a solar cell. It is defined by the ratio between the maximum power (P_{MPP}) and the product of J_{sc} and V_{oc}.

$$FF = \frac{J_{MPP} \cdot V_{MPP}}{J_{sc} \cdot V_{oc}} \qquad (2.7)$$

The conversion efficiency η is the ratio between input and output. For solar cells it is defined by the ratio between the maximum power P_{MPP} and the power of the incident light P_i.
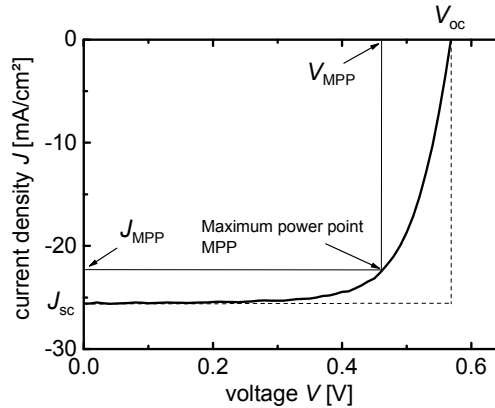
Figure 2.3.3: JV-characteristic of a single junction µc-Si:H solar cell under illumination indicating J_{sc}, V_{oc} and MPP.

For further reading, the standard textbook "Physics of Semiconductor Devices" by S. M. Sze is recommended [21].

2.4   the p-i-n Structure

In a p-i-n solar cell the intrinsic layer, also called absorber layer, is sandwiched between a p-type and an n-type layer. The doped p- and n-type layers are responsible for the separation of charge carriers generated within the i-layer. Charge carriers generated within the doped layers do not contribute to the current of a solar cell due to the high defect densities in these layers. For the design of a p-i-n device it means that intrinsic layers (absorber layers) should be rather thick to generate a large number of charge carriers, while doped layers have to be kept very thin to minimize the loss of photons. In contrast to a p/n-structure where the charge carrier transport is driven by diffusion, in a p-i-n device the driving force is supported by an electrical field (drift) induced by the p- and n-type layers. This is necessary because due to the high density of localized states in a-Si the lifetime τ of minority carriers is very short. Especially the transport of holes is limited because of the low mobility μ.

Solar cells fabricated in this work are all made in p-i-n (superstrate) configuration. The silicon layers are deposited on top of a supporting glass sheet that is covered with a transparent conductive oxide (TCO). The solar cell device is shown in Figure 2.4.1.

n-i-p (substrate) configurations are also possible. It means that the deposition starts with the n-type layer and ends with the p-type layer. Still, the side that faces the incident light is always the p-type side. This is advantageous because the mobility of holes and therefore the $\tau\mu$-product is far lower that for electrons [22]. Because holes are collected in the p-type layer and of the charge carrier generation profile (Lambert–Beer law) the mean distance that have to be traveled by holes is shorter. That way, the probability of recombination is reduced [23][24][25].

A schematic band structure is shown in Figure 2.4.1 b). Charge carriers are separated inside the intrinsic layer. Driven by the electrical field induced by the doped layers holes move upward and are collected in the p-type layer, while electrons move downward to the n-type layer. Through an external circuit the electrons are conducted to the front contact and recombine at the p-type layer.
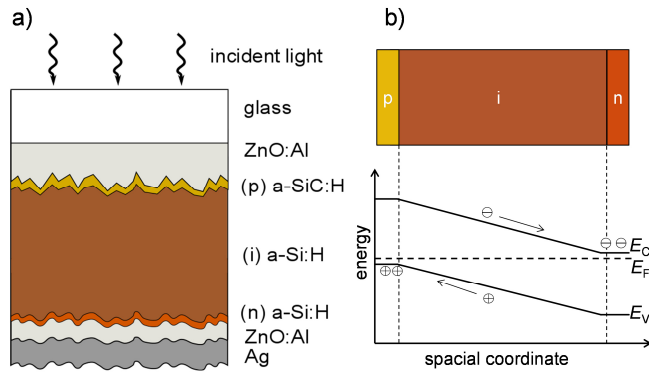
Figure 2.4.1: a) Sketch of an a-Si:H single junction solar cell in p-i-n superstrate configuration, and b) a corresponding schematic band structure of an p-i-n solar cell.

Correspondently, multijunction devices made of two or more junctions are fabricated by connecting p-i-n devices in series. A double-junction or tandem device consisting of an a-Si:H top and a μc-Si:H bottom solar cell is shown in Figure 2.4.2 a). Here, a higher utilization of incident light is possible leading to higher conversion efficiencies. The top cell absorbs the short wavelength light, while long wavelength light is absorbed in the bottom cell. A schematic of the band structure of a double junction device is shown in Figure 2.4.2 b).
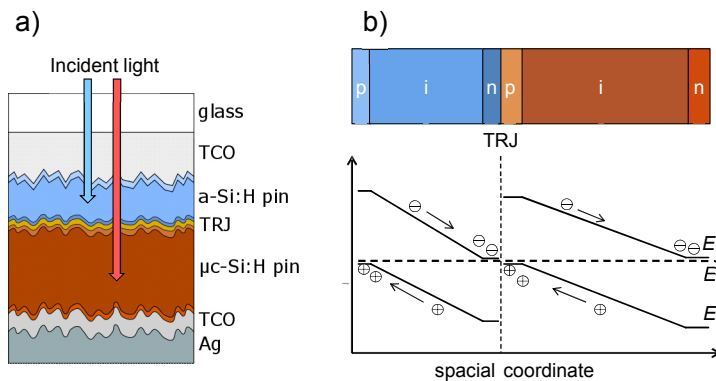
Figure 2.4.2: a) Sketch of double-junction (tandem) solar cell consisting of an a-Si:H top and μc-Si:H bottom cell in p-i-n/p-i-n superstrate configuration. b) By facing the same direction the series connection is illustrated with a schematic band structure of the tandem device including a tunnel-recombination junction TRJ.

The interconnection of the two junctions is called tunnel-recombination-junction. Electrons generated in the top cell and holes from the bottom cell recombine here and do not contribute to the charge carrier collection. However, the series connection results in an addition of the open circuit voltage V_{oc} originating from the sub-cells. This is illustrated in Figure 2.4.3 where characteristic *JV*-curves of a tandem device are shown. Here, the short-circuit current density J_{sc} of the tandem cell is limited by the top-cell J_{sc}, but the $V_{oc, tandem}$ is the sum of the $V_{oc, top}$ and $V_{oc, bottom}$. In a real device $V_{oc, tandem}$ is smaller than the sum which associated to several loss mechanisms that will not be discussed here.
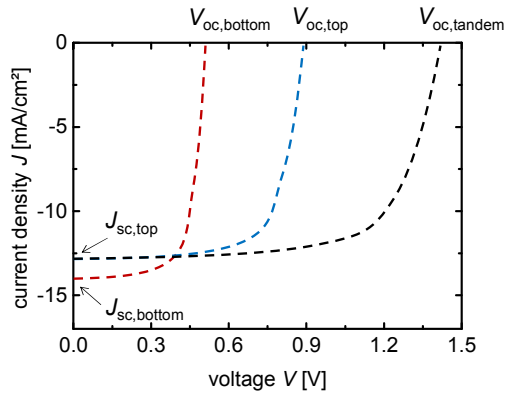
Figure 2.4.3: Schematic *JV*-curves of an a-Si:H/µc-Si:H tandem solar cell with a top (blue dashed lines) and bottom cell (red dashed lines) connected in series.

Due to a smaller band gap and a larger absorption coefficient in the long wavelength rage µc-Si:H is highly suitable for the application as a bottom cell for a high utilization of sunlight as shown in Figure 2.4.4.
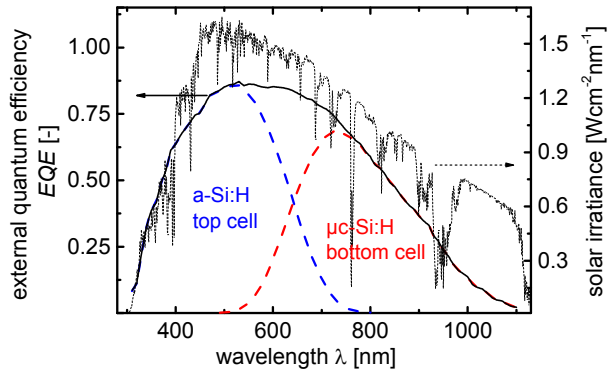
Figure 2.4.4: External quantum efficiency of an a-Si:H/μc-Si:H tandem solar cell. The dotted lines represent the spectral irradiance of the AM 1.5G spectrum (ASTM G173-03 Reference Spectrum).

The external quantum efficiency *EQE* is a measure for the probability of one incident photon of certain energy to generate a charge separation. The blue dashed line shows the *EQE* of the a-Si:H top cell and the red dashed line stands for the bottom cell. The black line is the sum of both *EQE*s. When displaying the *EQE* of a tandem device in a superimposed figure together with the AM 1.5G spectrum (solar spectral irradiance with air mass 1.5, published by American Society for Testing and Materials *ASTM*) it becomes apparent that both spectra are rather similar over a larger wavelength range.

2.5.   Transparent Conductive Oxides

Transparent conductive oxides (TCO) are mainly used in thin-film solar cells as front side contacts. High optical transparency, electrical conductivity and a suitable surface structure are the most relevant specifications for TCOs. They have a large band gap (≥ 3 eV) and are often doped to degeneracy. Indium tin oxide (ITO) [26], fluorine doped tin oxide (SnO_2:F) fabricated by atmospheric pressure chemical vapor deposition (APCVD) [27][28], sputter-etched aluminum doped zinc oxide (ZnO:Al) [29] or boron doped zinc oxide (ZnO:B) fabricated by low pressure chemical vapor deposition (LPCVD) [30] are the most common TCOs applied as a textured front contact in thin-film solar cells.

A challenge for TCO material for solar cell or module application is that the entire current that is generated inside the solar cell has to be transported through the front TCO layer. In order to minimize the resistive losses, the front contact has to be sufficiently thick or sufficiently high conductive which can be realized by doping. However, these specifications are in contrast with the optical transparency of the layer. Solar grade TCOs show a mean transmittance of >80% in a range between 400 – 800 nm.

For optimization of the conversion efficiency the improvement of absorptance of thin-film solar cells is indispensable. The idea of "light-trapping" is to enlarge the path of propagating light inside the absorbing layer by total internal reflection without increasing the layer thickness. The enhanced light scattering is primarily driven by texturing of the front TCO. The optical effects are further enhanced when placing a reflector at the back side of the solar cell. Therefore, the topography of the front and back side is of relevance. The theoretical maximum gain associated with internal reflection by textured topography has been proposed by Yablonovitch [31]. It is stated that the maximum gain of light intensity amounts to $4n^2$ with n as the local refractive index. Optical enhancement for a-Si:H solar cells by texturing were first achieved by Deckmann et al. [32]. From then, the improvement of light-trapping by finding suitable front side TCO topographies has been pursued steadily [33][34].

Chapter 3

Material and Solar Cell Preparation

3.1. The Large Area Deposition System

As the most commonly used method for deposition of amorphous and microcrystalline silicon thin-film solar cells, plasma-enhanced chemical vapor deposition (PECVD) was applied for the preparation of all solar cells and single layers investigated in this work.

A modified large area PECVD system (originally from the *Material Research Group MRG* in Colorado) suitable for one 30×30 cm² or four 10×10 cm² substrates was used. For gas purity reasons the high vacuum of the LA-PECVD system is maintained at a basic pressure of $< 6.6 \times 10^{-7}$ mbar. The power is applied by a radio frequency RF-generator with a frequency of 13.56 MHz for all electrodes. The PECVD system consists of two load lock chambers and two separate process cambers (PC) including three electrodes. A sketch of the equipment is shown in Figure 3.2.1. In PC 1 and 2 only intrinsic layers are deposited, while in PC 3 all doped layers including a-SiC:H and µc-SiO$_x$:H layers are fabricated. The electrode gap for PC 1 and 3 is 12.5 mm and in PC 2 it is 9 mm.
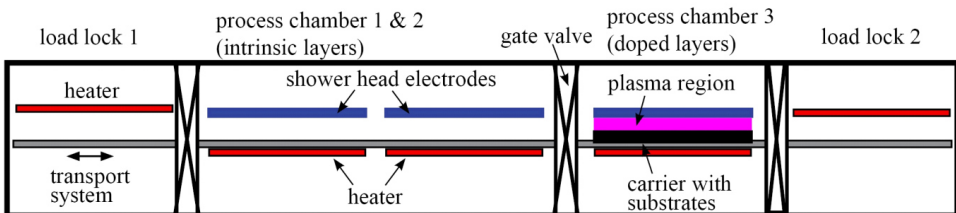
Figure 3.2.1: Schematic of the large area PECVD deposition system (top view).

Sealing gate valves between load lock chambers and process chambers improve the basic pressure and also render possible separate depositions at the same time. Substrates are mounted vertically on a carrier and are moved via an inline splint transport system. The carrier also represents the substrate electrode and is grounded during the deposition. Heating plates behind the substrate electrodes are responsible for adjustment for the temperature. Process gasses are applied through a showerhead electrode, which also represents the RF-electrode. The RF-electrodes are connected via matchboxes containing inductive coils and variable capacitors with the external power generators. The gas flows are controlled via mass flow controllers and are measured in standard cubic centimeters (sccm). The deposition pressure is set by a butterfly valve. A sketch of the PECVD chamber with external power generator and matchbox is shown in Figure 3.2.2. For detailed information on the deposition system see reference [35][36].
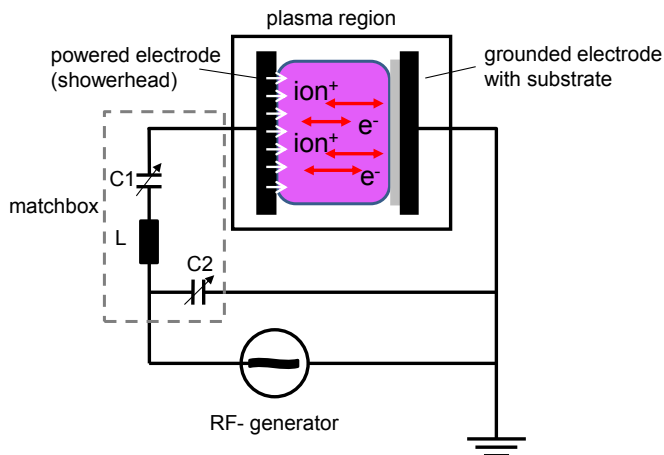
Figure 3.2.2: Schematic of a PECVD reactor with matchbox for impedance control.

Process gases

In this work, all a-Si:H, µc-Si:H and µc-SiO$_x$:H alloys were prepared by deposition from the gas phase. The process gases for intrinsic absorber layers were silane (SiH$_4$) and hydrogen (H$_2$). For p-type layers trimethylborane (B(CH$_3$)$_3$ or TMB) and for the n-type material phosphine (PH$_3$) was used as dopant sources. CO$_2$ was added as an oxygen source for the deposition of microcrystalline silicon oxide µc-SiO$_x$:H layers. For p-type

amorphous silicon carbide layers (p-type a-SiC:H) applied in a-Si:H solar cells methane (CH$_4$) was used as a carbon source. The gases were applied to the process through a powered showerhead electrode.

3.2.   Sputter-Etched ZnO:Al

Aluminum doped zinc oxide (ZnO:Al) coated glass (*Corning Eagle XG*[®]) fabricated by magnetron sputter deposition are used as a standard front contact in this work. For texturing reasons the ZnO:Al coated substrates were wet-chemically etched by a diluted HCl (0.5 wt%) solution. Additionally to single textured ZnO:Al some investigations were obtained with double-textured ZnO:Al (DT-ZnO:Al) involving a second etching step with a 1 wt% HF solution. In this work, two different targets were used for the sputtered ZnO:Al containing 1 wt% and 0.5 wt% aluminum, respectively. Detailed investigations on sputter-etched ZnO:Al are reported elsewhere [29][34][37]. More specifications for differently modified ZnO:Al front contacts applied in this work are given in the corresponding chapters.

3.3.   Solar Cell Device - Structure and Preparation

a-Si:H solar cells

Hydrogenated amorphous silicon solar cells (a-Si:H) applied in this work consist of a p-type amorphous silicon carbide layer (p-type a-SiC:H), an amorphous intrinsic absorber layer (a-Si:H i-layer) and an amorphous n-type layer (n-type a-Si:H). When deposited on sputter-etched aluminum doped zinc oxide front contacts an additional microcrystalline p-type contact layer was deposited between the ZnO:Al and the p-type a-SiC:H layer. The applied power density for the intrinsic a-Si:H layer was 0.28 W/cm² and the pressure was 4 mbar. The heater temperature was held constant at 200°C. The standard thickness of an a-Si:H solar cell is 350 nm.

µc-Si:H solar cells

The standard p-i-n device consists on a p-type μc-Si:H layer, an μc-Si:H absorber layer and an a-Si:H n-type layer. A silane grading was applied within the first minutes of the i-layer deposition starting at a SiH_4/H_2-ratio r_{SiH4} = 1.26%. The end value for the grading of the standard process is r_{SiH4} = 1.52% and has been kept constant for rest of the complete i-layer deposition. The applied power density for the intrinsic μc-Si:H layer was 4.4 W/cm². The pressure for the μc-Si:H absorber layer deposition was 10.7 mbar and the temperature 160°C. The standard thickness of a μc-Si:H solar cell is 1.2 μm.

a-Si:H/μc-Si:H Tandem solar cells

Tandem solar cells consist of an a-Si:H top and a μc-Si:H bottom cell in a series connection. The n-type layer of the top cell is electrically connected with the p-type layer of the bottom cell via the so call tunnel-recombination junction TRJ. Electrons from the top cell and holes from the bottom cell recombine the TRJ. In order to accelerate the recombination at the TRJ and therefore, improve the electric properties of a tandem device an additional n-type microcrystalline silicon layer (n-type μc-Si:H) is deposited between the n-type a-Si:H and the p-type μc-Si:H layer.

Back contact and laser process
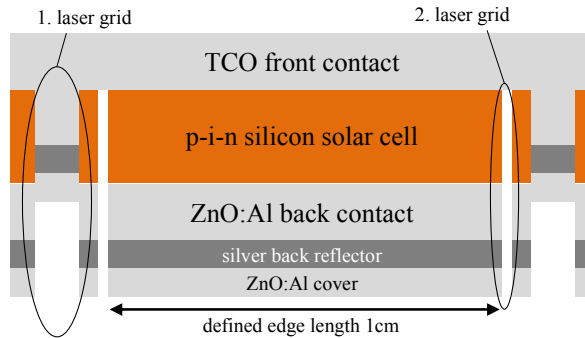
Figure 3.3.1: Sketch of the side view of a solar cell device after deposition of the back contact including laser grids.

After the deposition of all silicon layers the devices are cooled and unloaded for further treatments. Figure 3.3.1 shows the schematic side view of the completed solar cell device. The first step is a laser process at which grid lines are cut out of the silicon layer enabling a connection to the front TCO contact (1. laser grid). Subsequently, a ZnO:Al/Ag/ZnO:Al back contact or back reflector stack is deposited by sputtering and thermal evaporation process. A post annealing treatment in atmospheric ambient for 30 min at a temperature of 160°C was done to improve the connectivity between silicon and the back contact. In a final laser step the active solar cell area of 1×1 cm² was defined (2. laser grid). That way, the back contact is isolated from the front. More details on the laser process are given in reference [38].

3.4.   Preparation of Single Layers

Single layers are prepared for investigations of material properties of doped hydrogenated microcrystalline silicon oxide (μc-SiO$_x$:H) films by PECVD. *Corning eagle* glass was used as supporting substrates on which ~500 nm thick single layers are deposited. This layer thickness is especially needed for the determination of the refractive index. The characterization methods are described in Chapter 4 and results on the development on n- and p-type μc-SiO$_x$:H films are presented in Chapter 5.

Chapter 4

Characterization and Simulation Methods

4.1.   Material Characterization Methods

4.1.1. Layer thickness

For calculation of the deposition rate r_d and also for determination of the electric conductivity σ, band gap E_{04} and refractive index n the information on the layer thickness is mandatory. For that purpose narrow lines of the deposited films are removed from the glass substrates using a laser. The sharp edge was then measured mechanically using a *Vecco Dektak 6M Stylus Profiler*. For measurement of the thickness of a solar cell the same method was used. For doped layers applied in a solar cell as well as for the sub-cells in tandem solar cells the layer thicknesses are calculated using the deposition rate determined for single layers and single junction solar cells respectively.

4.1.2. Spectral Photometry

The transmittance T and reflectance R of front TCO contacts, doped $\mu c\text{-SiO}_x\text{:H}$ films and the solar cell reflectance were measured using a *UV-VIS-NIR Perkin-Elmer LAMDA 950 photo spectrometer* with integrating Ulbricht sphere. The spectrometer contains a deuterium and a tungsten halogen lamp as light sources and covers a wavelength range from 250 to 2500 nm.

The absorptance A of a solar cell is calculated from the reflectance R measurement:

$$A(\lambda) = 1 - R(\lambda) \qquad\qquad (4.1)$$

The refractive index n was calculated from the transmission and reflection spectra using the Fresnel equation at a wavelength of 1000 nm. T and R spectra are taken from single layers with a thickness of several hundred nanometers deposited on glass substrates. From the minima and maxima of the interference fringes a Sellmeier-plot is drawn up. The oscillation energy E_{osc} and the dispersion energy E_d are obtained from the Sellmeier-plot. The refractive index for a certain photon energy E is calculated by a one-oscillator model:

$$n^2(E) - 1 = \frac{E_d \cdot E_{osc}}{E_{osc}^2 - E^2} \qquad\qquad (4.2)$$

For details see reference [39][40].

4.1.3. Photothermal Deflection Spectroscopy

Photothermal deflection spectroscopy (PDS) was used as a highly sensitive tool for the investigation of optical absorption. By PDS also absorptions in band tails and in sub-band gap energy range can be measured. The set-up consists of a cavity filled with carbon tetrachloride (CCl_4) which surrounds the sample. A monochromatic chopped light beam illuminates the sample in a wavelength range of 310 nm $< \lambda <$ 2600 nm. The light source consists of a halogen lamp and a xenon lamp. The heat generation in the sample due to absorption and the heat transfer to the surrounding fluid causes a change of the refractive index of CCl_4 which is detected by a passing laser beam. The band gap E_{04} is defined as the photon energy at which the absorption coefficient α amounts to 10^4 cm^{-1}. This method is especially suitable for measuring samples with a low absorption coefficient. More details are given in reference [41][42].

4.1.4. Electrical Conductivity Measurements

The specific electrical conductivity σ of doped microcrystalline silicon oxide (μc-SiO$_x$:H) films were investigated by dark conductivity measurements with coplanar Ag electrodes. The measurement were performed in lateral direction which describes the electrical conductivity sufficiently, even though the longitudinal conductivity might be higher due to the growth-paths of a microcrystalline phase through the amorphous silicon oxide matrix. For measurement in planar direction two silver electrodes with a gap of 0.5 mm were evaporated on top of the μc-SiO$_x$:H films. For a known layer thickness and with the given width and distance between the evaporated electrodes the specific electrical conductivity is calculated. σ was obtained in vacuum after an annealing step at 440 K for 30 min at a voltage of 100 V.

4.1.5. Rutherford Backscattering Spectrometry

Rutherford backscattering spectrometry (RBS*)* is used to determine the elemental material compositions. Particularly for μc-SiO$_x$:H films the oxygen content in the material was quantified and presented as the oxygen to silicon ratio $r_{O, RBS}$.

$$r_{O,RBS} = \frac{O[atm.]}{Si[atm.]} \qquad\qquad (4.3)$$

The principle of RBS can be described by an elastic collision between particles in the incident ion beam (H$^+$) and atom nuclei in the samples. Through interaction between sample and the ion beam a fraction of the beam is scattered back. The number of back scattered ions is about proportional to the square of the number of target atoms. Rutherford backscattering spectrometry is a precise method to measure the oxide content of a sample independent of the nano-structure. The error is approximately ±5% for the stoichiometric fraction. Detailed experimental descriptions can be found in reference [43].

4.1.6. Raman Spectroscopy

Raman spectroscopy is a fast method to obtain the crystallinity of the silicon fraction in μc-Si:H and also μc-SiO$_x$:H films. For the determination of the crystalline volume fraction I_c of single layers a laser with a wavelength of 488 nm was used. The principle of

this method is based on inelastic scattering of photons when interfering with a sample. Here, a photon can whether emit (Stokes scattering) or absorb a phonon (anti-Stokes scattering). Characteristic spectra for µc-Si:H, amorphous and microcrystalline silicon oxide are presented in Figure 4.1.1.
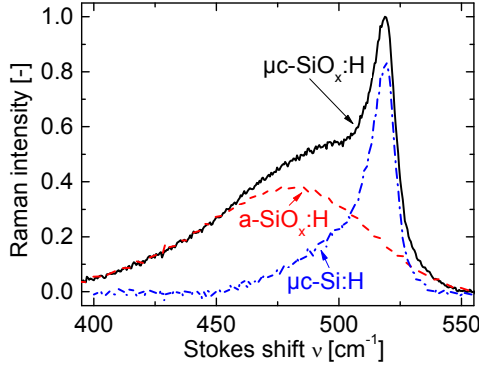
Figure 4.1.1: Normalized Raman intensity plotted as a function of the Stokes shift for µc-SiO$_x$:H film (black solid line). The a-SiO$_x$:H portion is shown as red dashed line and the µc-Si:H fraction is shown as a blue dashed-dotted line. To calculate the crystalline volume fraction I_c the integrated areas are used. [44]

In order to examine the crystalline volume fraction of the material, a Raman intensity ration I_c was determined as the ratio of the integrated area A of the µc-Si:H peak at 520 cm^{-1} to the total peak area:

$$I_c = \frac{A_{\mu c-Si:H}}{A_{\mu c-SiOx:H}} , \qquad (4.4)$$

with

$$A_{\mu c-SiOx:H} = A_{\mu c-Si:H} + A_{a-SiOx:H} \qquad (4.5)$$

For more details see reference [44] - [47].

4.1.7. Transmission Electron Microscopy

High resolution transmission electron microscopy HR-TEM was used for structural visualization of thin films in an atomic scale. The images were taken with a *FEI Titan 80-*

300 field emission transmission electron microscope with an imaging spherical aberration corrector at the *Ernst-Ruska Centre*. Images are taken with a *Gatan UltraScan 1000P (2k x 2k)* charge coupled digital camera. With a sub angstrom resolution it is possible to see atomic pattern and distinguish between crystalline and amorphous regions. For transmission electron microscopy samples have to be made very thin. Commonly, lamellas are prepared by focused ion beam treatment. In this work, thin µc-SiO$_x$:H film with a thickness of 30 nm were deposited on a ZnO:Al covered glass sheet. The ZnO:Al was subsequently etched away using a 20 wt% concentrated HCl solution. After cleaning with deionized water the samples are dropped and dried on top a TEM sample grid.

4.1.8. Atomic Force Microscopy

Atomic force microscopy *AFM* was used for mapping of nano-rough surface textures. The working principle oscillation is described as following. A 10 nm - 15 nm high silicon tip scans the surface of a sample. The tip is connected to a cantilever which is induced to oscillate in a frequency of several hundred kHz. As the tip moves over a sample the position of the cantilever varies through interaction of the tip with the surface. The cantilever is irradiated with a monochromatic laser beam and from the reflected light beam detected by a photodiode the position of the cantilever is obtained. In this work AFM measurements were conducted with a *Nanostation 300 SIS* system with a resolution of 1024 × 1024 pixels in non-contact mode for an area of 20 × 20 µm².

Root Mean Square Roughness

The root-mean-square roughness σ_{RMS} was calculated by using the *Statistical Quantities Tool* from the open source program *Gwyddion*. σ_{RMS} characterizes the roughness of a surface in vertical direction calculated from the mean square distance of each point to the average surface height z_M. With:

$$z_M = \frac{1}{N_x \cdot N_y} \sum_i^{N_x} \sum_j^{N_y} z_{i,j} \tag{4.6}$$

$$\sigma_{\text{RMS}} = \sqrt{\frac{1}{N_x \cdot N_y} \sum_i^{N_x} \sum_j^{N_y} (z_{i,j} - z_M)^2} \tag{4.7}$$

Autocorrelation Length

The autocorrelation length *ACL* was obtained by fitting of the exponential Height-Height Correlation Function HHCF using the open source software *Gwyddion*. It expresses the correlation of the textured surface to itself at a certain distance and corresponds to the lateral average feature size.

$$f(x) = 2\sigma_{RMS}^2 \left[1 - e^{\left(-\frac{x}{ACL}\right)} \right] \tag{4.8}$$

For further readings see references [48][49][50].

4.2.   Characterization of Solar Cells

4.2.1.   Current-Voltage Measurements

A double source (xenon and halogen lamp) class A solar simulator type *Wacom-WXS-140s-Super* was used to conduct *JV*-measurements. For measurements the solar cell is placed and fixed by aspiration on top of a copper plate which is connected to a temperature controlling system. The contacting pins are coated with gold to achieve a good electrical contact. During a measurement those pins are raised through holes in the sample plate and conduct the back side contact of each solar cell with a cell area of 10×10 mm². The solar cell conversion efficiencies η, the fill factor *FF*, open-circuit voltage V_{oc} and short-circuit current density J_{sc} are determined at standard test conditions (AM 1.5G, 100 mW/cm², 25°C). The ideality factor *n* and saturation current density J_0 are obtained under dark conditions. For calibration a photodiode type *Hamamatsu S1336-BQ* was used.

4.2.2.   External Quantum Efficiency

The external quantum efficiency *EQE* is defined as the probability of a photon with a certain energy to generate an electron/hole pair in the solar cell device which contributes to the current flow:

$$EQE(\lambda) = \frac{J_{ph}(\lambda)}{q\phi(\lambda)} .$$

(4. 9)

$J_{ph}(\lambda)$ is the photo current for a certain wavelength and $\phi(\lambda)$ is the photon flux density per time and *q* is the elementary charge.

The internal quantum efficiency *IQE* considers the solar cell reflectance *R*. It excludes optical losses arising from reflection losses:

$$IQE(\lambda) = \frac{EQE(\lambda)}{(1-R(\lambda))} .$$

(4. 10)

For determination of the *EQE* the spectral response $S(\lambda)$ was determined by the differential spectral response DSR method. The DSR device consists of an identical

double source (class A) solar simulator with additional interference filters, chopper wheel and lock in amplifier. For tandem solar cells the *EQE* of the top cell was measured under red bias light and of the bottom cell was measured under blue bias light. As a bias light source LED arrays were used.

EQE measurements were performed to calculate the top and bottom cell short-circuit current density ($J_{EQE, top}$, $J_{EQE, bot}$). For that purpose, the $EQE(\lambda)$ and $\phi(\lambda)$ product is integrated over the wavelength range under which charge carriers are generated.

$$J_{sc,EQE} = q \int_{\lambda_1}^{\lambda_2} EQE(\lambda) \cdot \phi(\lambda) d\lambda \qquad (4.11)$$

More details to this setup can be found in [51][52].

4.3.   Optical Simulations using Finite-Difference Time-Domain Algorithm

In this work optical simulations were conducted using Finite-Difference Time-Domain (FDTD) method that solves Maxwell's equations rigorously. AFM data gained for each texture served as input parameter for the FDTD simulation. The FDTD method uses a home-built interface to the software package *Meep* [54]. The calculation domain has a lateral size of 4.3×4.3 µm² and uses a grid size of 10 nm. The optical simulations consider a planar electromagnetic wave at normal incidence. A spectrum from 500 nm to 1050 nm is covered in 50 nm steps. The layer stack consists of a glass half space with a refractive index n = 1.5, a front contact layer (TCO), an a-Si:H film with a thickness of 300 nm, an intermediate reflector layer followed by a µc-Si:H film with a thickness of 1500 nm. A ZnO:Al/silver layer stack was used as a back reflector. Due to convergence purposes of the rigorous simulation, the silver was replaced by a perfect electric conductor. More details on the simulation method are given elsewhere [55][56].

Chapter 5
Doped Microcrystalline Silicon Oxide Films for Thin-Film Silicon Solar Cells

5.1   Material Development and Parameter Studies of μc-SiO$_x$:H

In recent years, there has been a continues interest in doped hydrogenated microcrystalline silicon oxide (μc-SiO$_x$:H) for solar cell applications. A number of publications concerning this material can be found for example in reference [7][44] and [57] - [61]. Hydrogenated microcrystalline silicon oxide is a mixed phase material containing a hydrogenated microcrystalline silicon (μc-Si:H) and a hydrogenated amorphous silicon oxide (a-SiO$_x$:H). These two phases result in a material with versatile properties. It has been proposed that the highly doped n- or p-type μc-Si:H phase maintains a high electrical conductivity while the a-SiO$_x$:H phase provides the material's high transparency and low refractive index [60].

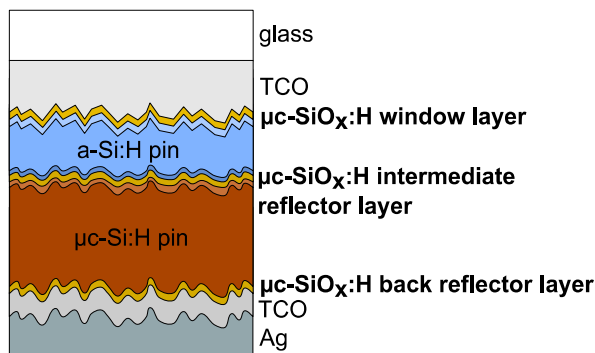Figure 5.1.1: Schematic drawing with possible applications of μc-SiO$_x$:H layers at different positions within a thin-film tandem solar cell.

With its superior optical and electrical properties μc-SiO$_x$:H can be integrated for various purposes at different positions inside thin-film silicon solar cells as shown in Figure 5.1.1. For instance, it can be used as an intermediate reflector layer (IRL) in tandem solar cells containing a hydrogenated amorphous silicon (a-Si:H) top cell and a hydrogenated microcrystalline silicon (μc-Si:H) bottom cell. Here, the IRL provides an increased top cell current, while the a-Si:H i-layer thickness is reduced. That way, an improved long term electrical performance can be obtained due to a reduction of light-induced degradation. The mixed phase material can also function as a transparent p-type window or contact layer in solar cells, where it enhances the light incoupling and electrical contact. Another possible application for doped hydrogenated microcrystalline silicon oxide is the integration as part of the back reflector. Higher transparency, sufficient electrical conductivity, low-ohmic contact to sputtered ZnO:Al and a tunable refractive index make μc-SiO$_x$:H a promising alternative to the commonly used doped silicon layers. In this chapter, the focus will be on the development of n-type and p-type μc-SiO$_x$:H material. Its various applications in thin-film silicon solar cells will be approached in Chapter 6.

n- and p-type microcrystalline silicon oxide films (μc-SiO$_x$:H) have been deposited with a thickness of several hundred nanometres by a large-area RF-PECVD system (30×30 cm^2; 13.56 MHz). The standard parameters for pressure, power density and heater temperature are 13.3 mbar, 0.5 W/cm^2 and 220°C, respectively. The electrode gap is 12.5 mm. The process gases are silane (SiH$_4$), carbon dioxide (CO$_2$) and hydrogen (H$_2$). As dopant gas phosphine (PH$_3$) (5%) diluted in SiH$_4$ for n-type material was used and for p-type material trimethylborane 2.54% (B(CH$_3$)$_3$ or TMB) diluted in helium (He) was used. The silicon oxide films were deposited on glass substrates (*Corning Eagle XG$^®$* glass).

For material characterization a number of methods have been applied that are described in more detail in Chapter 4. Layer thicknesses are determined using a profilometer. Photothermal deflection spectroscopy (PDS*)* was used as a highly sensitive tool for the investigation of optical absorption and determination of the band gap E_{04}. The refractive index *n* at a wavelength of $\lambda = 1000$ nm (n_{1000nm}) was calculated from reflection and transmission measurements using the Fresnel equation. The electrical conductivity was measured in planar direction. For the estimation of the crystalline volume fraction I_c Raman spectroscopy ($\lambda = 488$ nm) was used. The oxygen content in the material was

measured by Rutherford backscattering spectrometry (RBS*)* and is presented as the oxygen/silicon ratio $r_{O, RBS}$.

Commonly, the ratios between certain gas flows ϕ are used to quantify the process gas parameters. The SiH_4/H_2 ratio r_{SiH4} is described as the ratio between the silane gas flow ϕ_{SiH4} and the hydrogen flow ϕ_{H2}:

$$r_{SiH4} = \frac{\phi_{SiH_4}}{\phi_{H_2}}$$
(5.1)

The CO_2 concentration is described as the ratio between CO_2-flow ϕ_{CO2} and the SiH_4-flow ϕ_{SiH4}:

$$r_{CO_2} = \frac{\phi_{CO_2}}{\phi_{SiH_4}}$$
(5.2)

Likewise, the phosphine concentration is quantified as:

$$r_{PH_3} = \frac{\phi_{PH_3}}{\phi_{SiH_4}}$$
(5.3)

The ratio between the TMB-flow ϕ_{TMB} and the SiH_4-flow ϕ_{SiH4} is used to quantify the TMB concentration:

$$r_{TMB} = \frac{\phi_{TMB}}{\phi_{SiH_4}}$$
(5.4)

Because PH_3 is diluted in SiH_4 (5%) and TMB is diluted in He (2.54%) the net flows are only a certain percentage of the value set for the mass flow controller. In the following, all gas flows are presented as net gas flows ratios.

Electron Microscopy of µc-SiO$_x$:H layers

Microcrystalline silicon oxide contains a microcrystalline silicon (µc-Si:H) and an amorphous silicon oxide (a-SiO$_x$:H) phase. It is proposed in literature [44] that the µc-Si:H phase provides a high electrical conductivity while the a-SiO$_x$:H phase improves the transparency and decreases the refractive index of the mixed phase material. As reported in [60] and [5], filament-like silicon nano-crystallites (seen by EELS and EFTEM) which grow perpendicular to the substrate can enhance the transverse conductivity, even though the planar conductivity is low. To provide an idea of the materials structure, Figure 5.1.1 shows a microscopic image obtained by high resolution transmission electron microscopy (HRTEM) with sub-nanometer resolution.
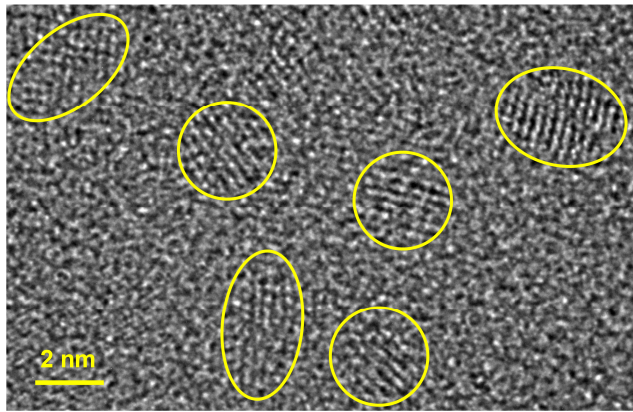
Figure 5.1.1: HRTEM images of p-type µc-SiO$_x$:H with randomly orientated silicon crystallites embedded in an amorphous matrix.

From the HRTEM images crystalline regions in the size of several nanometers embedded within a predominantly amorphous matrix can be seen. Moreover, atom patterns within crystallites are made visible by the high magnification. The microscopic images are taken for a single layer of ~30 nm thickness. They reveal that crystallites are orientated in a random way.

5.2 Material Properties of n-type µc-SiO$_x$:H

In this chapter, results on the development of n-type microcrystalline silicon oxide material, fabricated by PECVD as single layers, are presented. Material properties as a function of variation of the SiH$_4$/H$_2$-ratio r_{SiH4}, the CO$_2$/SiH$_4$-ratio r_{CO2}, and the PH$_3$/SiH$_4$-ratio r_{PH3} are shown. An overview of deposition parameters is given in Table 5.2.1.

Table 5.2.1: Overview of the PECVD process parameters for the n-type µc-SiO$_x$:H layers deposited on glass substrates.

power density [W/cm²]	f [MHz]	p [mbar]	T [°C]	r_{SiH4} [%]	r_{CO2} [-]	r_{PH3} [-]
0.5	13.56	13.3	220	0.26 – 0.48	1 – 6.4	0.003 – 0.03

5.2.1 Influence of the CO$_2$/SiH$_4$ and the SiH$_4$/H$_2$-ratio
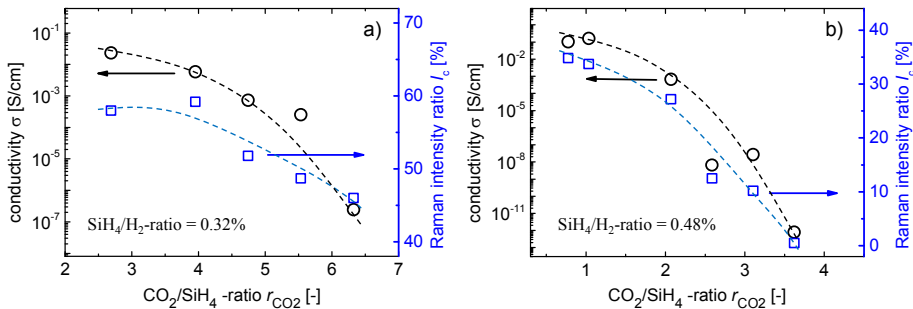
Figure 5.2.2: Conductivity and Raman intensity ratio as function of CO$_2$/SiH$_4$-ratio r_{CO2} a) for a SiH$_4$/H$_2$-ratio of 0.32% and b) for a SiH$_4$/H$_2$-ratio of 0.48%. The circles represent the conductivity σ and the squares represent Raman intensity ratio I_c.

Two series varying r_{CO2} for various SiH$_4$/H$_2$-ratios are presented. In Figure 5.2.2 a) the electrical conductivity as well as the Raman crystallinity are presented as a function of r_{CO2}. Figure 5.2.2 b) shows a similar plot for a higher SiH$_4$/H$_2$-ratio of 0.48%. The trends seen for both cases are the same. In the case of SiH$_4$/H$_2$-ratio of 0.32% the conductivity decreases from the order of 10^{-2} S/cm to 10^{-7} S/cm with increasing r_{CO2} from 2.6 to 6.4. At the same time, a decrease of I_c from 60% to 45% is observed. In the case of a higher r_{SiH4} the changes are more pronounced. The increase of r_{CO2} from 1 to 3.6 leads to a strong

decrease of the conductivity from 10^{-1} S/cm to 10^{-12} S/cm, while I_c is reduced from 35% to 0%.

In the following section the investigations aim to the interplay between optical and electrical material properties. Results for different CO_2/SiH_4-ratios are illustrated in Figure 5.2.3, while in a) σ is plotted versus the band gap energy E_{04} and in b) σ is plotted versus the refractive index n. Different r_{SiH4} are marked by different colors.
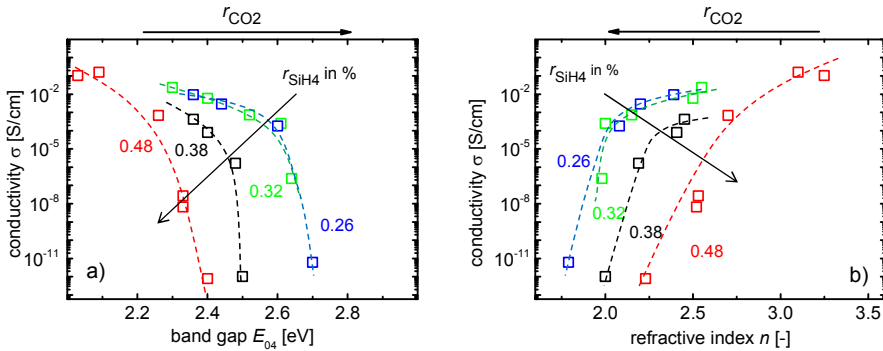
Figure 5.2.3: a) Electrical conductivity σ as a function of the band gap energy E_{04} for n-type µc-SiOx:H thin films with various SiH4/H2-ratios. b) Electrical conductivity σ as a function of refractive index $n@1000$ nm. The directions of r_{CO2} increase are indicated with arrows. Dashed curves are a guide to the eyes.

In Figure 5.2.3 a) the electrical conductivity σ is shown as a function of the band gap energy E_{04}. While r_{CO2} increases it is seen that σ declines. At the same time E_{04} is enlarged. This is the case for all r_{SiH4}. The same effects are seen for the refractive index, shown in b). Higher r_{CO2}, going from the right to left, lead to reduction of n simultaneously with a reduction of σ. Also, the figures show effects linked to variations of r_{SiH4}. By decreasing r_{SiH4} the optical parameters are pushed to more favorable regimes, while the materials maintain high conductivities. For $r_{SiH4} = 0.32$% saturation occurs, meaning that for lower r_{SiH4} the conductivity is not improved. Also, the band gaps are not enlarged and the refractive index is not decrease further.

Figure 5.2.4 shows a decrease of the deposition rate while r_{SiH4} is reduced and all other process parameters are held constant. Furthermore, it is seen that within a series with fixed r_{SiH4} larger CO_2-flows slightly improves the growth rate.
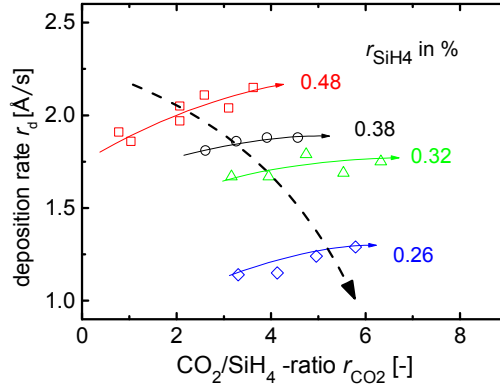
Figure 5.2.4: Deposition rate r_d of n-type µc-SiO$_x$:H films as a function of the CO_2/SiH_4 -ratio r_{CO2} for various SiH_4/H_2-ratios.

As shown before, the variation of the r_{CO2} are connected to various effects and alters the material properties of µc-SiO$_x$:H. Therefore, it is also important to known the composition of the material and most of all its oxygen content.
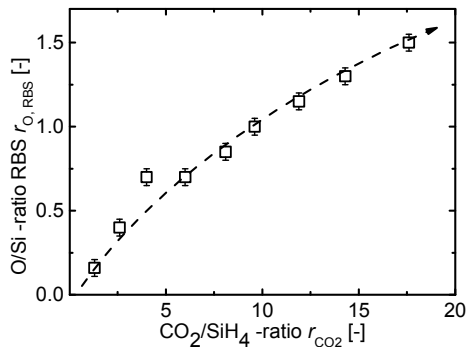
Figure 5.2.5: Oxygen/silicon ratio $r_{O,RBS}$ measured by RBS and plotted as a function of CO_2/SiH_4-ratio r_{CO2}.

In Figure 5.2.5 the oxygen/silicon ratio measured by RBS $r_{O,RBS}$ are shown as a function of r_{CO2}. $r_{O,RBS}$ increases with increasing r_{CO2} over a wide range. It is seen that an oxygen content, up to $r_{O,RBS} = 1.5$, was incorporated into the film by plasma-enhanced chemical vapor deposition with very high admixtures of CO_2.

5.2.2 Influence of the PH$_3$/SiH$_4$-ratio
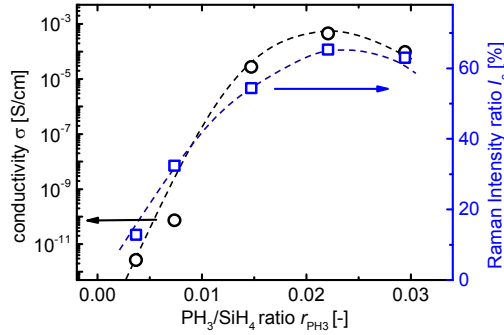
Figure 5.2.6: Conductivity σ and Raman intensity ration I_c of n-type μc-SiO$_x$:H films versus the PH$_3$/SiH$_4$-ratio r_{PH3}. The circles represent the conductivity σ and the squares represent Raman intensity ratio I_c. In this series the SiH$_4$/H$_2$-ratio r_{SiH4} was kept constant at 0.0026 and the CO$_2$/SiH$_4$-ratio r_{CO2} at 3.9. The dashed lines are a guide to the eyes.

In the next section, the effect of the PH$_3$/SiH$_4$-ratio r_{PH3} is investigated while r_{CO2} and r_{SiH4} are kept constant at 3.9 and 0.0026. In Figure 5.2.6 the conductivity σ and Raman intensity ration I_c of n-type μc-SiO$_x$:H films are shown as a function of r_{PH3}. The Raman intensity ratio increases with increasing proportion of PH$_3$ until a maximum of 65% is reached for r_{PH3} = 0.0022. For higher r_{PH3} the crystallinity decreases again. The electrical conductivity increases by increasing r_{PH3}. Both material properties behave similarly to the admixture of PH$_3$. Variations on r_{PH3} do not affect the optical properties in a strong way. The band gap E_{04} for all samples in this series is between 2.5 eV and 2.6 eV and the refractive index amounts to ~1.9.

Discussion

Results show that conductivity and crystallinity are highly influenced by the admixture of CO$_2$. Also, it is seen that the electrical conductivity is linked to the crystallinity of the material. The formation of larger fractions of a-SiO$_x$:H and therefore the decrease of the fraction of μc-Si:H leads to the reduction of electrical conductivity. When the crystallinity is decreased to 0% the silicon oxide material becomes an insulator with a conductivity of 10^{-12} S/cm. At the same time E_{04} is enlarged. This is caused by an increased formation of amorphous silicon oxide fraction. A lower SiH$_4$/H$_2$-ratio however,

enhances the formation of the crystalline fraction and the material maintains a high I_c and high σ even for higher r_{CO2}. The improvements of the optical properties are linked to the formation of large fractions of silicon oxides which would normally decrease the electrical conductivity. But the high crystalline volume fraction, rendered possible by a low r_{SiH4}, neglects this effect and act positively on the electrical performance.

It is also seen that the deposition rate decreases when r_{SiH4} is reduced while all other process parameters are held constant. Such a slowdown might also favor the crystal growth, because it gives the silicon containing specimen time to orientate and nucleate. It is seen that higher r_{CO2} result in a slight improvement of the deposition rate. This is because of the additional oxygen specimen in the plasma which are also incorporated into the $\mu c\text{-}SiO_x\text{:}H$ layer. A deposition rate to > 2 Å/s makes $\mu c\text{-}SiO_x\text{:}H$ fabricated by PECVD an industrial applicable material.

From the oxygen/silicon ratio measured by RBS $r_{O,RBS}$ it is seen that an oxygen content, up to $r_{O,RBS} = 1.5$, can be incorporated into the film by plasma-enhanced chemical vapor deposition with very high admixtures of CO_2. However, this material would not fulfil the requirements for a sufficiently conductive material suitable for the application in a thin-film silicon solar cell any more. For solar grade material, $r_{O,RBS}$ is required to be < 1.

Similar trends are also seen in literature [44]. A trade-off between optical and electrical properties becomes evident when plotting the conductivity as a function of E_{04} or n. Comparing to that early work, the materials deposited in this PECVD system show a higher amount of incorporated oxygen into the matrix. Also, for higher CO_2/SiH_4-ratios the conductivity remains in a high level, which can be explained by the low SiH_4/H_2-ratio in the processes, shown in Figure 5.2.2. This results in good optical properties while the electrical properties were kept in a sufficiently high solar grade level. Comparing to more recent publications [59] it is seen that the n-type $\mu c\text{-}SiO_x\text{:}H$ films produced in the large area PECVD system has equivalently high quality material characteristics.

It is seen that the admixture of PH_3 causes an increase of the crystallinity to a certain extend and simultaneously an improvement of the conductivity. Those material characteristics are in agreement with the literature [61].

5.3   Material Properties of p-type µc-SiO$_x$:H

In this chapter, investigations of p-type microcrystalline silicon oxide, fabricated by PECVD as single layers, are shown. Changes concerning optical and electrical properties that have been caused by the variation of CO_2/SiH_4-ratio r_{CO2} and the dopant gas (TMB) concentration r_{TMB} are presented.

From the previous development of n-type µc-SiO$_x$:H, it is seen that a high hydrogen dilution is important to produce highly transparent and highly conductive material. This effect has also been reported on p-type µc-SiO$_x$:H in literature [66]. Therefore, in order to produce material with a high crystalline volume fraction, the SiH_4/H_2-ratio r_{SiH4} was kept at a constantly low level of 0.21%, while process parameters like CO_2/SiH_4-ratio r_{CO2} and TMB/SiH$_4$-ratio r_{TMB} are tuned. For variations done for r_{CO2}, the r_{TMB} was set at 0.005. For variations done for r_{TMB}, the r_{CO2} was set at 2.4. An overview of deposition parameters is given in table 5.3.1.

Table 5.3.1: Overview of the PECVD process parameters for the p-type µc-SiO$_x$:H layers deposited on glass substrates.

power density [W/cm²]	f [MHz]	p [mbar]	T [°C]	r_{SiH4} [%]	r_{CO2} [-]	r_{TMB} [-]
0.5	13.56	13.3	220	0.26	1.2 - 6.0	0-0.036

5.3.1 Influence of the CO$_2$/SiH$_4$ and the TMB/SiH$_4$-ratio

Figure 5.3.1 a) shows the conductivity σ as a function of the band gap E_{04} for p-type µc-SiO$_x$:H. A broad range of E_{04} and σ can be achieved with variation of the CO_2/SiH_4-ratio, indicated by an arrow at the top of the graph. By increasing r_{CO2} from 1.2 to 6 the band gap increases from 2.2 to 2.8 eV. In the course of parameter variations, the refractive index n decreases from 2.6 to 1.6, as shown in Figure 5.3.1 b). Also, the conductivity drops from 10^{-2} to 10^{-12} S/cm by increasing r_{CO2}.
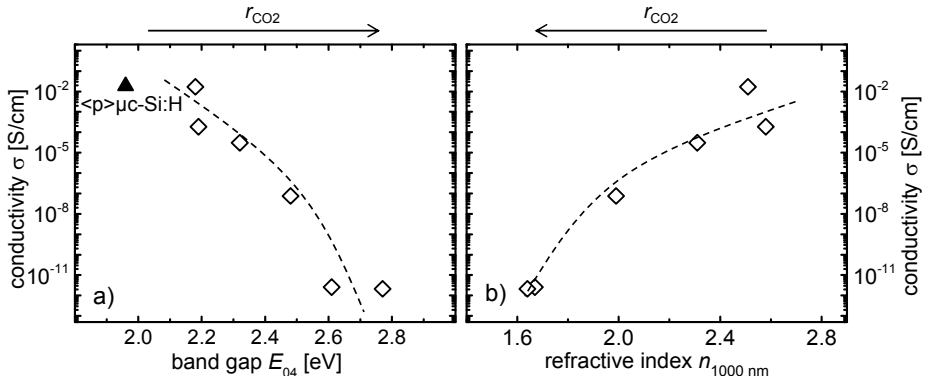
Figure 5.3.1: a) Conductivity σ as a function of band gap energy E_{04} for various μc-SiO$_x$:H films. b) Conductivity σ as a function of refractive index $n_{1000\,nm}$. The increase in CO_2/SiH_4 ratio is indicated by an arrow at the top of the graph.

Figure 5.3.2 shows the electrical conductivity σ and Raman crystallinity I_c of p-type μc-SiO$_x$:H films as a function of the r_{CO2} in a) and as a function of r_{TMB} in b). To provide a sufficient conductivity of the p-type μc-SiO$_x$:H film a certain crystalline volume fraction is required, as also reported in references [58] and [66]. When no oxygen is added into the system, hydrogenated microcrystalline silicon can reach a Raman intensity ratio I_c of over 90%. However, I_c of the p-type μc-SiO$_x$:H films go above 50% for a r_{CO2} of 1.2 while an increase of the CO_2 amount leads to a decrease of the crystallinity. For an r_{CO2} higher than 3.6 the crystalline volume fraction turns to almost 0%. With the decrease of the I_c also σ drops rapidly. With very high r_{CO2} the conductivity decreases to 10^{-12} S/cm.
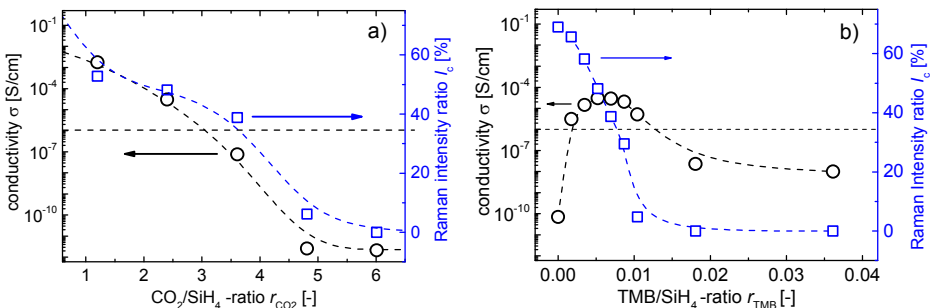
Figure 5.3.2: Conductivity σ and Raman intensity ration I_c of p-type μc-SiO$_x$:H films versus a) the CO_2/SiH_4-ratio r_{CO2} and b) the TMB/SiH$_4$-ratio r_{TMB}. The dashed lines mark the required conductivity for solar grade material. The circles represent the conductivity σ and the squares represent Raman intensity ratio I_c.

Another important process parameter for the development of p-type $\mu c\text{-SiO}_x\text{:H}$ is the TMB gas flow, which is the dopant source. Figure 5.3.2 b) shows a sharp decrease of the crystalline volume fraction I_c from 69% to 5% by increasing the TMB/SiH$_4$-ratio r_{TMB} from 0 to 0.01 in small steps. For higher r_{TMB} values the material becomes fully amorphous. From this figure it is also apparent that the conductivity of the material is in the range of 10^{-10} S/cm, when no dopant was added. With the admixture of a small amount of TMB ($r_{TMB} = 0.002$) the conductivity increases to 10^{-6} S/cm. The maximum of σ is found for $r_{TMB} = 0.005$ at $\sigma = 3 \times 10^{-5}$ S/cm. For values, $r_{TMB} < 0.005$, a TMB admixture improves the conductivity due to an increase in the dopant concentration. However, a further increase of TMB leads to a reduction of the crystalline volume fraction and with that a decrease of σ. For fully amorphous materials, σ remains at a level of $\sim 10^{-8}$ S/cm.
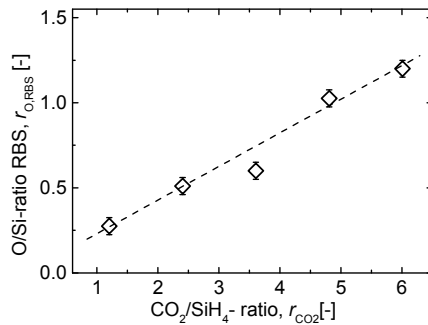
Figure 5.3.3: Oxygen/silicon ratio determined by *RBS* measurement $r_{O,RBS}$ plotted as a function of the CO$_2$/SiH$_4$- ratio r_{CO2}. The dashed line is a guide to the eye.

Figure 5.3.3 shows the oxygen/silicon ratio $r_{O,RBS}$ as a function of the CO$_2$/SiH$_4$-ratio r_{CO2}. A linear dependency between both parameters can be seen, meaning that r_{CO2} directly correlates with the amount of oxygen atoms built into the $\mu c\text{-SiO}_x\text{:H}$ material within the investigated range.

5.3.2 Influence of power density, pressure and temperature on the material properties of p-type $\mu c\text{-}SiO_x\text{:}H$

Starting from previous investigations, where the tunability of optical and electrical properties of microcrystalline silicon oxide through controlled changes of the CO_2/SiH_4 and the TMB/SiH_4-ratios are shown. This subchapter focuses on the influence of process parameters like power density, pressure and temperature. In the following series, all gas flows were kept constant for all experiments. The standard parameters are 0.5 W/cm² for the power density, 13.3 mbar for the pressure and 220°C for the heater temperature. In Table 5.3.2 the ranges, for which the process parameters are varied, are listed as an overview.

Table 5.3.2: Overview of the PECVD process parameters for p-type $\mu c\text{-}SiO_x\text{:}H$ layers deposited on glass substrates.

power density [W/cm²]	f [MHz]	p [mbar]	T [°C]	r_{SiH4} [%]	r_{CO2} [-]	r_{TMB} [%]
0.22 - 0.56	13.56	2.7 - 13.3	160 - 240	0.26	2.4	0.14

Influence of Power Density

In Figure 5.3.4 electrical conductivity σ, Raman intensity ratio I_c, optical band gap E_{04} and the refractive index are shown as a function of the power density ψ coupled into the plasma during the PECVD process. Measurements reveal that σ behaves reciprocal to ψ. For a power density below 3.7 W/cm² the conductivity is above 10^{-3} S/cm, while higher power densities lead to a reduction to 10^{-4} S/cm. Further, a correlation is seen for the Raman intensity ratio. A fully amorphous material is deposited when applying low power. Higher crystallinities up to an I_c of >50% are reached when the power density is increased. An almost linear correlation is seen between the power density and band gap E_{04}. The band gap changes from 2.1 eV to 2.3 eV with increasing ψ. At the same time, a reduction of the refractive index n from 3.0 to 2.4 is observed when tuning ψ from 0.22 W/cm² to 0.45 W/cm². For further increase of ψ no change on n is observed.
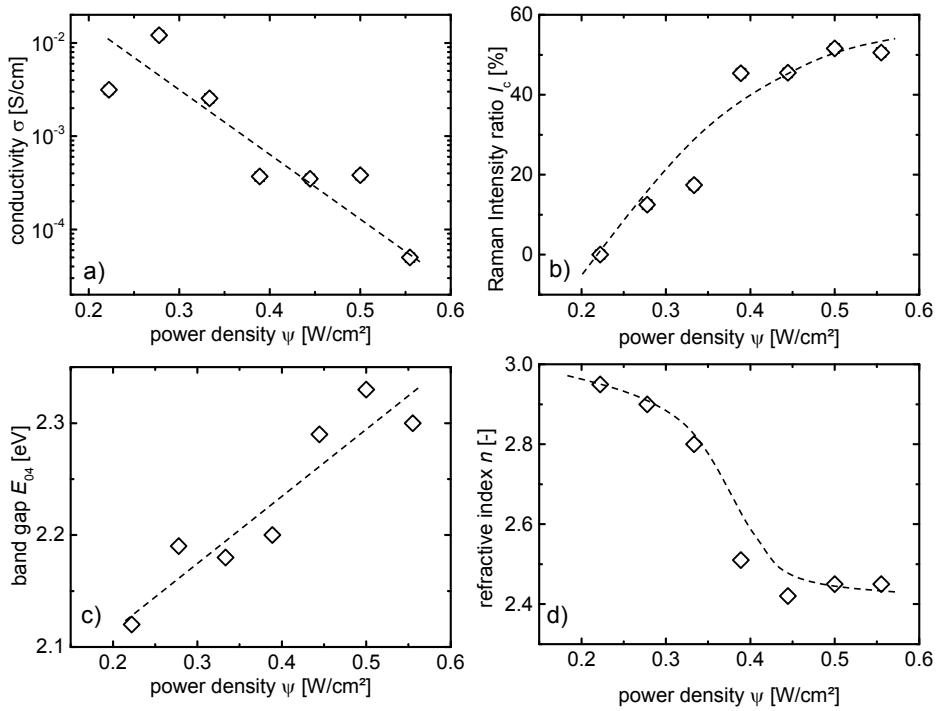
Figure 5.3.4: Influence of the power density applied at the PECVD process on a) conductivity σ; b) Raman intensity ratio I_c; c) band gap E_{04}; d) refractive index n. The dashed lines are a guide to the eyes.
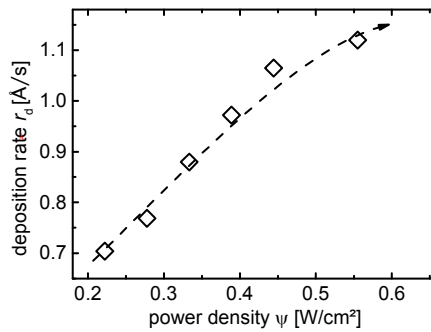
Figure 5.3.5: Deposition rate as a function of the power density ψ for p-type μc-SiO_x:H films.

Figure 5.3.5 shows the deposition rate of p-type μc-SiO_x:H films as a function of the applied power density. It is seen that when increasing ψ from 0.22 W/cm² to 0.55 W/cm² the deposition rate increases steadily from 0.7 Å/s to 1.1 Å/s.

Influence of Pressure
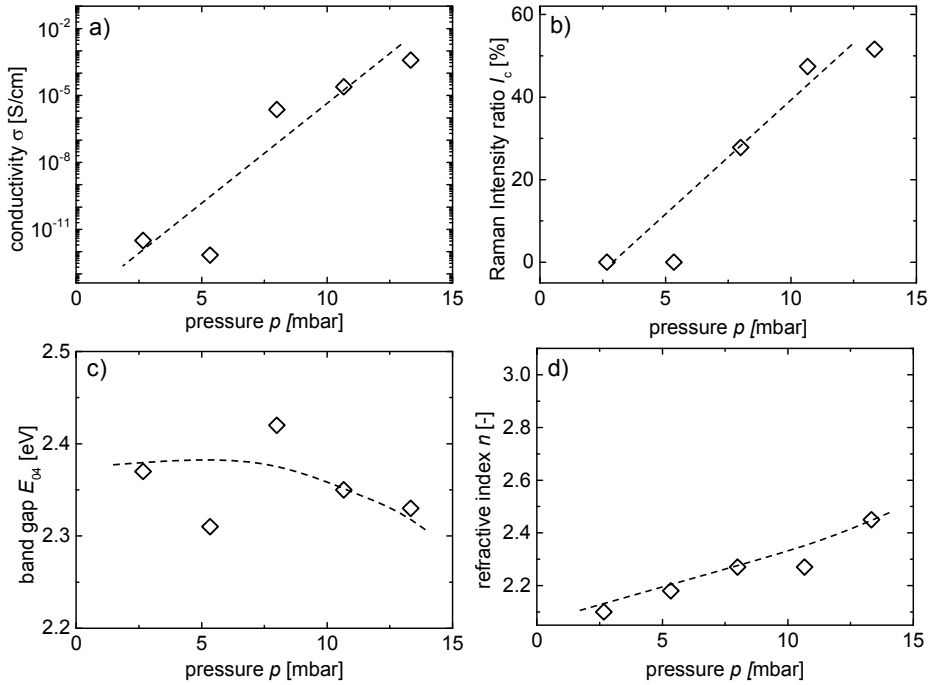
Figure 5.3.6: Influence of pressure on a) conductivity σ; b) band gap energy E_{04}; c) refractive index n and d) Raman intensity ratio I_c. The dashed lines are a guide to the eyes.

In Figure 5.3.6 the influence of the process pressure on the material properties of p-type $\mu c\text{-SiO}_x\text{:H}$ films is shown. It is seen that for a pressure below 6.6 mbar, the electrical conductivity σ is very low ($\sim 10^{-12}$ S/cm). For higher pressures the conductivity increases to above 10^{-4} S/cm. With a low pressure of below 6.6 mbar the material grows mainly amorphous. With increasing pressure the Raman intensity ratio I_c of p-type $\mu c\text{-SiO}_x\text{:H}$ increases and amounts to >50% for material deposited at a pressure of 13.3 mbar. It is also seen that the chamber pressure has only a minor influence on the band gap E_{04}. Here, a small decrease is observed with increasing pressure, but the band gap E_{04} remains in the range of 2.3 eV and 2.4 eV. The refractive index n increases linearly from 2.1 to 2.5 with an increase of pressure from 2.6 to 13.3 mbar.
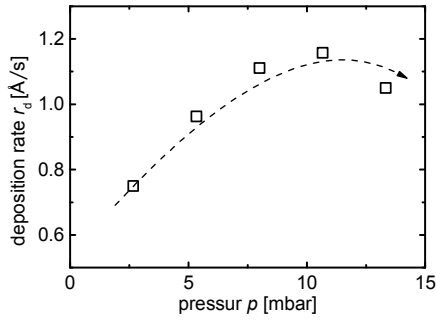
Figure 5.3.7: Deposition rate as a function of PECVD deposition pressure p.

In Figure 5.3.7 the impact of the pressure on the deposition rate of p-type μc-SiO$_x$:H films is shown. It is seen that higher pressures lead to an increasing deposition rate and peaks at ~10 mbar.

Influence of Heater Temperature
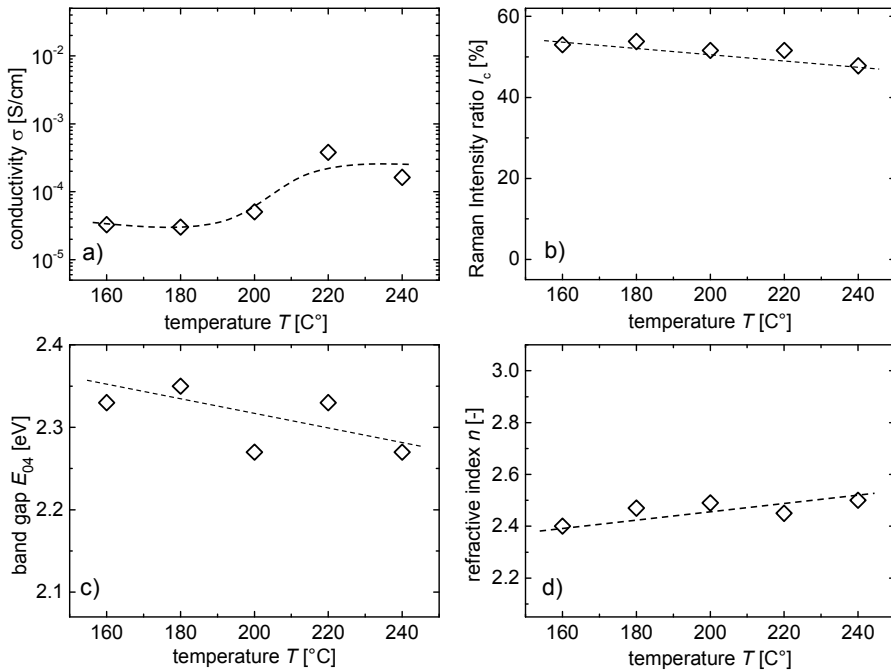
Figure 5.3.8: Influence of heater temperature on a) conductivity σ; b) band gap energy E_{04}; c) refractive index n and d) Raman intensity ratio I_c. The dashed lines are a guide to the eyes.

The impact of variations of the heater temperature during the PECVD process on various material properties is shown in Figure 5.3.8. Since, it is not possible to measure the substrate temperature in the LA-PECVD system, therefore, the heater temperature is taken as a process parameter. It is seen that an increase of the temperature leads to a small improvement for the electrical conductivity from about 10^{-5} S/cm (160°C) to over 10^{-4} S/cm (240°C). A maximum is seen for a temperature of 220°C. The temperature has a small impact on the crystallinity of p-type μc-SiO$_x$:H. For a temperature range from 160°C to 240°C, the Raman intensity ratio I_c decreases from 55% to 50%. The temperature does not have a strong influence on the optical band gap E_{04}. A minor decrease is observed here when increasing the temperature by over 80°C (from 2.27 eV to 2.35 eV). Also, the refractive index n is not strongly influenced by temperature variations. n increases slightly from 2.4 to 2.5 by increasing the temperature from 160°C to 240°C.
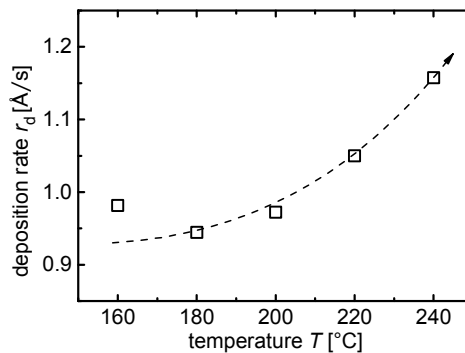
Figure 5.3.9: Deposition rate r_d as a function of the heater temperature T.

In Figure 5.3.9 the impact of the temperature on the deposition rate is shown. It is seen that higher temperature result in an increase of the deposition rate. Within a range of 60°C the deposition rate increases approximately by 20%.

Discussion

The optical properties of p-type μc-SiO$_x$:H films can be tuned by adapting deposition parameters e.g. the CO$_2$/SiH$_4$-ratio. As already seen previously in Chapter 5.2.1 from the variation of the CO$_2$ for n-type material the increased incorporation of oxygen into the compound material leads to a reduction of the refractive index while the band gap is enlarged. At the same time, when improving the optical transparency the electrical conductivity declines. A low conductive material is not suitable for the application in a solar cell device without a significant reduction of the fill factor. Here, it is apparent that there is a trade-off between transparency and electrical conductivity. From literature it is known that window layers for solar cell applications should have a minimum lateral conductivity of 10^{-6} S/cm when prepared as several hundred nanometer thick single layer on glass [62]. Therefore, r_{CO2} has to be chosen in a way resulting in a wider band gap for a higher transparency, a low refractive index and at the same time a sufficient electrical conductivity.

When varying the TMB/SiH$_4$-ratio in small steps it is seen that r_{TMB} strongly influences the crystallinity. Also, the amount of TMB sensitively affects the material's electrical conductivity. To be more precise, a certain amount of TMB is needed to provide a high conductivity, whereas too much of it reduces the crystallinity and with that the conductivity. Therefore, an optimized amount of dopant concentration is essential. This is also in agreement with results from the literature [63].

Similar trends for optical and electrical properties as seen for r_{CO2} variations have also been observed when the power density ψ is changed. It is seen that when the power density is increased the band gap are enlarged while refractive index and conductivities are reduced. Only the Raman intensity ratio behaves differently as compared to increasing r_{CO2}. It is seen that I_c decreases with increasing ψ. Therefore, the oxygen/silicon ratio of μc-SiO$_x$:H that has been deposited with various power densities was measured by RBS. The results are shown in Figure 5.3.10.
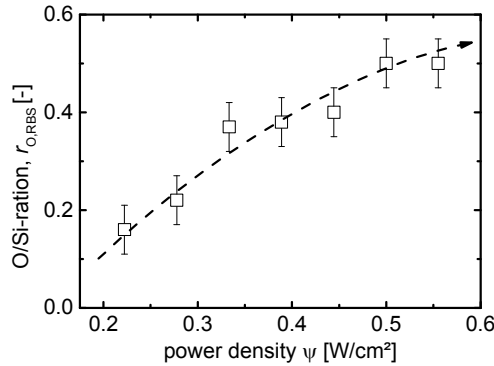
Figure 5.3.10: Oxygen/silicon ratio of p-type μc-SiO$_x$:H films determined by RBS measurement $r_{O,RBS}$ as a function of applied power density during the PECVD process.

It is seen that materials deposited with higher power densities also incorporate a higher amount of oxygen. Here, the process gas composition has not been changed. It means that binding oxygen and therefore, the formation of an oxygen rich phase for improved optical properties is linked to a sufficiently high power density applied during the deposition. Furthermore, it is observed that higher power densities lead to larger crystalline fractions. Unlike in previous results, where an increased I_c also resulted in higher conductivity, a decrease of σ is observed here (Figure 5.3.4 a)). Despite the increase of the crystalline fraction the electrical conductivity declines due to enhanced incorporation of oxygen atoms into the multi-phase material. It shows that the effect of oxygen incorporation has a more dominant effect on the electrical conductivity than the effect of an enhanced crystalline growth.

In Figure 5.3.5 it is seen that an increased power density leads to a higher deposition rate. It is known that a higher power density as well as a higher pressure increases the deposition rate of μc-Si:H layers [36][73]. Another reason for the faster deposition g rate might be the larger amount of oxygen atoms that can be incorporated into the matrix due to the increased power density.

5.4 Conclusion

In Chapter 5 results of the material development of n-type and p-type μc-SiO_x:H are presented. Starting with the n-type material, it is shown that microcrystalline silicon thin films with a conductivity of 10^{-2} S/cm and a crystalline volume fraction of around 55% can be fabricated by decreasing the SiH_4/H_2-ratio and adjustment of the CO_2/SiH_4-ratios. Also, the energy band gap could be modified between 2.1 to 2.7 eV and correspondently the refractive index from 3.3 to 1.8. The decrease of the SiH_4/H_2-ratio results in a shift to higher electrical conductivity, larger band gap and smaller refractive index. The admixture of PH_3 causes an increase of the crystallinity to certain extend and simultaneously an improvement of the conductivity. Unlike for r_{SiH4} or r_{CO2} variations changes on r_{PH3} do not affect the optical properties in a strong way.

In a next step, p-type μc-SiO_x:H layers were fabricated with a conductivity of up to 10^{-2} S/cm and a Raman crystallinity of above 60%. Furthermore, p-type μc-SiO_x:H films with a broad range of optical properties (2.1 eV $< E_{04} <$ 2.8 eV and $1.6 < n < 2.6$) are presented. It is shown that solar grade material ($\sigma > 10^{-6}$ S/cm) can be produced with a proper transparency and reflective index. The admixture of oxygen reduces the crystallinity (Figure 5.3.2 a)) and therefore, the electrical conductivity of the films. For p-type μc-SiO_x:H layers a CO_2/SiH_4-ratio r_{CO2} of 2.4 ($r_{O,RBS} = 0.5$) or lower is crucial for applications in a solar cell. Additionally, when varying r_{TMB} in small steps it was seen that a strong influence of the dopant on the electrical conductivity becomes apparent. First, the admixture of dopant increases the material's electrical conductivity. When increasing r_{TMB} further the crystallinity is reduced. A high conductivity can only be established with a certain crystalline volume fraction. Thus, the optimization of r_{TMB} is a crucial step in the material development process.

Finally, the effects on the material properties caused by variations of the power density, pressure and temperature were investigated. The amount of oxygen that is bound into the matrix is highly related to the applied power density. Therefore, the power density has a very large effect on optical as well as electrical material properties. The applied pressure affects the crystalline growth of p-type μc-SiO_x:H films and thus, it influences the electrical conductivity. It is seen that the heater temperature shows only minor effects on various material properties.

Applications of p- and n-type μc-SiO_x:H layers with different functions in thin-film silicon solar cells will be presented in Chapter 6.

Chapter 6
Applications of doped Microcrystalline Silicon Oxide in Thin-Film Silicon Solar Cells

6.1   p-type µc-SiO$_x$:H applied as Window Layers in Thin-Film Silicon Solar Cells

In the previous chapter, where the tunability of optical and electrical properties of p-type µc-SiO$_x$:H by controlled changes of the CO_2/SiH_4 and the dopant gas flow ratios are shown, the focus in this chapter is on the application of p-type µc-SiO$_x$:H as window layers in a-Si:H and µc-Si:H solar cells.

The state-of-the-art p-type layer stack, which is used in single-junction amorphous or in tandem solar cells fabricated on sputtered aluminum doped zinc oxides (ZnO:Al) front side TCO [29][34], includes a p-type µc-Si:H contact layer and a p-type amorphous silicon carbide (a-SiC:H) layer. It provides a low-ohmic TCO/p contact, as discussed elsewhere [61], but causes additional parasitic absorption [60][65]. In order to reduce the parasitic absorption, a p-type µc-SiO$_x$:H material with a high transparency and sufficient conductivity was developed and applied as a window layer.

6.1.1 p-type μc-SiO$_x$:H as Window Layer for a-Si:H Solar Cells

Figure 6.1.1 shows a schematic drawing of a hydrogenated amorphous silicon (a-Si:H) single-junction solar cell with a p-type μc-Si:H layer acting as a contact layer at the ZnO/Si interface. In the following chapters results are shown on approaches made to substitute the p-type μc-Si:H layer by a p-type μc-SiO$_x$:H layer to minimize optical absorption losses. Solar cells were deposited with various p-type layer configurations and variations of the layer thicknesses. For the application of p-type μc-SiO$_x$:H layer in solar cells a CO$_2$/SiH$_4$-ratio of 2.4 and TMB/SiH$_4$-ratio of 0.14% were used. The applied p-type μc-SiO$_x$:H layers contain an oxygen/silicon ratio $r_{O,\,RBS}$ of 0.5.
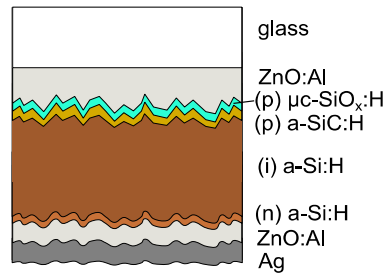
Figure 6.1.1: Schematic drawing of a standard single junction a-Si:H solar cell deposited with a p-type μc-SiO$_x$:H contact layer on ZnO:Al coated glass and ZnO:Al/Ag as back contact.

The development of p-type μc-SiO$_x$:H layers applied in solar cells were carried out on sputtered ZnO:Al as front TCO, which was wet-chemically etched in diluted hydrochloric acid (HCl) for texturing the materials surface. Details are shown elsewhere [29][34]. The solar cell thickness is kept constant at 350 nm.

In Figure 6.1.2 the external quantum efficiency *EQE* and the corresponding absorptance spectra of a-Si:H solar cells with different p-type layers is shown. The different stacks include a p-type μc-Si:H contact layer with p-type a-SiC:H layer (reference), only a p-type a-SiC:H layer, a p-type μc-SiO$_x$:H contact layer with p-type a-SiC:H layer and a p-type μc-SiO$_x$:H contact layer with a thin p-type a-SiC:H layer. From the absorptance curves it is seen that no decrease in cell reflection was achieved by implementing a μc-SiO$_x$:H window layer. However, the *EQE* spectra, especially in the short wavelength range, reveal some differences between various layer stacks. The a-Si:H solar cell without a contact layer in front of the p-type a-SiC:H layer show a clearly

higher *EQE* in the wavelength range from 350 nm to 600 nm compared to the reference. The difference between these configurations is caused by additional absorption losses from the p-type μc-Si:H contact layer. μc-SiOₓ:H was applied to substitute this layer. It is seen that the quantum efficiency of the solar cell with a p-type μc-SiOₓ:H layer is increased in a way that it is similar to the solar cell with only a p-type a-SiC:H layer. In order to reduce the parasitic absorption in the p-type layer of a-Si:H solar cells, further approaches are made. Certainly, the p-type a-SiC:H layer also absorbs incoming light which then cannot contribute to the charge carrier separation in the intrinsic layer. Therefore, a reduction of its thickness has been obtained. The most distinct change is revealed by the layer stack consisting of a p-type μc-SiOₓ:H contact layer with a thin p-type a-SiC:H layer. The *EQE* in a wavelength range from 350 nm to 550 nm is clearly improved. The *JV*-measurements show a fill factor of 60% for solar cells with only a p-type a-SiC:H layer; 68.2% for the reference; and 69.3% for a 8 nm thick μc-SiOₓ:H.
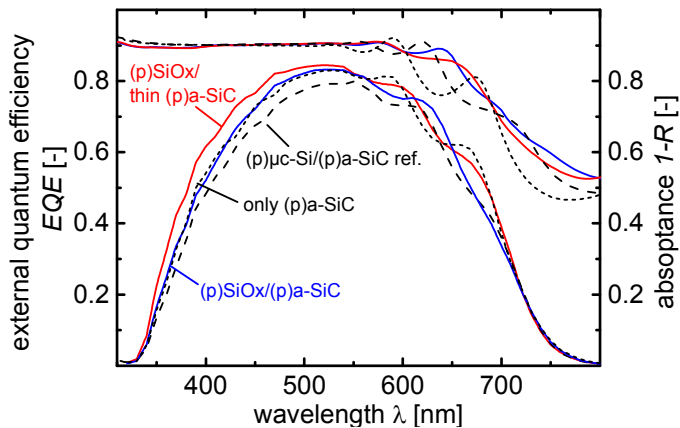
Figure 6.1.2: External quantum efficiency (*EQE*) and absorptance of a-Si:H solar cells without contact layer, i.e. only p-type a-SiC:H layer; with p-type μc-Si:H contact layer (reference); with p-type μc-SiOₓ:H contact layer; with p-type μc-SiOₓ:H contact layer and a thin p-type a-SiC:H layer. All solar cells are deposited on single textured ZnO:Al front contact.

Besides the improvements of the optical properties of a solar cell it is also important to advance the electrical properties further. This was realized by a layer stack consisting of a p-type μc-SiOₓ:H; thin p-type μc-Si:H and a thin p-type a-SiC:H. The photovoltaic parameters are shown in Figure 6.1.3. The reference solar cell consisting of a p-type μc-Si:H contact layer and a p-type a-SiC:H layer shows a conversion efficiency of 9.4%.

The fill factor is 68.2% and the open circuit voltage V_{oc} amounts to 935 mV. The short-circuit current density J_{sc} is relatively low with only 14.8 mA/cm². Compared to that, the p-type µc-SiO$_x$:H window layer with a p-type a-SiC:H shows an slightly improved J_{sc} of 15.0 mA/cm². The *FF* is improved to 69.3%, while the V_{oc} is reduced to 925 mV. Thus, the conversion efficiency is improved to 9.6%. The highest J_{sc} (16.0 mA/cm²) is seen for solar cells with only a p-type µc-SiO$_x$:H layer and a thin p-type a-SiC:H layer. However, the reduction of the p-type a-SiC:H results in a reduction of the V_{oc} (917 mV) as well as the *FF* (68.2%). The conversion efficiency of this configuration is 10%. Finally, by application of the p-type µc-SiO$_x$:H/ thin p-type µc-Si:H/ thin p-type a-SiC:H layer stack the short-circuit current density could be retained at 15.7 mA/cm² resulting in combination with a higher fill factor of 70.3% to the highest conversion efficiency of 10.3%.

Figure 6.1.3: Photovoltaic parameters of a-Si:H solar cells with different p-type layer configurations: with p-type µc-Si:H contact layer (reference); with p-type µc-SiO$_x$:H contact layer; with p-type µc-SiO$_x$:H contact layer and a thin p-type a-SiC:H layer; with p-type µc-SiO$_x$:H/thin p-type µc-Si:H/ thin p-type a-SiC:H layer stack. All solar cells are deposited on top of sputter-etched ZnO:Al front contact.

6.1.2   p-type µc-SiO$_x$:H as Window Layer in µc-Si:H Solar Cells

As for a-Si:H solar cells the same p-type µc-SiO$_x$:H material has been applied as a transparent p-type layer in µc-Si:H solar cells. The state-of-the-art µc-Si:H solar cell has a p-type µc-Si:H layer. Figure 6.1.4 shows a schematic drawing of a hydrogenated microcrystalline silicon (µc-Si:H) single-junction solar cell with a p-type µc-Si:H layer. By implementing a transparent µc-SiO$_x$:H p-type layer, the goal was to improve the current density. A p-type µc-SiO$_x$:H was deposited and the thickness of the p-type µc-Si:H layer was decreased. The photovoltaic parameters of µc-Si:H solar cells with different p-type layer configurations are shown in Figure 6.1.5. All solar cells have a thickness of 1150 nm and are deposited on textured ZnO:Al front contact. An efficiency improvement from 8.4% to 9.5% for µc-Si:H solar cells was achieved with a p-type µc-SiO$_x$:H window layer. The efficiency improvement is driven by the short-circuit current density as well as by the open circuit voltage. J_{sc} has been improved from 23.0 mA/cm² to 25.3 mA/cm² while the V_{oc} has been increased from 511 mV to 530 mV.
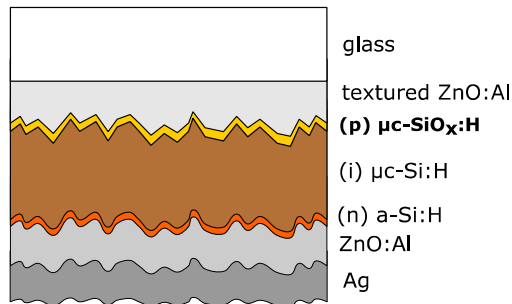
Figure 6.1.4: Sketch of a standard single junction µc-Si:H solar cell deposited with a p-type µc-SiO$_x$:H layer on ZnO:Al coated glass and ZnO:Al/Ag as back contact.

Approaches to improve the current density, by increasing the thickness of the solar cell to 1.5 µm, lead to no further improvement of the conversion efficiency. Even though an improvement of J_{sc} to 26.6 mA/cm² was achieved, the efficiency was limited by a reduction of V_{oc} and FF.
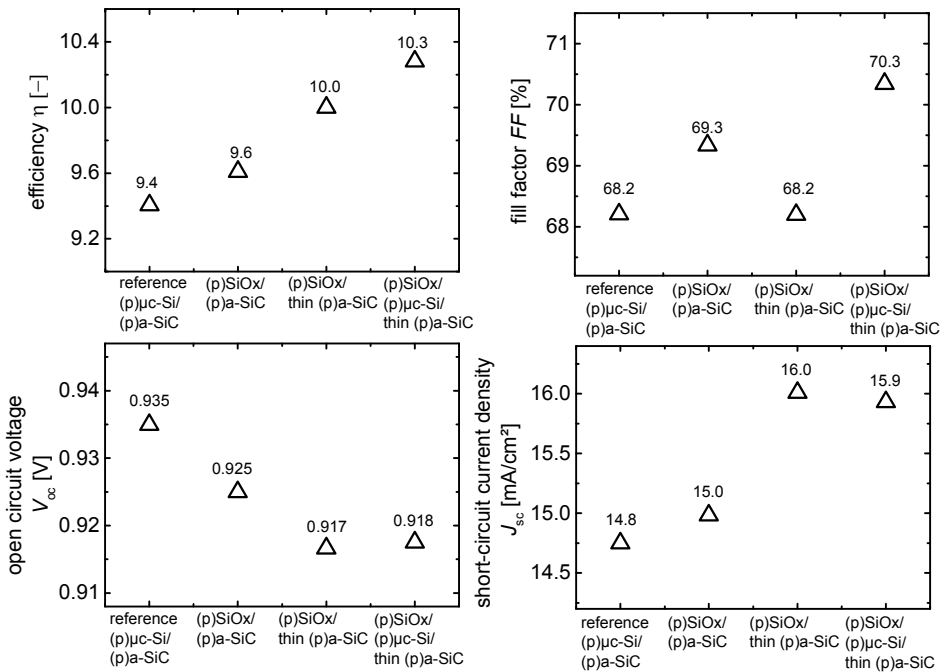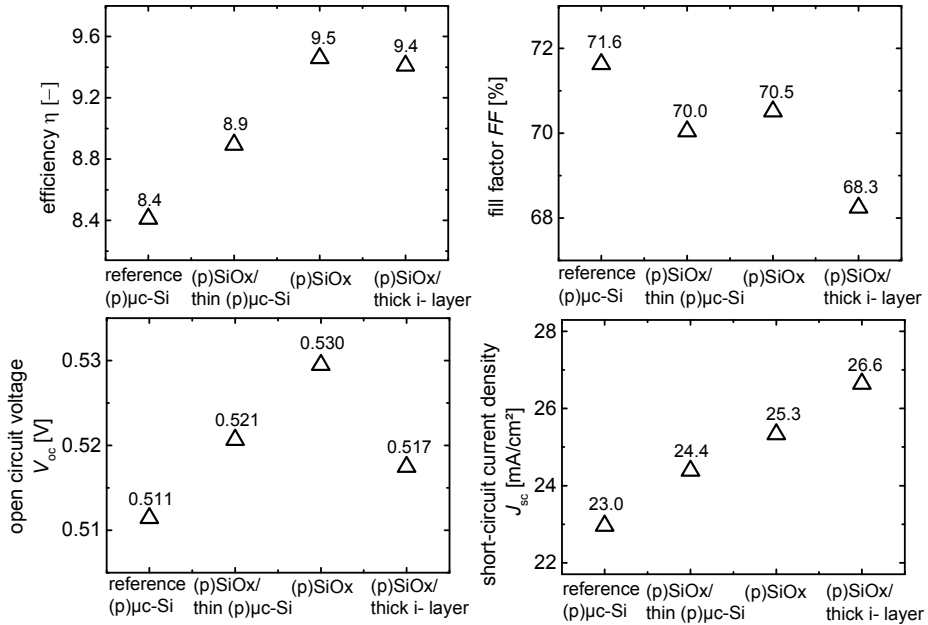
Figure 6.1.5: Photovoltaic parameters of µc-Si:H solar cells with different p-type µc-SiO$_x$:H configurations: with p-type µc-Si:H contact layer (reference); with p-type µc-SiO$_x$:H contact layer and thin p-type µc-Si:H layer; with only a p-type µc-SiO$_x$:H contact layer; with p-type µc-SiO$_x$:H and increased i-layer thickness. All solar cells are deposited on top of sputter-etched ZnO:Al front contact.

The *EQE* and the absorptance of µc-Si:H solar cells with p-type µc-SiO$_x$:H as a window layer compared to the reference with p-type µc-Si:H in shown in Figure 6.1.6. The short-current densities obtained by *EQE* measurement ($J_{sc, EQE}$) is also presented in the graphic. The *EQE* spectra show that especially for the short wavelength rage a distinct improvement is observed. The strong improvement of spectral response in a wavelength range between 350 nm and 600 nm is caused by a reduction of parasitic absorption in the p-type layer and also from the change of the growth behavior of the intrinsic material. For µc-Si:H solar cells with the combination of µc-SiO$_x$:H p-type layer and a thicker i-layer, a further improvement of the *EQE*, also for the long wavelength range, is seen. This is in agreement with the improvements seen for the absorptance.
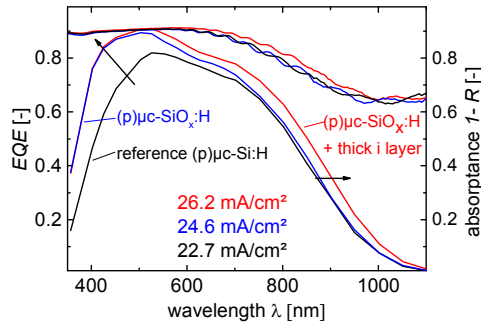
Figure 6.1.6: External quantum efficiency of µc-Si:H solar cells with p-type µc-SiO$_x$:H as a window layer. The current densities obtained by *EQE* measurement ($J_{sc,\,EQE}$) are shown. The reference is a µc-Si:H solar cell with p-type µc-Si:H.

As an attempt to improve the conversion efficiency of µc-Si:H solar cells further, the electrode gap was adjusted to 9 mm instead of 12.5 mm. For optimization reasons the PECVD process parameters regarding the SiH$_4$/H$_2$-ratio r_{SiH4} and the i-layer thickness were fabricated in two series. Results of the series obtained by a variation of the r_{SiH4} from 1.41% to 1.62% while holding the hydrogen flow constant are shown in Figure 6.1.7. All solar cells include a p-type µc-SiO$_x$:H and an n-type a-Si:H layer. The silane flow variations result in a steady improvement of the V_{oc} from 520 mV to 590 mV. At the same time a reduction of the current density is observed going from 25 mA/cm² to 23.3 mA/cm². For high r_{SiH4} both findings are linked to a shift of the silicon growth to higher amorphous fraction and therefore, to a higher band gap and weaker red response. The maximum of the fill factor is seen for a r_{SiH4} of 1.52 %, while higher values lead to a drop of the *FF*. Low silane flows resulted in a conversion efficiency of 9.2%, which is due to lower V_{oc} and *FF*. Highest efficiencies of over 10% are seen for r_{SiH4} of 1.46% to 1.52%.
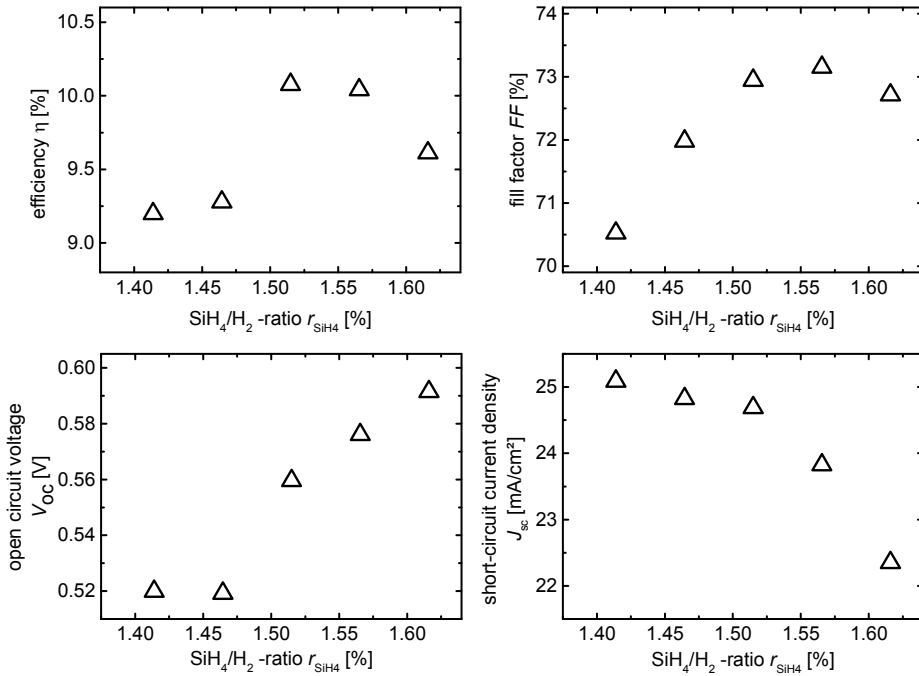
Figure 6.1.7: Photovoltaic parameters of μc-Si:H single junction solar cells deposited with an electrode gap of 9 mm. The series shows results obtain by a variation of the silane flow r_{SiH4} from 1.41% to 1.62%. All solar cells include a μc-SiO$_x$:H p-type layer. The solar cells have a thickness of 1.17 μm.

In Figure 6.1.8 the photovoltaic parameters of a series of μc-Si:H solar cells obtained by a variation of the i-layer thickness ranging from 630 nm to 1800 nm are presented. The silane flow r_{SiH4} was kept constant at 1.52%. The reference solar cell with a standard μc-Si:H p-type layer shows an V_{oc} of 0.53 V, while solar cells with a μc-SiO$_x$:H p-type layer and the same i-layer thickness (1.17 μm) show a V_{oc} of 0.56 V. In general, for solar cells deposited with the same p-type layer a steady decreasing trend for the V_{oc} is seen going from 0.59 mV for 630 nm to 0.54 V for 1.8 μm. More pronounced is the decrease of the fill factor going from 76% to 68% when increasing the thickness. However, the short-circuit current density increases with increasing i-layer thickness going from < 22 mA/cm² for 630 nm thick to 26 mA/cm² for 1.8 μm thick solar cells. This is linked to an improvement of the red response seen by *EQE* measurements (data not shown). The improvement of the J_{sc} of μc-Si:H solar cell with the same i-layer thickness but a more transparent μc-SiO$_x$:H p-type layer amounts to 2 mA/cm² which is caused by a better blue response. This effect is similar to findings shown in Figure 6.1.5. The improvement of V_{oc}

and J_{sc} in combination of a similar fill factor result in an efficiency improvement from 8.9% to 10.1%.
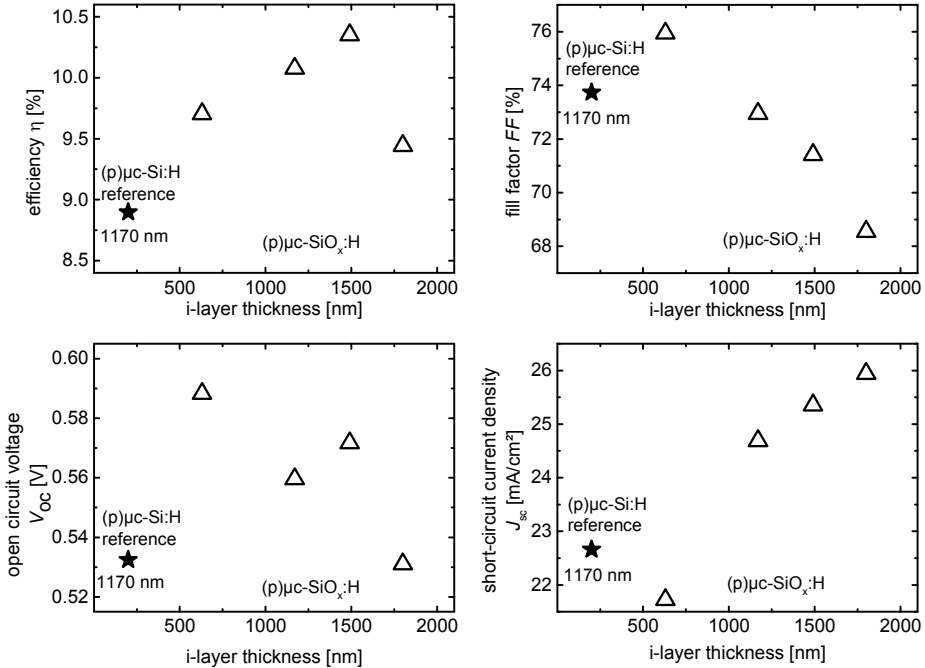
Figure 6.1.8: Photovoltaic parameters of µc-Si:H single junction solar cells deposited with an electrode gap of 9 mm. The series shows results obtain by a variation of the i-layer thickness varying from 630 nm to 1800 nm. r_{SiH4} was 1.52%. Results of a reference solar cell with a standard µc-Si:H p-type layer is shown.

The highest conversion efficiency was found for 1490 nm thick solar cells. That single junction solar cell with a µc-SiO$_x$:H p-type layer shows a short-circuit current density of 25.4 mA/cm², an open circuit voltage of 568 mV. In combination with a FF of 71.6% a conversion efficiency of 10.42% has been achieved.

Discussion

When replacing the p-type µc-Si:H contact layer by the more transparent p-type µc-SiO$_x$:H in a-Si:H and µc-Si:H solar cells a reduced parasitic absorption was observed by *EQE* measurements. A clear conversion efficiency improvement for both cases was achieved. In the case of a-Si:H solar cells it is seen that a contact layer made of p-type µc-SiO$_x$:H is capable of providing a low-ohmic contact to the ZnO:Al front contact. In this study the p-type a-SiC:H layer could not be fully substituted by the p-type µc-SiO$_x$:H layer in the case of a-Si:H solar cells. This finding was associated with a strong decrease of the V_{oc} meaning that a p-type a-SiC:H layer is essential to provide an adequate p/i-interface in a-Si:H solar cell. Nevertheless, by decreasing the layer thickness of the p-type a-SiC:H layer the parasitic absorptance could be decreased further resulting in higher short-circuit current densities. The impact of various interfaces on the electrical performance of solar cells will be discussed in Chapter 8.3.

Such efficiency improvements by implementation of a p-type layer made of µc-SiO$_x$:H were also reported by other groups [5][60][65]. Here, solar cells with a higher fill factor and enhanced blue response are presented. However, the clear reduction of solar cell reflection as shown in reference [60] was not measured in this work. The reason might because of the small p-type layer thickness of only 8 nm which makes it not suitable to function as a refractive index matching layer for a better light incoupling. In [60] the p-type µc-SiO$_x$:H layer was reported to be 20 nm thick.

In the case of µc-Si:H solar cells the short-circuit current density was increased from 23 mA/cm² to more than 25 mA/cm². Also, the V_{oc} was improved from 510 mV to 530 mV. It is seen that an additional layer for the improvement of the p/i-interface is not needed as in the case of a-Si:H solar cells. The electrical properties of µc-Si:H solar cells with a p-type µc-SiO$_x$:H layer are improved in terms of *FF* and V_{oc}.

The improvement of V_{oc} by 20 mV to 30 mV associated with the substitution of p-type µc-Si:H by p-type µc-SiO$_x$:H is linked to a decrease of the crystalline volume fraction of the intrinsic µc-Si:H material. The Raman intensity ratio from $I_c = 61.2\%$ for µc-Si:H i-layer grown on top of µc-Si:H p-type layer was decreased for layers grown on top of p-type µc-SiO$_x$:H ($I_c = 56.9\%$) under the same deposition conditions. This was measured by ex-situ Raman spectroscopy for λ = 658 nm.
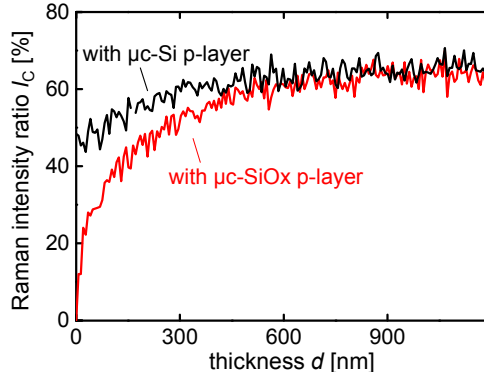
Figure 6.1.9: Raman intensity ratio I_c of µc-Si:H i-layers plotted as a function of film thickness. The i-layers have been deposited under the same conditions on top of the µc-Si:H and the µc-SiO$_x$:H p-type layer. The solar cells are deposited on single textured ZnO:Al front texture.

Furthermore, a newly implemented method of in-situ Raman measurement [67] was obtained to determine the evolution of crystalline growth. The results are shown in Figure 6.1.9. A distinct difference in the first 500 nm is seen. Here, it is to mention that the in-situ Raman measurements were obtained by a small chamber PECVD tool. The profiles show that the intrinsic material starts to grow with a crystallinity I_c of over 45% on top of p-type µc-Si:H, while the Raman profile for layers grown on top of a µc-SiO$_x$:H p-type layer starts at much lower values. The crystalline volume fraction increases rapidly with the progress of growth and the Raman profile aligns to the I_c values measured for an i-layer grown on p-type µc-Si:H. Above 600 nm layer thickness I_c amounts to ~ 60%. The Raman crystallinity profiles reveal different qualitative trends obtained for different p-type layer conditions. Another possibly explanation for the improvement of the V_{oc} is the formation of an advanced p/i-interface between µc-SiO$_x$:H p-type layer and the intrinsic µc-Si:H layer.

Also, the Neuchâtel group achieved remarkable improvements of the performance of µc-Si:H single junction solar cells through the implementation of p-type µc-SiO$_x$:H [60]. Due to enhanced blue response the short-circuit current density was increased from 23.6 mA/cm² to 25.1 mA/cm². In that publication it is shown that the V_{oc} was improved for solar cells deposited on ZnO:B texture, which likely induces formation of nanocracks. Therefore, the improvement of the V_{oc} is explained by the quenching of "nanoshunts" [60]. The measured Raman crystallinity did not show significant differences for µc-Si:H

i-layers grown on top of µc-Si:H or µc-SiO$_x$:H p-type layer layers. This is in agreement with ex-situ Raman measurements conducted as part of this thesis. Similar crystallinities are measured for µc-Si:H solar cells grown on different p-type layers. However, by usage of the in-situ Raman spectroscopy an evolution of the crystalline growth profile can be observed and significant differences are seen between both configurations for the first few hundred nanometers. The understanding of growth behavior as well as advanced process monitoring and control might lead to a next level of more efficient thin-film silicon solar cells.

6.2   μc-SiO$_x$:H Layers as Intermediate Reflectors in Tandem Solar Cells

In this chapter, tandem solar cells with intermediate reflector layer (IRL) made of doped μc-SiO$_x$:H are presented. The ~2.5 µm thick tandem solar cells were deposited on SnO$_2$:F coated glass. For the back contact, sputtered ZnO:Al/Ag back reflectors were applied. In tandem solar cells the a-Si:H top cells and μc-Si:H bottom cells are deposited in a superstrate configuration (p-i-n/p-i-n). The IRLs made of doped μc-SiO$_x$:H were prepared by RF-PECVD from gas mixtures of silane (SiH$_4$), carbon dioxide (CO$_2$), hydrogen (H$_2$), phosphine (PH$_3$) for n-type and trimethylborane (TMB) for p-type material. A schematic drawing of a tandem solar cell device with intermediate reflector layer is shown in Figure 6.2.1.
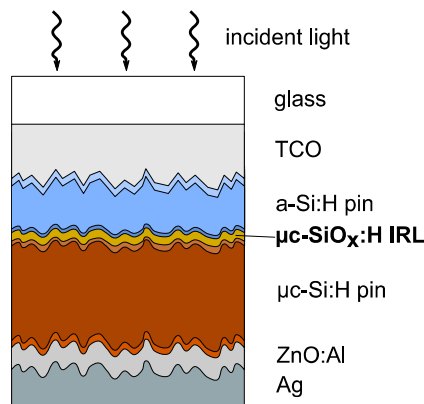
Figure 6.2.1: Schematic drawing of a tandem solar cell with intermediate reflector layer between the a-Si:H top and the μc-Si:H bottom cell.

Many aspects of the IRL are investigated as layer thickness, refractive index or the influence of the front texture. In this chapter, the effects seen for different IRL thicknesses, refractive indices and n- and p-doping are studied. Chapter 7 will concentrate on the topic of the interplay between various texture parameters and the solar cell performance with IRL.

6.2.1   Intermediate Reflectors made of n-type μc-SiO$_x$:H

Integrated as part of the tunnel recombination junction between the n-type layer of the top cell and the p-type layer of the bottom cell, the intermediate reflector layer requires a certain electrical conductivity. In Figure 6.2.2 the external quantum efficiencies and the absorptance of tandem solar cells without and with IRLs of different thicknesses are shown. An IRL material with a refractive index of 1.9, E_{04} of 2.6 eV and a dark conductivity of 2.5 x 10^{-4} S/cm has been applied between a 350 nm thick top and a 1.9 µm thick bottom cell. From the *EQE* measurements it is seen that the applied n-type μc-SiO$_x$:H layer functions as an intermediate reflector and with a thicker IRL more light is maintained within the top cell while the bottom cell current density is reduced. The *EQE* of the top cell is improved for the complete wavelength range. However, the improvements are more distinct for a wavelength range between 550 nm to 750 nm. At the same time the *EQE* of the bottom solar cell is reduced in a wavelength range from 550 nm to 830 nm. The short-circuit current density of the top and the bottom solar cell, derived from *EQE* measurements for different tandem solar cells are shown in Table 6.2.1. It is seen that when no IRL was applied the a-Si:H top cell limits the short-circuit current of the tandem device to 12.1 mA/cm^2. The bottom cell shows a $J_{EQE, bottom}$ of 13.1 mA/cm^2. The integration of a 40 nm thick IR layer between the sub-cells improves the top cell current density by 0.5 mA/cm² ($\Delta J_{EQE, top}$) while 0.9 mA/cm² is missing in the bottom solar cell ($\Delta J_{EQE, bottom}$) compared to the reference solar cell. The current has been transferred from the bottom to the top cell. The solar cell is now limited by the bottom cell with a $J_{EQE, bottom}$ of 11.7 mA/cm². A further increase of the IRL thickness to 80 nm results in a $\Delta J_{EQE, top}$ of 1.1 mA/cm². At the same time $\Delta J_{EQE, bottom}$ amounts to 2.3 mA/cm². The *EQE* and also the absorptance curves indicate a reflection loss at ~800 nm when an IRL was integrated. The loss mechanism and the thickness dependency will be discussed in Chapter 7 in detail.
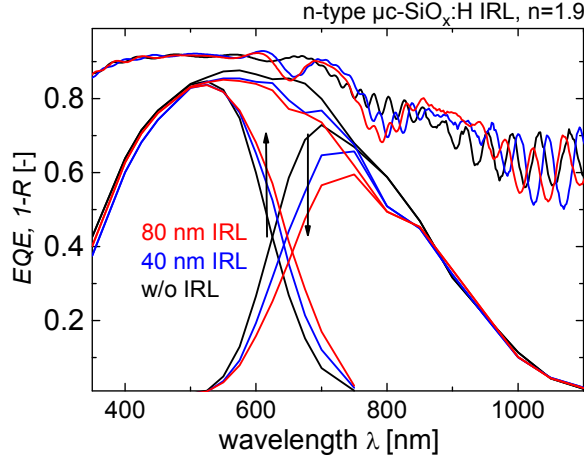
Figure 6.2.2: External quantum efficiency, *EQE* and absorptance *1-R* of tandem solar cells without and with µc-SiOx:H IRL layer with different thicknesses. The IRL has a refractive index *n* of 1.9. The tandem solar cells consist of top/bottom cell thickness of 0.35/1.9 µm.

Table 6.2.1: Photovoltaic parameters efficiency η; fill factor *FF*; open circuit voltage V_{oc}; short-circuit current density J_{sc} and the current density $J_{EQE, top}$ of the top and the bottom solar cell, derived from *EQE* measurements for tandem solar cells shown in Figure 6.2.2 with IRL with different thicknesses.

IR layer thickness [nm]	η [%]	*FF* [%]	V_{oc} [V]	J_{sc} [mA/cm²]	$J_{EQE, top}$ [mA/cm²]	$J_{EQE, bottom}$ [mA/cm²]
0	12.4	74.6	1.37	12.2	12.1	13.1
40	11.7	74.6	1.35	11.7	12.6	11.7
80	10.9	75.0	1.35	10.8	13.2	10.8

As summarized in Table 6.2.1, for tandem solar cells without an IRL a conversion efficiency of 12.4% and a *FF* of 74.6% were achieved. The integration of a 40 nm thick IRL between the sub-cells comes with a reduction of η to 11.7%. While maintaining a high *FF*, the solar cell is now limited by the bottom cell. An increased IRL thickness to 80 nm is linked to an additional reduction of the efficiency to 10.9%. This also, was caused by a current limiting bottom cell with $J_{EQE, bottom}$ of 10.8 mA/cm^2. The V_{oc} was decreased when an IRL was integrated by 20 mV.

Another approach to adjust the amount of transferred current is to vary the refractive index *n* of the IRL. The higher the difference of the refractive index of the IRL and of the

surrounding silicon material the larger is the reflectance. Therefore, IRLs with the same thickness but various refractive indices (n_{IRL} = 1.9; 2.5; 3.1) were applied in tandem solar cells consisting of a top cell thickness of 350 nm and bottom cell thickness of 2.2 µm. The *EQE* spectra are shown in Figure 6.2.3. The current densities $J_{EQE, top}$ and $J_{EQE, bottom}$, derived from *EQE* measurements for different tandem solar cells are shown in Table 6.2.2. Figure 6.2.3. It is seen that a similar effect is obtained when the refractive index of the IRL is decreased as when the layer thickness is increased. With a lower refractive index more light is kept in the top cell. The top cell *EQE* increases especially in a wavelength range between 500 nm to 750 nm. Also in this wavelength range a clear decrease of the bottom cell *EQE* is observed. For the case with an IRL with n_{IRL} = 3.1 the top cell gains only 0.4 mA/cm² compared to the reference. By decreasing n_{IRL} to 2.5 $\Delta J_{EQE, top}$ could be increased by 0.7 mA/cm². Likewise, by decreasing n_{IRL} to 1.9 the $\Delta J_{EQE, top}$ was further improved amounting to 1.2 mA/cm². The current density losses in the bottom cells with n_{IRL} = 3.1; 2.5; 1.9 amount to 0.4 mA/cm²; 1.2 mA/cm² and 1.6 mA/cm², respectively. It is also seen that as the refractive indices are lowered the absorptance decreases indicating a stronger cell reflection.
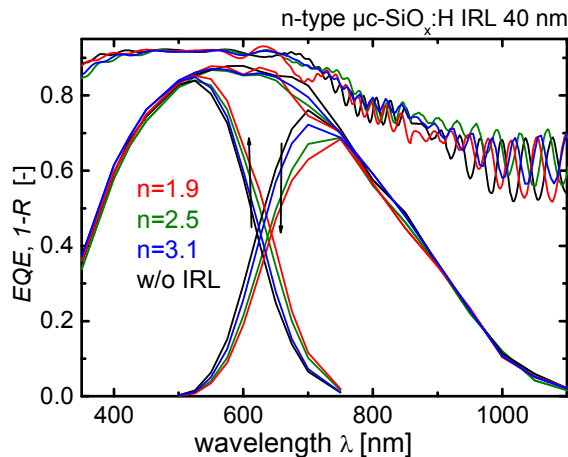
Figure 6.2.3: External quantum efficiency, *EQE* for tandem solar cells with 40 nm thick µc-SiO$_x$:H intermediate reflector with different refractive indices from n=1.9 (red) to n=3.1 (blue). The thickness of the bottom cell is 2.2 µm and the top cell remains is 0.35 µm thick.

Table 6.2.2: Photovoltaic parameters and the short-circuit current density of the top and the bottom solar cell, derived from *EQE* measurements for tandem solar cells with 40 nm thick µc-SiO$_x$:H intermediate reflector with different refractive index as shown in Figure 6.2.3.

n_{IRL}	η	*FF*	V_{oc}	J_{sc}	$J_{EQE, top}$	$J_{EQE, bottom}$
[-]	[%]	[%]	[V]	[mA/cm²]	[mA/cm²]	[mA/cm²]
1.9	12.1	73.0	1.36	12.1	12.9	12.1
2.5	12.3	73.1	1.36	12.4	12.4	12.5
3.1	12.0	72.9	1.35	12.2	12.1	13.3
-	12.0	74.7	1.35	11.9	11.7	13.7

The sub-cell current densities for tandem cells with various intermediate reflectors was derived from *EQE* measurements and the photovoltaic parameters are summarized in Table 6.2.2. The solar cell without an IRL shows a conversion efficiency of 12%. It is limited by the top cell and therefore. The solar cell shows a high fill factor, *FF* = 74.7%. With an IRL with n_{IRL} = 3.1 the top cell current density is improved. But sill, the solar cell remains top cell limited. The *FF* is reduced to 72.9% resulting in a consistent η = 12%. For the tandem solar cell with IRL (n_{IRL} = 2.5) the sub-cell current densities were matched at 12.4 mA/cm². With a fill factor of 73.1% the conversion efficiency was improved to 12.3%. A further decrease of the n_{IRL} to 1.9 resulted in a shift to a bottom limited case. The conversion efficiency amounts to 12.1% while the *FF* remains at 73%. From the *JV*-measurements is seen that the tandem solar cells with an IRL with n_{IRL} = 1.9 and 2.5 show a slight improvement of the V_{oc} to 1.36 V compared to the IRL with n_{IRL} = 3.1 and the case without an IRL showing V_{oc} = 1.35 V.

6.2.2 Intermediate Reflectors made of p-type µc-SiO$_x$:H

As an alternative to n-type µc-SiO$_x$:H layers p-type µc-SiO$_x$:H were applied as an intermediate reflector layer IRL in tandem solar cells. The a-Si:H top cell has a thickness of 350 nm and µc-Si:H bottom cell a thickness of 2.1 µm. The *EQE* data and the absorptance of a-Si:H/µc-Si:H tandem cells with p-type µc-SiO$_x$:H IRL of different thicknesses is shown in Figure 6.2.4. The reference is a tandem solar cell without an intermediate reflector layer. By implementing a p-type IRL the *EQE* of the top cell in a

wavelength range from 500 nm to 750 nm is enhanced. This is visible for an IRL thickness of 24 nm. This effect is more distinct for an IRL thickness of 40 nm. The tandem solar cells with a 9 nm thick IRL shows no difference in the *EQE* compared to the reference and is therefore not presented in the graphic. The *EQE* of the bottom solar cells are decreased when an IRL was implemented. The effect is clearly seen in a wavelength range between 550 nm and 800 nm.
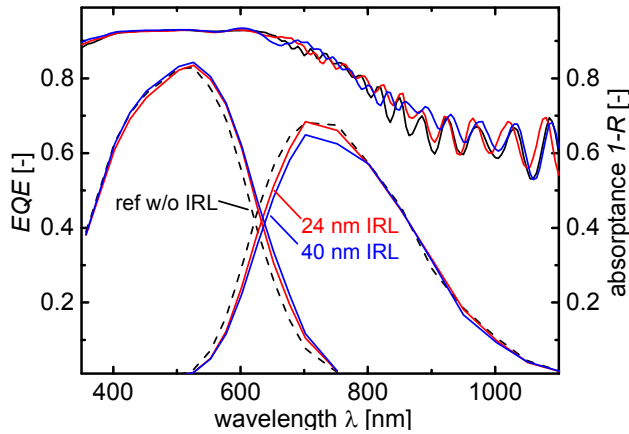
Figure 6.2.4: External quantum efficiency *EQE* of a-Si:H/µc-Si:H tandem cells with p-type µc-SiO$_x$:H as IRL applied with different thickness. The reference is a tandem solar cell without an intermediate reflector layer. Green lines indicate the *EQE* of a tandem cell with p-type µc-SiO$_x$:H as an IRL and n-type µc-SiO$_x$:H as a back reflector.

Table 6.2.3: Photovoltaic parameters of a-Si:H/µc-Si:H tandem cells with p-type µc-SiO$_x$:H of different thickness deposited on SnO$_2$:F coated glass substrates (*EQE* shown in Figure 6.2.4). The reference is a tandem solar cell without an intermediate reflector layer.

p-type IRL thickness	η	*FF*	V_{OC}	J_{SC}	$J_{EQE, top}$	$J_{EQE, bottom}$
[nm]	[%]	[%]	[V]	[mA/cm²]	[mA/cm²]	[mA/cm²]
reference w/o IRL	12.0	74.5	1.36	11.8	11.7	13.2
9	12.0	74.0	1.36	11.9	11.6	13.1
24	12.3	73.5	1.36	12.3	12.1	12.6
40	12.1	74.7	1.35	12.0	12.5	12.0

In Table 6.2.3 the photovoltaic parameters of a-Si:H/µc-Si:H tandem cells with different IR layers deposited on SnO$_2$:F front contact are presented. Clear differences are

seen for the short-circuit current density for the top and bottom cells ($J_{EQE,\ top}$ and $J_{EQE,\ bottom}$). A tandem solar cell with a thin p-type μc-SiO$_x$:H of 9 nm shows no clear difference compared to the reference, while a 24 nm thick layer improved $J_{EQE,\ top}$ by 0.4 mA/cm². At the same time $J_{EQE,\ bottom}$ is reduced by 0.5 mA/cm². A further increase of the IRL thickness to 40 nm leads to an improved $J_{EQE,\ top}$ by 0.8 mA/cm² and a decrease of $J_{EQE,\ bottom}$ of 1.2 mA/cm² compared to the reference. In this case the tandem cell becomes limited by the bottom cell current density. It is seen that the fill factor stays consistent for most samples in the range of 74% and the V_{oc} at 1.36 V. Only in the case with a 40 nm thick IRL the V_{oc} is reduced to 1.35 V. In this series the reference solar cell show a conversion efficiency of 12%. This is improved by the implementation of a 24 nm thick IRL to 12.3%. When the IRL thickness is enlarged to 40 nm the solar cell becomes bottom limited with $J_{EQE,\ bottom} = 12.0$ mA/cm² leading to a conversion efficiency to 12.1%.

Discussion

In this chapter intermediate reflector layers made of n-type and p-type μc-SiO$_x$:H were integrated in a-Si:H/μc-Si:H tandem solar cells. IRLs with various refractive indices and different layer thicknesses were investigated. It was shown that the variation of the μc-SiO$_x$:H IRL thickness and the refractive index influences the amount of light reflected back into the top cell. This is in agreement with the literature [6]. Due to current matching, a conversion efficiency improvement from 12.0% to 12.3% was achieved by the implementation of an IRL with n_{IRL} = 2.5 when using SnO$_2$:F coated glass substrates. Also, with an IRL made of p-type μc-SiO$_x$:H the conversion efficiency could be improved from 12.0% to 12.3%. An IRL with n_{IRL} = 3.1 resulted in a rather low top cell current density gain ($\Delta J_{EQE, top}$) of only 0.4 mA/cm². By decreasing n_{IRL} to 2.5 $\Delta J_{EQE, top}$ could be increased by 0.7 mA/cm². Finally, when n_{IRL} was decreased to 1.9 the $\Delta J_{EQE, top}$ was further improved amounting to 1.2 mA/cm². Similar trends are reported in literature concerning variations of the refractive index [75]. Where IRLs with n_{IRL} from 2.05 to 1.75 were fabricated and implemented in a tandem solar cell.

The reflectance of an IRL is a matter of thickness and refractive index. In Chapter 5 it is shown that with the admixture of CO$_2$ and reduction of n the conductivity is also reduced. In order to obtain a high fill factor the applied material is required to have a high electrical conductivity. Therefore, a trade-off between electrical and optical properties becomes apparent.

It can be concluded that with lower refractive indices and thicker IRL more light is reflected back into the top cell resulting in larger short-circuit current densities in the top cell. At the same time a larger amount of light is kept away from the bottom cell resulting a strong decrease of the bottom cell short-circuit current density. The optical losses and the impact of the solar cell topography on those will be discussed in detail in Chapter 7.

6.3   n-type µc-SiO$_x$:H Layers as Back Reflectors
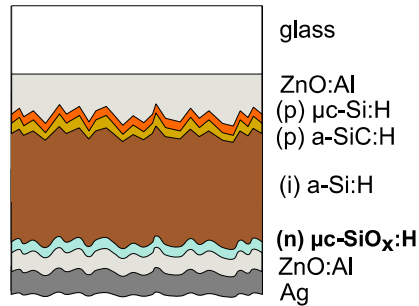
Figure 6.3.1: Schematic drawing of a standard single junction a-Si:H solar cell deposited with a n-type µc-SiO$_x$:H layer as part of a ZnO:Al/Ag back contact.

As presented before in Chapter 6.1 the current density of single junction solar cells are improved by the application of p-type µc-SiO$_x$:H as a window layer. Another approach to improve the current density is the integration of a second (n-type) µc-SiO$_x$:H layer at the back side of the solar cell, see sketch (Figure 6.3.1).

µc-Si:H solar cell with	$J_{sc,\,EQE}$ [mA/cm²]
reference (p)µc-Si:H	22.7
(p)µc-SiO$_x$:H	24.6
(p)µc-SiO$_x$:H + (n)µc-SiO$_x$:H (back)	25.2
(p)µc-SiO$_x$:H + thick i-layer	26.2
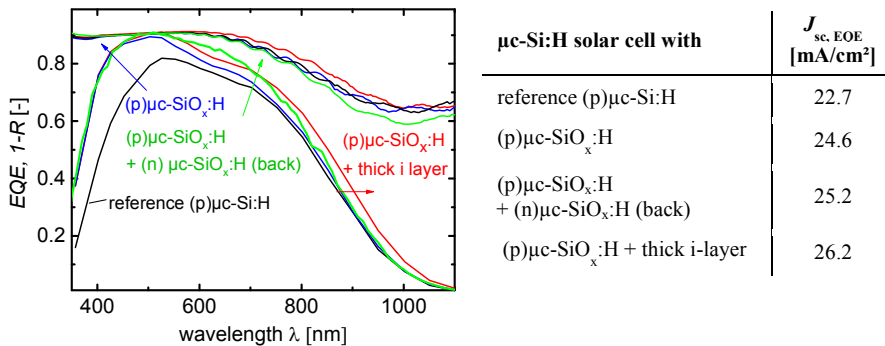
Figure 6.3.2: External quantum efficiency and absorptance of µc-Si:H solar cells with various window and back reflector layers. The *EQE* of a solar cell with a p-type µc-SiO$_x$:H window layer and an n-type µc-SiO$_x$:H layer as back reflector is displayed in green. The reference is a µc-Si:H solar cell with p-type µc-Si:H. The short-current density obtained by *EQE* measurements $J_{sc,\,EQE}$ of each configuration is shown in the table.

As shown in Figure 6.3.2, this additional n-type µc-SiO$_x$:H layer improves the spectral response of a µc-Si:H solar cell in the range between 500 nm and 900 nm. For higher

wavelength an enhanced cell reflectance is observed indicating an improved reflection at the back reflector. Compared to a solar cell without a µc-SiO$_x$:H back reflector the current density was improved by 0.7 mA/cm². In the following, the development of n-type µc-SiO$_x$:H used for back reflector application in thin-film silicon single junction and tandem solar cells will be presented. Solar cell results of a-Si:H single junction and a-Si:H/µc-Si:H tandem solar cells are shown. More details can be found in reference [69].

The solar cells were deposited on APCVD SnO$_2$:F coated glass from the *Asahi Glass Company.* The absorber layer of the single junction a-Si:H solar cells have a thickness of 315 nm. The tandem cells consist of a 315 nm top and 1.78 µm thick bottom cell. Between the two sub-cells a 40 nm thick IRL with a refractive index of 2.5 was deposited. An optimal back reflector material has a high electrical conductivity, a low refractive index, a high transparency and provides a low contact resistance to the back contact. Meeting those requirements, the applied n-type µc-SiO$_x$:H layer shows a refractive index of 2.2, an energy gap of 2.4 eV and a conductivity of 2×10^{-2} S/cm. The thickness was 45 nm. After the n-type layer a silver back reflector with a thickness of 700 nm was deposited. It is known that the introduction of a doped ZnO layer between the n-type layer and the metal back contact enhances the spectral response of a solar cell in long wavelength ranges [70]. However, because of an additional ZnO deposition step alternative ways are of interest. Therefore, n-type µc-SiO$_x$:H/Ag back reflector stacks are applied and investigated in terms of optical and electrical performances.

a-Si:H solar cell with	$J_{sc, EOE}$ [mA/cm²]
Ref. (n)a-Si/ZnO/Ag	14.7
(n)a-Si/Ag	14.0
(n)µc-Si/Ag	13.8
(n)µc-SiO$_x$:H/Ag	15.8

Figure 6.3.3: External quantum efficiency and absorptance of a-Si:H solar cells with different back reflector configuration. The reference is a state-of-the-art (n)a-Si/ZnO/Ag stack**.**

Figure 6.3.4: Solar cell parameters of a-Si:H cell with various n-type layers. As back reflectors Ag (black) is compared to a ZnO/Ag stack (red).

Figure 6.3.3 shows the *EQE* and absorptance of a-Si:H solar cells with a-Si:H, µc-Si:H and µc-SiOₓ:H as n-type layers. Also, the state-of-the-art back reflector layer stack consisting of n-type a-Si:H/ZnO/Ag is shown as a reference. It is apparent that for all configurations there are almost no differences regarding the *EQE* up to a wavelength of 550 nm. Above 550 nm the influence of the back reflector becomes visible. With a short-circuit current density of 13.8 mA/cm² the solar cell with a µc-Si:H n-type layer shows the lowest *EQE* followed by the configuration with an a-Si:H n-type layer. For the state-of-the-art back reflector with an additional 80 nm thick ZnO layer in front of the Ag layer the *EQE* is increased for the wavelength range from 550 nm to 750 nm. The current density was improved by 0.7 mA/cm² compared to the solar cell without the ZnO. The enhanced back reflection is even more pronounced for the n-type µc-SiOₓ:H/Ag back reflector and resulted in a short-circuit current density of 15.8 mA/cm². The improved reflectance is also seen in the absorptance measurements (*1-R*). The increased cell reflectance for wavelength above 750 nm indicate an improved reflectance at the back reflector for ZnO/Ag and especially for the n-type µc-SiOₓ:H/Ag stack.

Figure 6.3.4 shows the solar cell parameters of a-Si:H solar cells with various n-type layers. Ag back reflectors are indicated in black while the ZnO/Ag back reflector stack is

shown in red. The application of the n-type μc-SiO$_x$:H layer showed a remarkable increase of the short-circuit current density. However, the fill factor was low (60%) and therefore, the conversion efficiency was only 8.3%. By adding a ZnO interlayer between the n-type μc-SiO$_x$:H layer and Ag a *FF* of >70% was achieved. Comparing to n-type a-Si:H and n-type μc-Si:H the V_{oc} seen with the n-type μc-SiO$_x$:H layer was larger for both cases, Ag and the ZnO/Ag back reflectors. In comparison with the reference with an n-type a-Si:H/ZnO/Ag back reflector a conversion efficiency improvement from 9.4% to 9.9% was achieved with a (n)μc-SiO$_x$:H /ZnO/Ag stack.

The influence of different back reflector configurations was also investigated for tandem solar cells. In this series the influence of the ZnO layer on the performance of the quantum efficiency and solar cell performance for various n-type layers are investigated. Figure 6.3.5 shows the *EQE* of the tandem solar cell with emphasis on the bottom cell. The most pronounced effects are seen for wavelength above 650 nm in the bottom cells. The lowest spectral response is seen for a-Si:H as an n-type layer resulting in a bottom cell $J_{EQE,\,bottom}$ of 7.5 mA/cm². A higher *EQE* is seen for solar cells with a μc-Si:H n-type layer with $J_{EQE,\,bottom}$ = 8.2 mA/cm². By introducing the ZnO interlayer in front of the silver (state-of-the-art back reflector), a large improvement of the bottom cell *EQE* is observed resulting in a $J_{EQE,\,bottom}$ = 10.6 mA/cm². The highest spectral response is seen for solar cells with an n-type μc-SiO$_x$:H layer. Even without a ZnO layer $J_{EQE,\,bottom}$ was improved to 10.8 mA/cm². It is to mention that for solar cells with an n-type μc-SiO$_x$:H layer no further improvement was observed for an additional ZnO layer in front of the silver back reflector [69]. Like in the case of the single junction a-Si:H cell, an increased cell reflectance especially for longer wavelength is observed.
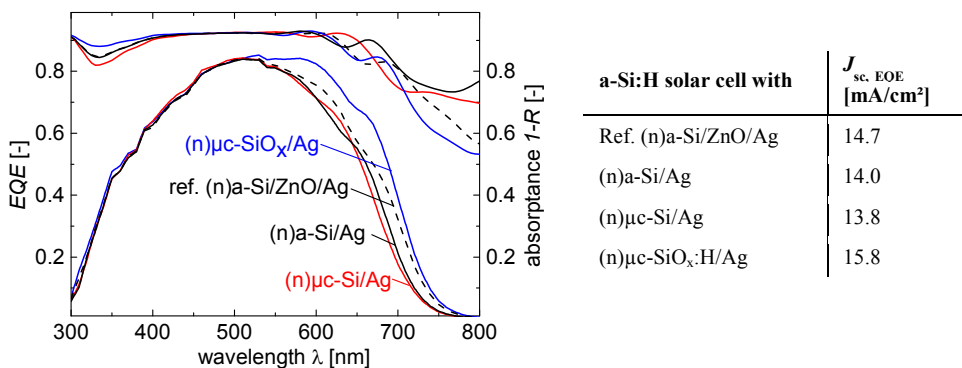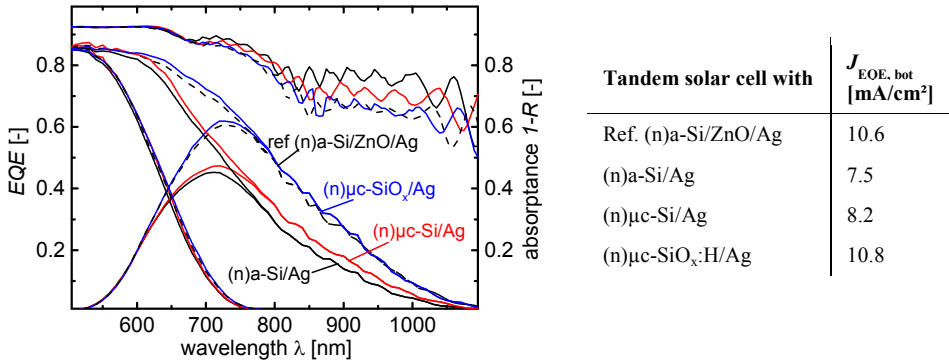
Figure 6.3.5: External quantum efficiency and absorptance of a-Si:H/μc-Si:H tandem solar cells with different back reflector configuration. The reference is a state-of-the-art n-type a-Si/ZnO/Ag stack. $J_{EQE,\ bot}$ was derived from *EQE* measurements of the bottom solar cells.
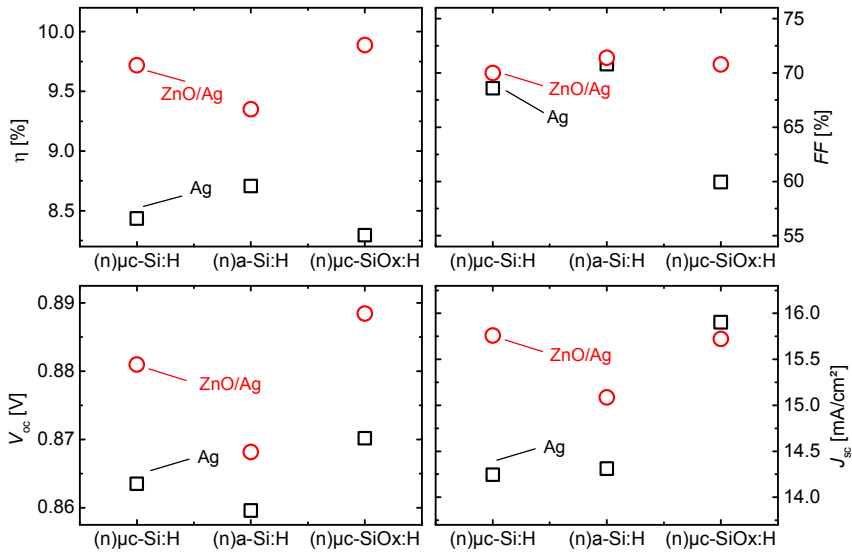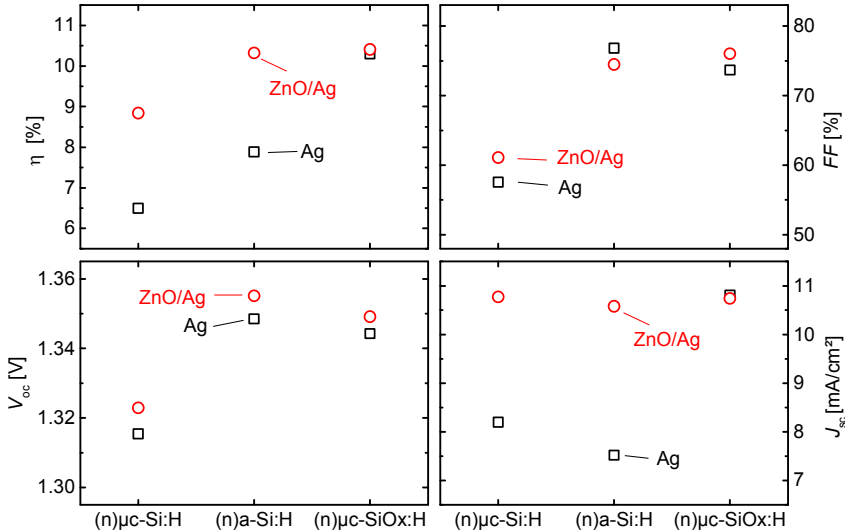

Figure 6.3.6: Solar cell parameters of tandem cell with various n-type layers. As back reflectors Ag (black) is compared to a ZnO/Ag stack (red).

In Figure 6.3.6 the photovoltaic parameters of tandem cells with different n-type layers and Ag or ZnO/Ag back reflectors are shown. Without an additional ZnO the conversion efficiency of solar cells with an n-type μc-Si:H (6.5%) and an a-Si:H (7.9%) layer are exceeded by the solar cells with a μc-SiOₓ:H n-type layer by far (10.3%). However, with a ZnO/Ag back reflector the efficiencies of the n-type μc-Si:H/ZnO/Ag and the n-type a-Si:H/ZnO/Ag are increased to 8.8% and 10.3%, respectively. The highest conversion

efficiency (η = 10.4%) was obtained with a n-type μc-SiO$_x$:H/ZnO/Ag back reflector. The short-circuit current density J_{sc} of the tandem cell is bottom limited in all cases. It was improved by the introduction of a ZnO interlayer between the n-type layer and the silver back reflector. The J_{sc} for tandem solar cells with an n-type µc-Si:H layer was improved from 8.2 mA/cm² to 10.8 mA/cm². For solar cells with an n-type a-Si:H layer the J_{sc} was improved from 7.5 mA/cm² to 10.6 mA/cm². However, the efficiency for tandem solar cells with an n-type µc-Si:H layer is still lower (η = 8.8%) and is linked to the smaller open circuit voltage of 1.32 V and the smaller fill factor of 61%. Those amount for n-type a-Si:H and µc-SiO$_x$:H layers to ~1.35 V and ~75%, respectively. To sum up, the additional ZnO layer between the n-type layer and the silver back reflector leads to remarkable improvements of the J_{sc} when using μc-Si:H and a-Si:H n-type layers resulting in an increase of the conversion efficiencies. In the case of n-type μc-SiO$_x$:H however, the J_{sc} was not improved. The solar cell's conversion efficiency remains in the same level showing that n-type μc-SiO$_x$:H/Ag could be an appropriate substitution for the n-type a-Si:H/ZnO/Ag state-of-the-art back reflector layer stack.

Discussion

The improvements of the *EQE* for the μc-SiO$_x$:H/Ag back reflector are caused by an enhanced red response which is attributed to an advanced reflectance at the back side. As in the case of a ZnO/Ag back reflectors the improvements can be explained by a reduction of plasmonic losses at the metal surface [70][71]. Plasmons excited at the metal surfaces can cause a reduction of the reflectance by plasmonic resonances. It is known that a reduction of plasmonic losses occurs with the presence of a transparent oxide. As reported, an additional metal oxide interlayer result in a blue shift of the plasmonic resonances [70][5]. The conversion efficiency and short-circuit current density improvements of solar cells with an n-type μc-SiO$_x$:H/Ag or a ZnO/Ag back reflector are a result of improved reflectance at the back side. The blue shift of the plasmonic absorption results in an enhanced reflection of longer wavelengths. For the case of μc-SiO$_x$:H as an n-type layer no further improvement of the bottom current density was achieved by the introduction of an additional ZnO layer. This suggests that also μc-SiO$_x$:H affects the plasmonic resonances in a way resulting in an enhanced reflectance for long wavelengths. Likewise, similar improvements of the measured solar cell reflectance is seen for ZnO/Ag and n-type μc-SiO$_x$:H/Ag back reflectors.

Tandem solar cells with an n-type μc-SiO$_x$:H/Ag back reflector show the same conversion efficiency as the state-of-the-art n-type a-Si:H/ZnO/Ag back reflector. The short-circuit current densities of single junction a-Si:H as well as tandem solar cells with an n-type μc-SiO$_x$:H/Ag back reflector stack exceeded the current density of solar cells with the state-of-the-art back reflector. In literature it has been reported that the back reflector stack consisting of μc-SiO$_x$:H/ZnO/Ag result in highest current densities [76]. However, it is shown in this chapter that a back reflector consisting of only μc-SiO$_x$:H/Ag led to equally high performances as the state-of-the-art ZnO/Ag back reflector. It is known that the plasmonic resonances shift further to the short wavelengths when the refractive index of the applied embedding medium is lower. The reason for these different results might be that the refractive index of applied μc-SiO$_x$:H in this work was lower than in the literature.

The optical effects seen for single junction solar cells are larger than in tandem solar cells. For a-Si:H solar cells the J_{sc} was improved by ~1mA/cm² by using a μc-SiO$_x$:H/Ag back reflector compared to the standard a-Si:H/ZnO/Ag back reflector. In tandem solar

cells the effect was only ~0.1 mA/cm². The reason for this is because of the impact of the back reflection for a tandem solar cell is generally rather low. Due to the thicker absorption layers the portion of light that reaches the back reflector already is lower as compared to thinner single junction solar cells. Therefore, an improved reflectance shows only a minor effect on the *EQE*. This also explains why the measured enhanced cell reflectance for long wavelengths is more distinct for a-Si:H than for tandem solar cells when using a μc-SiO$_x$:H/Ag back reflector. Also, for longer wavelengths the absorption coefficient of the a-Si:H material is very low allowing a larger fraction of light to escaping the solar cell device after being reflected at the back reflector.

It has been presented that a-Si:H solar cells with a μc-SiO$_x$:H/Ag back reflector show excellent optical performances while the fill factor and V_{oc} are clearly reduced. This effect is not seen for tandem solar cells. This indicates that the losses occur for the a-Si:H i-layer/(n)μc-SiO$_x$:H/Ag layer stack. When ZnO is introduced between the n-type μc-SiO$_x$:H and the Ag layer *FF* and V_{oc} are improved. Also, for tandem solar cells where μc-Si:H i-layer/ (n)μc-SiO$_x$:H/Ag represent the back contact *FF* and V_{oc} are in a similarly high level as when ZnO is applied. The reason for these differences can be due to different work functions of the a-Si:H and µc-Si:H intrinsic layers.

6.4   Conclusion

In Chapter 6.1 the newly developed p-type hydrogenated microcrystalline silicon oxide (μc-SiO$_x$:H) was implemented as a contact or window layer in amorphous silicon (a-Si:H) and microcrystalline (μc-Si:H) single junction solar cells. A reduced parasitic absorption was obtained by the replacement of the p-type μc-Si:H contact layer by the more transparent p-type μc-SiO$_x$:H. A conversion efficiency improvement of a-Si:H solar cells from 9.4% to 9.6% was achieved by applying a p-type μc-SiO$_x$:H contact layer compared to the standard p-type μc-Si:H layer. In combination with a thin p-type a-SiC:H a conversion efficiency improvement to 10.3% was achieved.

In the case of μc-Si:H solar cells the replacement of the p-type μc-Si:H layer by a p-type μc-SiO$_x$:H layer led to a strong improvement of the short-circuit current density from 23 mA/cm² to more than 25 mA/cm². Also, the V_{oc} was improved from 510 mV to 530 mV. The increase of the voltage is linked to a decrease of the crystallinity of the first few hundred nanometers of the intrinsic material which was also shown by a newly developed in-situ Raman measurement. These changes resulted in an improvement of the conversion efficiency of μc-Si:H solar cells from 8.4% to 9.5%. Under the changed growth conditions for the intrinsic μc-Si:H layer grown on a p-type μc-SiO$_x$:H layer, an optimization concerning the SiH$_4$/H$_2$-ratio and i-layer thickness were conducted. Those optimizations resulted in a further conversion efficiency improvement. A record μc-Si:H solar cell with η = 10.42%, J_{sc} = 25.35 mA/cm², V_{oc} = 568 mV and FF = 71.6% was demonstrated.

The conversion efficiency improvement is a result of an improved light incoupling in combination with a low ohmic TCO/p contact and a good p/i-interface. Also changed crystalline growth behavior affects the material properties of the intrinsic layer leading to high fill factor and high V_{oc}.

In Chapter 6.2 intermediate reflector layers made of n-type and p-type μc-SiO$_x$:H were successfully integrated in an a-Si:H/μc-Si:H tandem solar cell. IRLs made of n-type material with various refractive indices and different layer thicknesses were investigated. It was shown that the variation of the μc-SiO$_x$:H IRL thickness and the refractive index influences the amount of light reflected back into the top cell. Due to current matching, a conversion efficiency improvement was achieved by implementing an IRL. Also, with tandem solar cells with an IRL made of p-type μc-SiO$_x$:H the conversion efficiency could

be improved. It can be concluded that with a thicker IRL or a lower refractive index more light is reflected back in to the top cell.

In Chapter 6.3 it was shown that the use of a μc-SiO$_x$:H/Ag reflector resulted in an enhanced J_{sc} of single junction and tandem solar cells in comparison with a-Si:H/Ag or μc-Si:H/Ag back reflectors. The improvements are caused by an enhanced red response which is attributed to an advanced reflectance. The presence of an n-type μc-SiO$_x$:H layer suppresses the plasmonic losses at the back reflector and also reduces absorption losses as compared to the state of the art a-Si:H n-type layer. The effects are more distinct for single-junction solar cells compared to tandem cells. The J_{sc} was improved by ~1 mA/cm² for a-Si:H and only ~0.1 mA/cm² for tandem solar cells compared to the standard a-Si:H/ZnO/Ag back reflector.

To conclude, an alternative to the ZnO/Ag back reflector was successfully applied in single junction and tandem solar cells. A newly implemented n-type μc-SiO$_x$:H layer provides excellent optical and electrical performances. The use of a μc-SiO$_x$:H/Ag layer stack renders possible the reduction of the state-of-the-art ZnO deposition step in the manufacturing process.

In this chapter it was shown that doped hydrogenated microcrystalline silicon oxide layers can be implemented with various functions in thin-film silicon solar cells. Like reported by several other groups [60][5][75][76] conversion efficiencies improvements of thin-film silicon solar cells by implementing doped μc-SiO$_x$:H were obtained. Furthermore, in other photovoltaic technologies like in silicon heterojunction solar cells μc-SiO$_x$:H is also of high interest [77]. Therefore, it can be expected that future thin-film silicon solar cells with higher efficiencies will be established by application of doped microcrystalline silicon oxide.

Chapter 7
Light Management in Thin-Film Silicon Solar Cells with Intermediate Reflector

7.1. Introduction

As described in Chapter 6.2 one challenge of the thin-film silicon tandem solar cell technology is the light-induced degradation of a-Si:H layers and the associated deterioration of the electrical properties known as the Staebler-Wronski Effect [6]. To minimize the resulting efficiency loss it is beneficial to reduce the thickness of the a-Si:H top cell [33]. One approach to maintain a high current density with reduced top cell thicknesses, is to introduce an intermediate reflector layer (IRL) made of microcrystalline silicon oxide (μc-SiO$_x$:H) between the sub-cells [44][59][68]. The development of intermediate reflector layers is described in detail in Chapter 6.2. This additional layer has a lower refractive index compared to silicon and reflects a part of the incident light back into the top cell. Thereby, the current density of the top cell and the bottom cell can be matched at a higher level despite the reduced thickness of the a-Si:H top solar cell. It is known that the amount of light kept in the top cell and thus, kept away from the bottom cell is highly dependent on the solar cell texture. A lot of work has been done on the texture and thickness related effectiveness of an IRL. Detailed investigations have been made applying periodic [78] and randomly textured interfaces [79] - [84]. Some precise predictions on the impact of a thickness variation of the IRL on the top and bottom cell current focusing on the LPCVD ZnO:B texture are shown in reference [82]. While other groups focused on finding an optimal thickness of the IRL and its impact on light kept in

the top cell, the emphasis in this chapter is on the impact of a large range of different textures on the effectiveness of an IRL.

The correlation between solar cell topography and short-circuit current density by investigating tandem silicon solar cells with and without IRL fabricated on eight different front textures is discussed. A series of electromagnetic simulations based on AFM measurements of the interfaces taken from these devices after different stages of the production were performed additionally. The optical simulations over a wide wavelength range allow a detailed study of computed modified textures. They make it possible to go beyond experimental limitations and investigate parasitic losses which occur in tandem cell devices.

7.2. Effects of Interface Topographies on the Effectiveness of Intermediate Reflector in Tandem Solar Cells

In this chapter all solar cells were fabricated using a LA-PECVD system (30 × 30 cm²; 13.56 MHz) suitable for eight 5 × 10 cm² substrates. This way, the solar cells were processed at the same deposition conditions. The fabricated tandem cells contain a 300 nm thick a-Si:H top cell and a 1500 nm thick µc-Si:H bottom cell. They were prepared with and without an IRL made of n-type µc-SiO$_x$:H (refractive index $n = 2.5$ at $\lambda = 1000$ nm). The applied IRL is 70 nm thick. A schematic drawing of a tandem solar cell with IRL is shown in Figure 7.2.1.

The types of applied transparent conductive oxides (TCO) front contacts are: sputtered ZnO:Al [29], low pressure chemical vapor deposition (LPCVD) ZnO:B from EPFL in Neuchâtel [30] and atmospheric pressure chemical vapor deposition (APCVD) SnO$_2$:F coated glass from *Asahi Glass Company* (AGC). Two different targets were used for the sputtered ZnO:Al containing 1% and 0.5% aluminum. Sputtered ZnO:Al substrates were etched in 0.5 w/w% HCl and 1 w/w% HF with varied etching time [37][87]. The autocorrelation length (*ACL),* a parameter to describe the lateral size of surface features, the root mean square roughness (σ_{RMS}) and the mean angle of the texture features are derived from AFM measurements [48]. The details of each applied front contact are shown in Table 7.2.1.
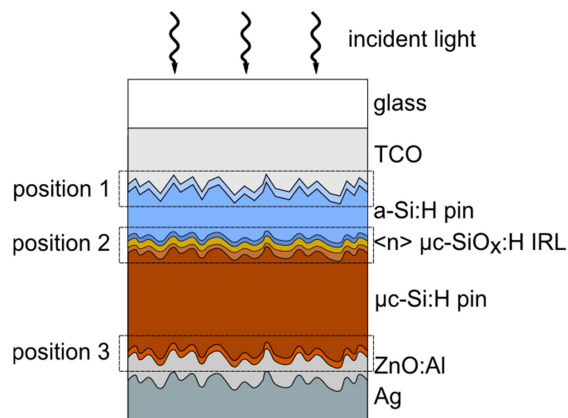
Figure 7.2.1: Schematic drawing of an a-Si:H/µc-Si:H tandem solar cell with an intermediate reflector layer. AFM scans have been carried out at marked positions.

The topographies of the samples at precisely the same spot were characterized by atomic force microscopy (AFM) after different stages of the fabrication process. The stages are shown in Figure 7.2.1. Those are: i) at the front TCO, ii) after the deposition of the a-Si:H top cell and iii) after the deposition of the μc-Si:H bottom cell. The AFM measurements were conducted with a resolution of 1024×1024 pixels for an area of 20×20 μm². For the determination of the photovoltaic parameters and the external quantum efficiency (*EQE*) the solar cells were processed in a separate run. Solar cells deposited on ZnO front contacts included an additional p-type μc-Si:H contact layer to establish an sufficient TCO/p contact. The solar cells deposited on SnO_2:F only contain a p-type a-SiC:H layer.

Table 7.2.1: Overview of applied TCO front contacts, fabrication remarks and surface topography characteristics

type	TCO material	Fabrication remark	*ACL* [nm]	σ_{RMS} [nm]	Mean angle [°]
A	ZnO:Al (1%)	Sputter; 35s HCl etched	715	110	23
B	ZnO:Al (1%)	Sputter; 20s HF / 10s HCl etched	470	80	25
C	ZnO:Al (0.5%)	Sputter; 90s HCl / 20s HF etched	380	70	27
D	ZnO:Al (0.5%)	Sputter; 90s HCl etched	855	125	24
E	ZnO:Al (0.5%)	Sputter; 120s HCl etched	1110	160	21
F	ZnO:B	LPCVD from EPFL	290	80	40
G	SnO_2:F	APCVD Asahi Glass Company	190	35	29
H	ZnO:Al (1%)	flat	5	5	-

Figure 7.2.2 shows the root mean square roughness σ_{RMS} plotted against the autocorrelation length *ACL* for the investigated TCO textures to give an overview of the feature sizes. It is seen that a broad variety of feature sizes have been applied and investigated. A correlation between σ_{RMS} and *ACL* can be observed. However, type F TCO shows a higher roughness and therefore, a higher aspect ratio compared to the other textures resulting in a higher mean angle of 40°.

AFM scans were performed on every TCO at three positions in the tandem solar cell. The evolution of the topography from the front to the bottom texture for type A to G TCO is shown in Figure 7.2.3.

The type A TCO represents a state-of-the-art sputter-etched single-textured ZnO:Al with crater-like features. In general, the topography is relatively flat and contains large features. Type B TCO, show a slightly steeper crater-like structure compared to type A. Also, the ACL is significantly smaller (470 nm). Type C TCO, on the other hand, is a sputter-etched double-textured ZnO:Al with enhanced light scattering properties [86][87].
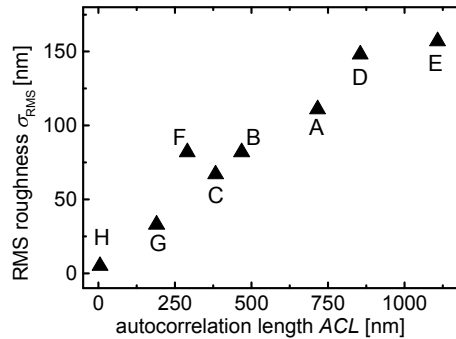
Figure 7.2.2: Autocorrelation length ACL plotted against the root mean square roughness σ_{RMS} of applied front TCO textures.

Here, an additional HF etching step for 20 s was performed subsequently after the HCl etching which results in the formation of steep etch-pits in sub-µm-size. Type D TCO and type E TCO show a similar texture compared with type A and B but with larger features. The ACL is 855 nm and 1110 nm, respectively. Especially for type E TCO a flatter texture with an angular distribution shifted to lower angles is observed. The features include additional smaller and steeper structures than in the case of type A. The texture of type F TCO consists of steep pyramids with an ACL of 290 nm. For type G TCO flatter and smaller pyramids are seen. Generally, the sharp edges which are visible on the bare TCO in Figure 7.2.3 position i) are smoothened after the deposition of the amorphous silicon top cell (position ii)). The AFM images also indicate that the surface topography of the growth model described in reference [86] sufficiently matches to the measured topography after the a-Si:H growth. From literature it is know that this structure complies with a non-conformal growth. The morphology of the back reflector shows additional substructures that occur with a µc-Si:H growth (see Figure 7.2.3, position iii)).
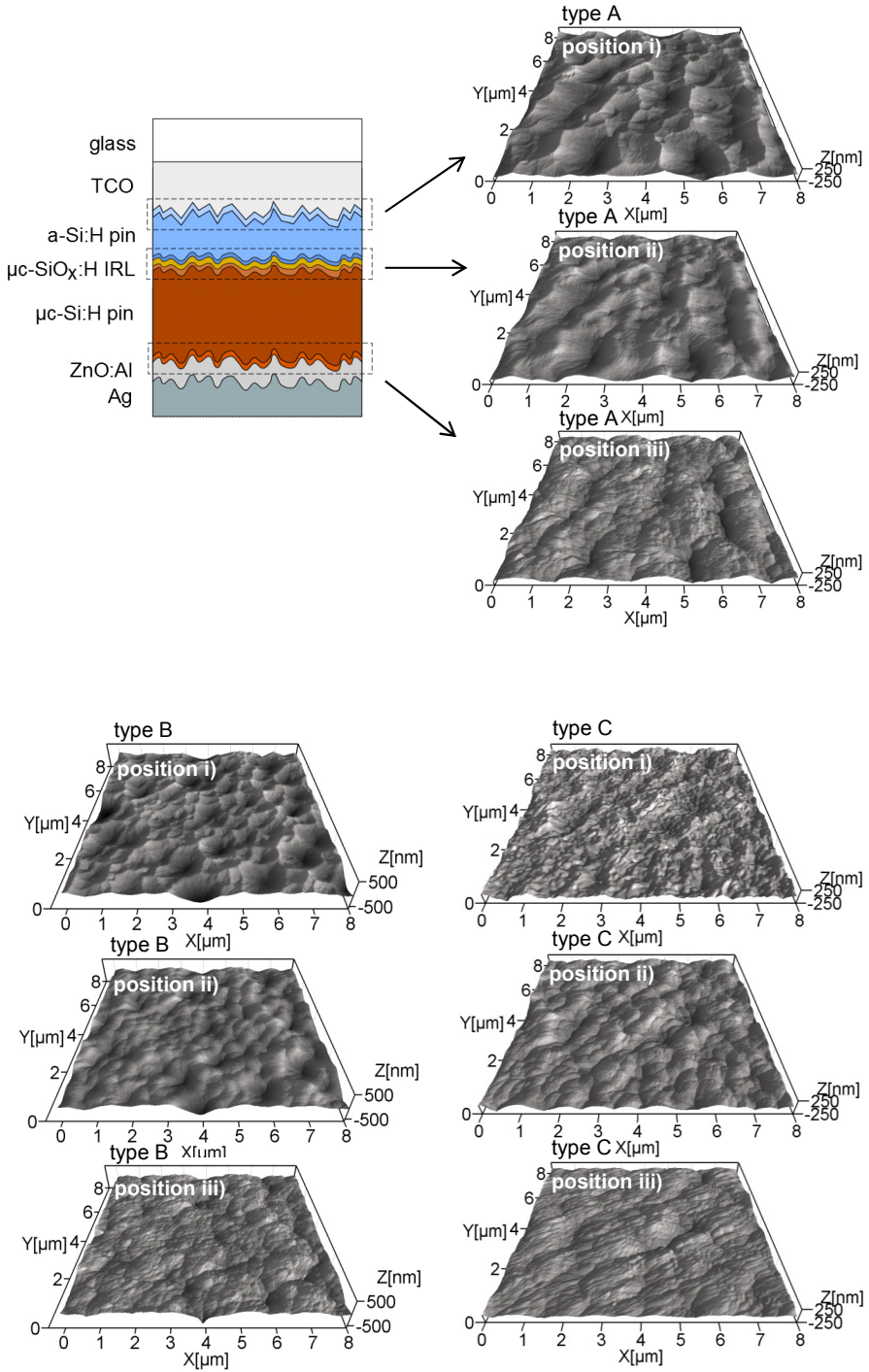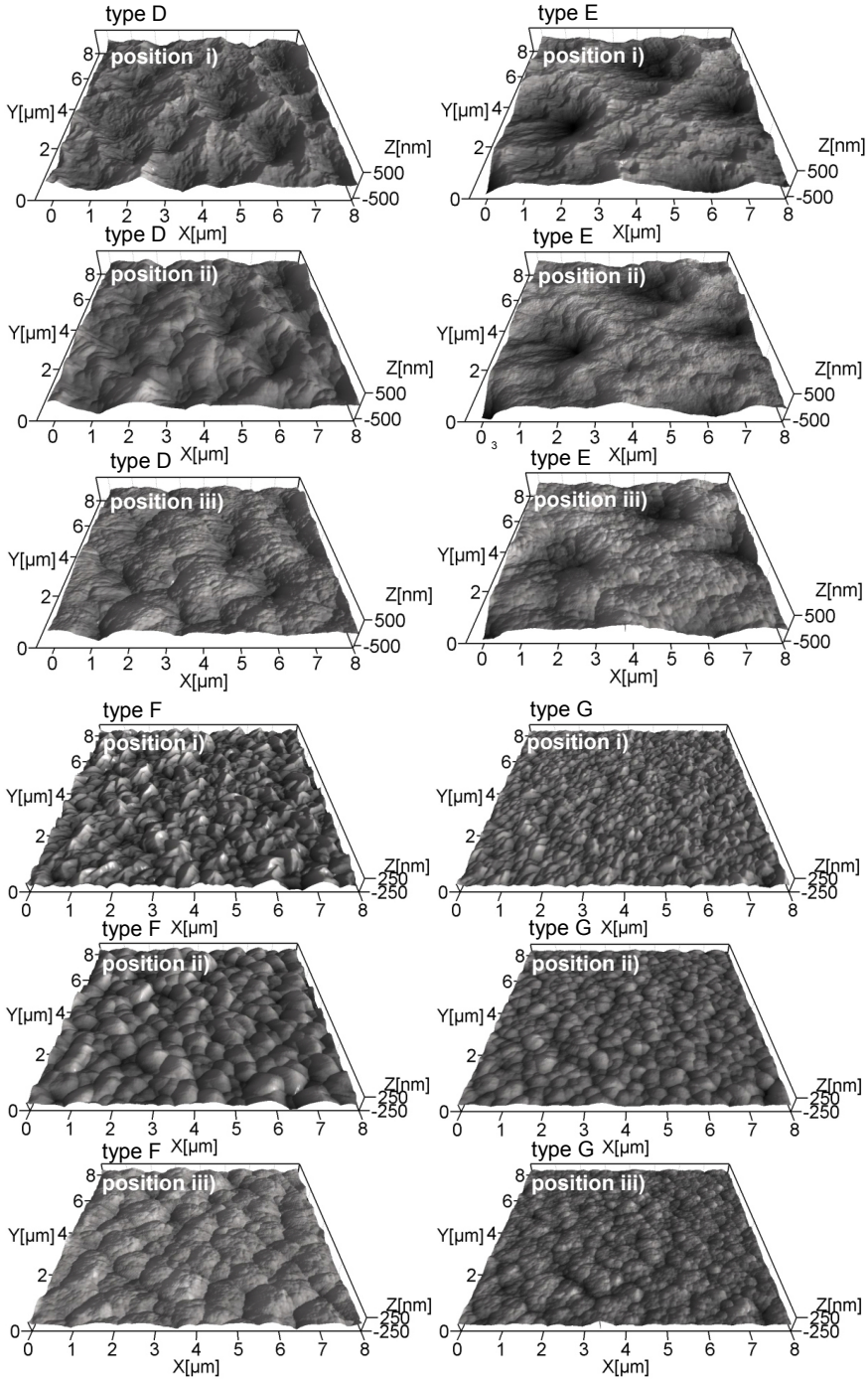
Figure 7.2.3: AFM images measured after different stages of the deposition of tandem solar cells on type A to G front TCO. i) shows the front TCO texture, ii) the a-Si:H top cell texture and iii) the μc-Si:H bottom cell texture. The measurements are taken at each sample for exactly the same area.

Table 7.2.2: Photovoltaic parameters and J_{EQE} of tandem cells deposited on various TCOs, with and without IRL

without IRL

type	η [%]	FF [%]	V_{OC} [V]	J_{SC} [mA/cm²]	$J_{EQE, top}$ [mA/cm²]	$J_{EQE, bottom}$ [mA/cm²]	$J_{EQE, total}$ [mA/cm²]
A	10.4	71.4	1.37	10.6	10.4	14.1	24.5
B	10.2	71.7	1.37	10.4	10.4	13.6	24.0
C	11.1	73.8	1.34	11.2	11.0	13.8	24.8
D	10.1	71.6	1.39	10.1	10.0	12.4	22.4
E	10.4	71.6	1.37	10.6	10.3	13.8	24.2
F	11.3	74.4	1.36	11.2	11.2	14.2	25.4
G	11.0	73.7	1.35	11.0	11.0	11.5	22.5
H	8.8	73.9	1.38	8.6	9.5	8.1	17.6

with IRL

| type	η [%]	FF [%]	V_{OC} [V]	J_{SC} [mA/cm²]	$J_{EQE, top}$ [mA/cm²]	$J_{EQE, bottom}$ [mA/cm²]	$J_{EQE, total}$ [mA/cm²]
A	10.9	71.1	1.38	11.2	11.0	12.2	23.2
B	10.7	70.7	1.36	11.1	11.1	12.0	23.1
C	11.4	71.6	1.33	11.9	12.1	12.2	24.3
D	10.4	72.4	1.38	10.4	10.1	10.8	20.9
E	10.6	71.7	1.38	10.8	10.7	11.1	21.8
F	11.8	72.3	1.36	12.0	12.2	12.3	24.5
G	10.4	79.9	1.34	9.7	12.1	9.5	21.6
H	8.3	81.1	1.37	7.5	9.6	7.0	16.6

In Table 7.2.2 the photovoltaic parameters of tandem cells with and without IRL deposited on various front textures are listed. Additionally, $J_{EQE, top}$ and $J_{EQE, bottom}$ from *EQE* measurements are presented. It is seen that the top and the bottom cell current densities show large differences when comparing solar cells deposited on various front textures. This is driven by a different light scattering and incoupling at each texture. The efficiencies of the tandem cells vary from 8.3% for flat ZnO:Al (type H) to 11.8% for ZnO:B (type F). With exception of the flat front contact (type H) the tandem cells are limited by the top cell and therefore, the introduction of an IRL leads to an improvement of efficiencies due to higher top cell current densities. The V_{oc} of tandem cells without an IRL are in the range between 1.34 V to 1.39 V and with IRL between 1.33 V to 1.38 V. Solar cells deposited on type C and type G show the lowest V_{oc}. Also, solar cells deposited on type F TCO show a rather low V_{oc} with 1.36 V. Flat ZnO:Al (type H) and single textured ZnO:Al (type A; D; E) result in the highest V_{oc}. The fill factors of tandem solar cells deposited on various front textures without an IRL are in the range between

71.4% and 74.4%. In the case with an IRL the differences are larger and range between 70.7% and 81.1%. The highest *FF*s are seen for tandem cells with IRL deposited on type G and H TCO. Tandem cells deposited on type A and B show the lowest *FF*s.

In Figure 7.2.4 the *EQE* and absorptance **(**1-*R***)** of tandem solar cells deposited on type A to H TCO are compared. They reveal different performances in terms of incoupling and trapping of light. The spectral responses of the top as well as of the bottom cells reveal clear differences for each texture. Comparing type A with B TCO, both sputter-etched ZnO:Al, but differing in terms of the feature size, show similar top cell performances for tandem cells without an IRL (10.4 mA/cm²). The bottom cell from type A shows a by 0.5 mA/cm² higher J_{EQE} which is due to the advanced light trapping caused by the large craters. In the case of type C TCO a high bottom cell current is also observed. The top cell shows a higher J_{EQE} (11.0 mA/cm²), which is due to an improved light incoupling and scattering of blue light. That effect is related to the additional etching pits in sub-micrometer size. Solar cells deposited on top of the relatively flat textures like type D and E show a poor spectral response for the top cell. This is linked to the large craters which do not provide a strong incoupling of the blue light. Also, these relatively flat surfaces are not suitable for a good light incoupling. The bottom cell *EQE*s are also effected by an insufficient light incoupling. Solar cells deposited on type E TCO show a higher performance which is comparable with type A. This might be caused by the long etching time and with that a reduction of the front ZnO thickness resulting in a reduction of parasitic absorption. From all samples tandem cells without an IRL deposited on type F TCO (ZnO:B) show the highest $J_{EQE, top}$ (11.2 mA/cm²) and $J_{EQE, bottom}$ (14.2 mA/cm²) and therefore, the highest $J_{EQE, total}$ (25.4 mA/cm²). The good light incoupling and trapping is caused by the steep pyramid-like structure of ZnO:B improving the antireflection and enhancing light scattering into large angles. A similarly strong blue response is seen for solar cells deposited on top of type G TCO (SnO$_2$:F). The small pyramid-like features are highly suitable for light scattering in the short wavelength range resulting in a $J_{EQE, top}$ of 11.0 mA/cm². However, the poor spectral response of the bottom cell with a $J_{EQE, bottom}$ of 11.5 mA/cm² reveal the weakness of a texture with small features. The pyramids in sub-wavelength size (*ACL* = 190 nm) are not suitable to scatter red light in large angles for a good light trapping in the bottom cell. Finally, type H TCO (flat ZnO:Al) show strong cell reflections as wells as interferences. The poor light incoupling results in a weak blue response. Also, the flat ZnO:Al is associated to a low $J_{EQE, bottom}$ of 8.1 mA/cm², since no light trapping texture is included.
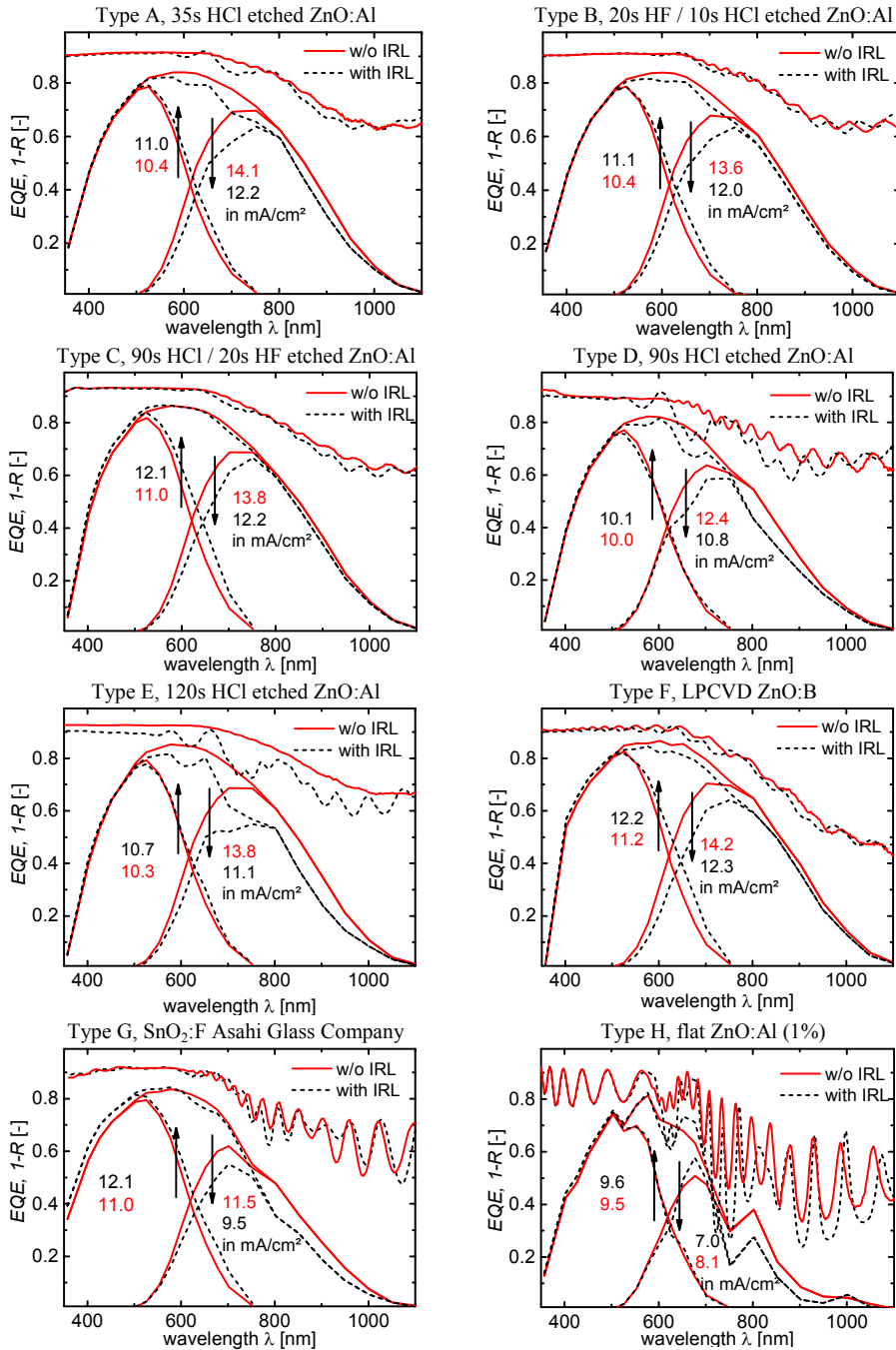
Figure 7.2.4: External quantum efficiency (*EQE*) and absorptance (1-*R*) of tandem solar cells deposited on type A – H TCO front contacts. Dashed black lines indicate *EQE* of solar cells deposited with and solid red lines without IRL. Current densities ($J_{EQE, top}$, $J_{EQE, bottom}$) were calculated from *EQE* measurements for solar cells with and without IRL.

The impact of an IRL on the short-circuit current density of sub-cells in tandem solar cells with an IRL are differently strong for various front textures. The increase of $J_{EQE, top}$ ($J_{EQE, top}$-*gain*) and the decrease of $J_{EQE, bottom}$ ($J_{EQE, bot}$-*loss*) are strongly depend on the type of front texture.

$$J_{EQE, top}\text{-}gain = J_{EQE, top IRL} - J_{EQE, top w/o IRL} \qquad (7.1)$$

$$J_{EQE, bot}\text{-}loss = J_{EQE, bot IRL} - J_{EQE, bot w/o IRL} \qquad (7.2)$$

With an IRL, the $J_{EQE, top}$ of the solar cell deposited on type A TCO was increased by 0.6 mA/cm², while the $J_{EQE, bottom}$ was decreased by 1.9 mA/cm². In the case of type B (smaller and steeper craters) the impact was slightly higher but still, the top cell current density was increased by 0.7 mA/cm², while the $J_{EQE, bot}$ was decreased by 1.6 mA/cm². In contrast, $J_{EQE, top}$-*gain* for a solar cell deposited on type C TCO was 1.1 mA/cm² and $J_{EQE, bot}$-*loss* was 1.6 mA/cm². This can be attributed to the presence of smaller features in combination with higher surface angles. In contrast, tandem cells deposited on type D and E textures show the weakest $J_{EQE, top}$-*gain* (0.1 mA/cm² and 0.4 mA/cm²) in combination with large $J_{EQE, bot}$-*losses* (1.6 mA/cm² and 2.7 mA/cm²). On the other hand, solar cells deposited on top of front textures with pyramid-like features, like type F and G TCO, show large improvements through an IRL. The top cells improvements amount to 1.0 mA/cm² and 1.1 mA/cm², respectively. But unlike type C, which also show a large top cell improvement, tandem cells deposited on type F and G TCO rather large $J_{EQE, bot}$-*losses* (1.9 mA/cm² and 2.0 mA/cm²) are seen. It shows that it is not necessarily that a large $J_{EQE, top}$-*gain* is linked to a large $J_{EQE, bot}$-*loss* by a certain factor. More likely, each texture holds its own characteristics that influence the performance of an IRL individually.

An indication for parasitic losses due to an additional IRL can be derived from ΔJ_{EQE}. It is defined as the difference of the total current density between a tandem solar cell with and without an IRL:

$$\Delta J_{EQE} = J_{EQE, top}\text{-}gain + J_{EQE, bot}\text{-}loss \qquad (6.3)$$

Altogether, the parameters $J_{EQE, top}$-*gain*, $J_{EQE, bot}$-*loss* and ΔJ_{EQE} describe the effectiveness of an IRL. For tandem cells deposited on type C TCO the ΔJ_{EQE} value amounts to -0.5 mA/cm² and -2.3 mA/cm² for type E TCO. Those enormous differences

seen for different front textures open the questions about the loss mechanisms and the impacts of different texture characteristics.
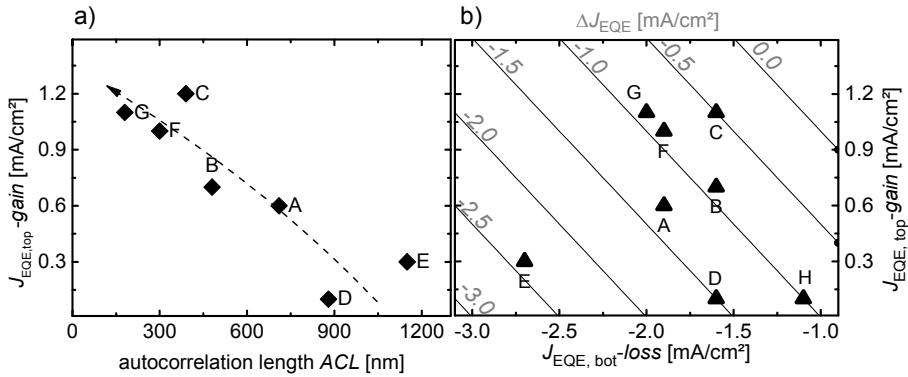
Figure 7.2.5: a) $J_{EQE,\,top}$-*gain* plotted against autocorrelation length *ACL* of TCO front textures. The dashed arrow is a guide to the eye. b) Increase of the top cell current density ($J_{EQE,\,top}$-*gain*) as a function of decrease of bottom cell current density ($J_{EQE,\,bot}$-*loss*) of tandem solar cells caused by an additional IRL deposited on various TCOs. Constant ΔJ_{EQE} is shown in diagonal lines.

Figure 7.2.5 a) shows the correlation between the current improvement in the top cell ($J_{EQE,\,top}$-*gain*) versus the autocorrelation length *ACL* of various TCO front textures. It is seen that especially small *ACL*s of textured TCOs are linked to large $J_{EQE,\,top}$-*gain* values. With increasing *ACL* of applied front textures $J_{EQE,\,top}$-*gain* decreases. In Figure 7.2.5 b) the $J_{EQE,\,top}$-*gain* is plotted against the reduction of the bottom cell current density ($J_{EQE,\,bot}$-*loss*). Constant ΔJ_{EQE} values are included as diagonal lines. It is seen that the IRL effectiveness for tandem solar cells deposited on type C TCO (double-textured ZnO:Al) is by far the highest compared to all other textures. It means that the ΔJ_{EQE} as well as the $J_{EQE,\,top}$-*gain* values are the largest among all applied textures. It is shown that the type C texture makes it possible to improve the ΔJ_{EQE} significantly, which can be attributed to the small and very steep craters created by an HF etching step. For type D and E (large craters), $J_{EQE,\,bottom}$ is strongly reduced without being able to improve the top current density significantly. From Figure 7.2.5 a) it is seen that a front texture with 200 nm $< ACL <$ 500 nm is mandatory for a high $J_{EQE,\,top}$-*gain*. This is in agreement with reference [80] where small *ACL*s have been found to be favorable.
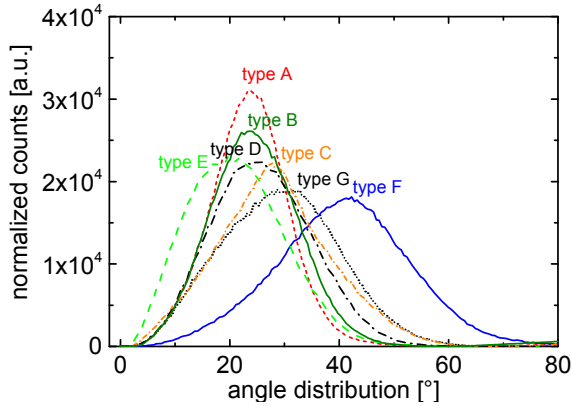
Figure 7.2.6: Normalized surface angle distributions as a function of angle distribution of type A-G TCO front contact textures derived from AFM measurements.

However, the *ACL* alone does not reflect all differences between those textures. For instance, it does not give any information about the roughness or more detailed characteristics of a texture. Therefore, surface angle distributions of various textures have been derived from AFM measurements. The different distributions are shown in Figure 7.2.6. Steeper structures mean that the angle distribution maximum is shifted to larger angles. Type D and type E show the smallest surface angles, meaning that the surface is relatively flat. Those textures have a mean surface angle of ~25°. On the other hand, type C TCO (double-textured ZnO:Al) has the largest surface angles among textured ZnO:Al substrates. Pyramid-like textures show steeper structures. Especially type F (LPCVD ZnO:B) has a large mean angle amounting to 40°.
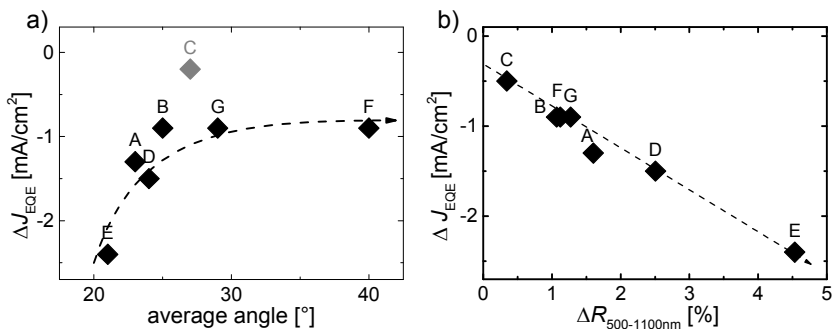
Figure 7.2.7: a) ΔJ_{EQE} shown as a function of average angle of the angular distribution derived from AFM data. b) Correlation between measured ΔJ_{EQE} and ΔR (difference between cell reflection of tandem cells with and without IRL) for tandem cells deposited on TCOs type A - H for a wavelength range from 500 to 1100 nm. Dashed lines are a guide to the eye.

In Figure 7.2.7 a) ΔJ_{EQE} is plotted as a function of average angle from the angular distribution. It is seen that ΔJ_{EQE} is improved with larger structure angles. It should be mentioned that the limiting AFM resolutions could not fully resolve the sub-micrometer sized and steep etch pits in double-textured ZnO:Al (type C) and therefore, the true average angle value of type C might be larger than displayed in the graph.

In Figure 7.2.4 the absorptance 1-R is plotted as a function of the wavelength. It is seen that the additional cell reflectance caused by an IRL is more pronounced for tandem cells deposited on relatively flat textures like type A, D or E compared to rough textures like type C, F or G TCO front contacts. Furthermore, it is supposed that a part of the light, which is reflected back into the top cell and not been fully absorbed in the silicon, might be absorbed in the TCO when passing it for the second time. This effect also seems to be larger in the case of flatter TCOs when comparing the discrepancy between the difference between the red and black lines of the cell reflectance and the total EQE. Also, the interference effects seen for tandem cells with IRL on type A, B, D, E, G and H are reduced in the case of type C and type F.

In Figure 7.2.7 b) the dependency between ΔJ_{EQE} and $\Delta R_{500\text{-}1100\,nm}$ is shown. $\Delta R_{500\text{-}1100\,nm}$ is the difference between the solar cell reflectance of tandem cells with and without IRL for a wavelength range from 500 nm to 1100 nm.

$$\Delta R_{500\text{-}1100\,nm} = R_{cell,\ 500\text{-}1100\,nm,\ IRL} - R_{cell,\ 500\text{-}1100\,nm,\ w/o\ IRL} \qquad (6.4)$$

$$\text{with } R_{cell} = \int_{500nm}^{1100nm} r\,d\lambda \qquad (6.5)$$

A linear correlation for textured TCO types A - G is observed. Type C TCO, the texture with the lowest ΔJ_{EQE} also shows almost no additional reflection when an IRL is introduced. Accordingly, textures with high ΔJ_{EQE} also show large values for $\Delta R_{500\text{-}1100\,nm}$. Especially low ΔJ_{EQE}s are found for solar cells deposited on flatter textures showing large parasitic reflections when an IRL was added. This is due to the increased amount of light, which is reflected in an angle smaller than the angle of total reflection and therefore, not trapped within the solar cell. With this linear correlation it can be assumed that the parasitic losses indicated by the parameter of ΔJ_{EQE} are directly linked or predominately caused by the additional reflection from the IRL out of the solar cell.

7.3. Influence of IRL Thickness on the Performance of Tandem Solar Cells

In order to study the interplay of the topography and thickness of intermediate reflectors the optical performance of a-Si:H/µc-Si:H tandem solar cells were investigated experimentally and by means of rigorous 3-D optical FDTD simulations. In Chapter 6 it is shown that the sum of the top and bottom cell short-circuit current densities decreases with increasing IRL thickness. In the following chapter this effect is studied for different types of front textures.
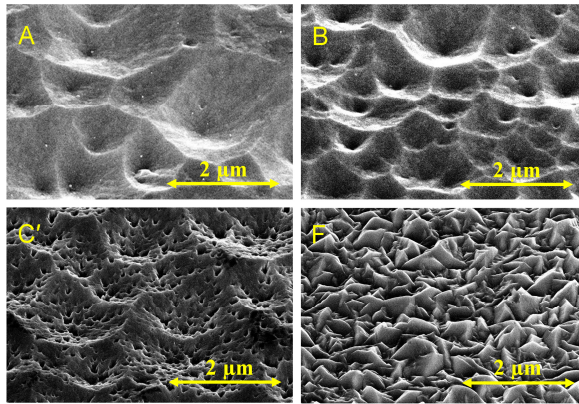
Figure 7.3.1: SEM images of front TCOs described in Table 7.3.1. Type A: HCl etched ZnO:Al with large craters, type B: HF and HCl etched ZnO:Al with small and steeper craters, type C′: HCl and HF etched ZnO:Al with large and small crater features (double-textured), type F: LPCVD ZnO:B pyramid like surface topography.

Figure 7.3.1 shows SEM images of the four different surface textures that were used. Type A: single textured sputter-etched ZnO:Al etched in an HCl solution (0.5%) with large craters, type B: HF (1%) and HCl (0.5%) sputter-etched ZnO:Al with small and steeper craters, type C′: HCl (0.5%) and HF (1%) etched ZnO:Al with large and small crater features (a similar double texture as type C presented in Chapter 7.2, but with a different ZnO:Al containing 1% Al), type F: low-pressure chemical vapor deposited (LPCVD) ZnO:B pyramid like surface topography (2.5-µm thick grown layers with low boron doping, post treated with a smoothening argon plasma after deposition [91]). The ZnO:Al consists of ~1 µm ZnO:Al-layer sputtered on Corning-glass. After the etching step in HCl a surface-texture consisting of contiguous craters with diameters of 0.5 µm to

1.2 µm are fabricated. In case of type C an additional HF etching step (1%) for 10 s of the ZnO:Al surface was performed subsequently. In that step sub-micrometer sized etch-pits are formed. The specifications are listed in Table 7.3.1.

Table 7.3.1: Applied TCO front contacts and characteristics for tandem solar cells with intermediate reflector layer. The autocorrelation length *ACL* and root mean square roughness σ_{RMS} were derived from atomic force microscopy (AFM) scans.

Type	TCO material	Fabrication remark	*ACL* [nm]	σ_{RMS} [nm]
A	ZnO:Al (1%)	Sputter; 35s HCl etched	715	110
B	ZnO:Al (1%)	Sputter; 20s HF / 10s HCl etched	470	80
C′	ZnO:Al (1%)	Sputter; 30s HCl / 10s HF etched	630	125
F	ZnO:B	LPCVD from EPFL	240	100

In Figure 7.3.2, the measured top and bottom J_{EQE} values for tandem solar cells containing a 350 nm thick top and a 1560 nm thick bottom cell are shown. The solar cells were deposited with different thicknesses of the IRL layer: 0 nm, 40 nm, 70 nm and 100 nm. The refractive index *n* of th the IRL was 2.5.
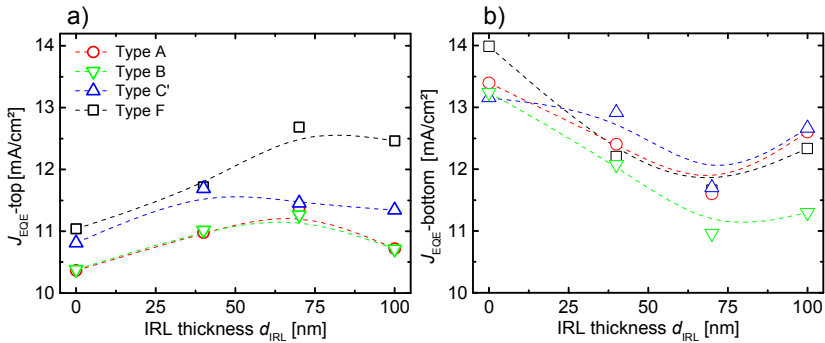
Figure 7.3.2: a) Top cell short-circuit current density $J_{EQE, top}$ as a function of IRL thickness d_{IRL}; b) Bottom cell short-circuit current density $J_{EQE, bottom}$ as a function of IRL thickness d_{IRL} for tandem solar cells deposited on type A, B, C′ and F TCOs described in Table 7.3.1.

Similar trends are observed for different TCO topographies. $J_{EQE, top}$ increases with increasing thickness of the IRL d_{IRL} until a maximum is reached. The maximum was found for type A, B and F at d_{IRL} = 70 nm, while for type C′ the maximum was found for

d_{IRL} = 40 nm. At the same time, the bottom cell short-circuit current density decreases with increasing top cell short-circuit current density and reaches a minimum at d_{IRL} = 70 nm for all cases.

Table 7.3.2: Photovoltaic parameter and J_{EQE} of tandem cells deposited on various TCOs, with and without IRL. The parameters for solar cells with IRL refer to results found for a maximum gain in the top cell.

without IRL

type		η [%]	FF [%]	V_{OC} [V]	J_{SC} [mA/cm²]	$J_{EQE, top}$ [mA/cm²]	$J_{EQE, bottom}$ [mA/cm²]	$J_{EQE, total}$ [mA/cm²]
A		9.6	65.8	1.39	10.5	10.4	14.0	24.4
B		9.8	68.3	1.36	10.5	10.4	13.2	23.6
C′		10.0	67.4	1.36	10.9	10.8	13.2	24.0
F		10.3	69.3	1.33	11.2	11.0	14.0	25.0

with IRL (optimal thickness for maximum top cell current density gain)

type	d_{IRL} [nm]	η [%]	FF [%]	V_{OC} [V]	J_{SC} [mA/cm²]	$J_{EQE, top}$ [mA/cm²]	$J_{EQE, bottom}$ [mA/cm²]	$J_{EQE, total}$ [mA/cm²]
A	70	10.2	66.7	1.36	11.3	11.4	11.6	23.0
B	70	9.8	69.5	1.31	10.8	11.2	11.0	22.2
C′	40	11.1	69.3	1.34	11.9	11.7	12.9	24.6
F	70	9.8	67.3	1.27	11.5	12.7	11.7	24.4

It has been shown by simulations that LPCVD ZnO:B based front textures have the highest optical potential when combined with a thin IRL with low refractive index [90][91]. In our experiments it is seen that $J_{EQE, total}$ for tandem cells deposited on type F TCO show the largest value, in the case without an IRL. Also, for type F TCO the top cell short-circuit current densities improves with a high slope to a $J_{EQE, top}$ -*gain* of 1.7 mA/cm² for the optimal d_{IRL}. Like in Chapter 7.2 it is seen that the strongest light scattering and incoupling is obtained for solar cells deposited on type F (ZnO:B). For tandem solar cells deposited on type A, B and C′ TCO (crater structures) the $J_{EQE,top}$ -*gain* is only ~0.9 mA/cm² for the optimal d_{IRL}. Despite the high $J_{EQE, top}$ -*gain* for type F the reduction of the bottom cell short-circuit current density $J_{EQE, bot}$ -*loss* remains at a relatively low value of -2.3 mA/cm². Only type C′ TCO losses less in the bottom cell (-1.4 mA/cm²) for d_{IRL} = 70 nm. Similar conclusions as in Chapter 7.2 can be drawn in the case of double textured ZnO:Al, where the small features increase light scattering into larger angles beneficial for light trapping in the bottom cell.

7.4.   Finite-Difference Time-Domain Simulations

Optical simulations are performed to support experimental findings and one step further, to overcome given experimental limitations. For the Finite-Difference Time-Domain (FDTD) simulations that solve Maxwell's equations rigorously [53][54] AFM data measured for each interface texture serves as input parameter. The optical constants of the front contact layers were assumed for all cases to be the ones of ZnO:Al. n and α for the ZnO:Al, a-Si:H and μc-Si:H were determined by reflection/ transmission measurements and photothermal deflection spectroscopy. The glass/ZnO:Al interface was assumed to be flat while all other interfaces were textured using topographies from AFM measurements for interlayer textures at positions i), ii) and iii).

7.4.1 FDTD Simulations of Tandem Solar Cells on various front Textures

The most efficient solar cells were deposited on textures C, F and G (see Chapter 7.2, p. 88). They show σ_{RMS} and *ACL* values within a certain range. Thus, to achieve a deeper understanding on the individual impact of structure type and feature size on the effectiveness of the IRL, three-dimensional electromagnetic simulations were carried out. The simulations allow using modified textures with adjusted *ACL*, feature height and consequently the feature steepness. That makes it possible to look beyond the experimental limits by the texturing process. For validation, the absorptance in top and bottom solar cells derived from simulations based on the interface textures of type A TCO are presented exemplarily in Figure 7.4.1 a).
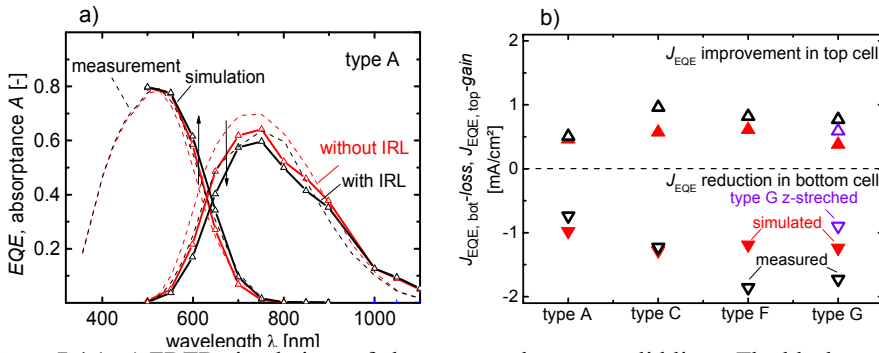
Figure 7.4.1: a) FDTD simulations of absorptance shown as solid lines. The black curves represent the absorptance of a tandem solar cell with and the red curves without an IRL. As a reference the measured *EQE* of a tandem solar cell with IRL is shown as dashed lines. The employed interface textures are from type A TCO (single-textured ZnO:Al). b) Comparison between J_{EQE} derived from measurements and simulations of short-circuit current density gain in the top cell and loss in the bottom cell for a wavelength range from 500 nm to 1050 nm. Investigated TCOs are single-textured ZnO:Al (type A), double-textured ZnO:Al (type C), LPCVD ZnO:B (type F) and SnO$_2$:F (type G). Results for a stretched modification of type G TCO in the z-direction is marked by violet triangles.

The comparison with experimental data of solar cells deposited on the same front texture (type A) show a higher computed absorptance for the top cells. Though, for the bottom solar cell the simulated absorptance is lower than the measured *EQE,* the effect of the intermediate reflector, maintaining light in the top cell and therefore, reducing the short-circuit current density of the bottom cell, has been successfully reproduced by simulations. Further, simulations of tandem solar cells based on the measured interlayers of type C, F and G TCO are carried out. These front textures have been shown to perform in a diverse way and are widely used in research and industry. The results of improvement of $J_{EQE, top}$ and reduction of $J_{EQE, bottom}$ due to the introduction of an IRL are shown in Figure 7.4.2 b). In general, simulated and measured solar cells show similar trends in terms of the $J_{EQE, top}$-*gain* and the $J_{EQE, bot}$-*loss*. For $J_{EQE, top}$-*gain* of solar cells on type A and for $J_{EQE, bot}$-*loss* of type C TCO the agreement can be seen as excellent. A few differences for bottom solar cells on top of type F and G textures are seen. In this series of simulations the difference of the TCO material was not considered. As the TCOs vary not just by texture but also by thickness and refractive index, simulations were carried out holding theses parameters constant and just varying the surface texture. In all simulations the optical data of ZnO:Al (1%) were used. Thus, an influence of the TCO material can

be seen as a source of error to explain the mismatch between experiment and simulation. However, comparison of simulations and measured *EQE*s show a sufficiently reliable agreement for various textures.
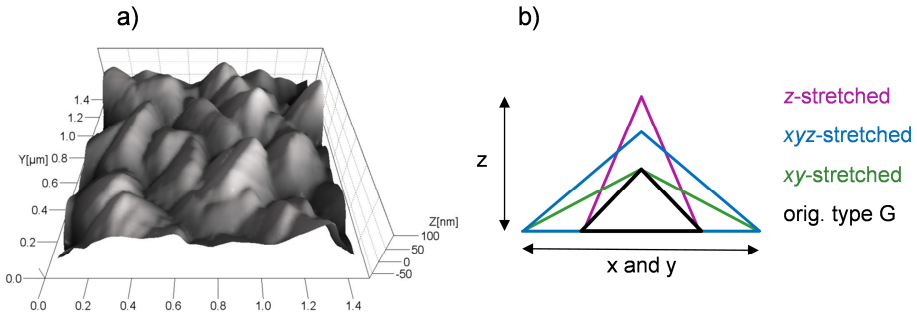

Figure 7.4.2: a) AFM image of a small section of a SnO$_2$:F (type G) texture. b) Schematic drawing of different modifications performed for the type G texture by stretching of width and height.

In the next step, solar cells on top of a series of artificially stretched textures based on measured SnO$_2$:F texture (type G) (Figure 7.4.2 a)) are simulated. Type G texture was chosen, because tandem cells deposited on top of this TCO show a satisfactory $J_{EQE, top}$-*gain*, but also a high $J_{EQE, bot}$ -*loss*. The impact of a stretching of the height of a texture was already investigated previously [83], where the focus was the impact on the improvements in the top cell current. The effects on the absorptance in the bottom cell due to modified textures are presented in the following.

The differently modified textures are shown in a schematic drawing in Figure 7.4.2 b). They consist of a lateral stretching (*xy*-stretching), a stretching in three dimensions (*xyz*-stretching) and a stretching only of the height (*z*-stretching). The *xy*-stretching was implemented in a way that the *ACL* of the modified type G texture is equal to ZnO:B (type F). *xyz*-stretching result in a simply enlarged version of type G texture with the same *ACL* and height compared to type F TCO. The third modification is a stretching of height by a factor of 1.5. These modifications allow studying the impact of the lateral structure size and the steepness on the effectiveness of an IRL individually. That way, findings can contribute to the design of optimized textures for intermediate reflectors. The stretching was carried out for measurements of the texture at position i) and iii). For position ii) a non-conformal growth model was applied. The model is described in reference [88] and is based on the stretched texture from position i).
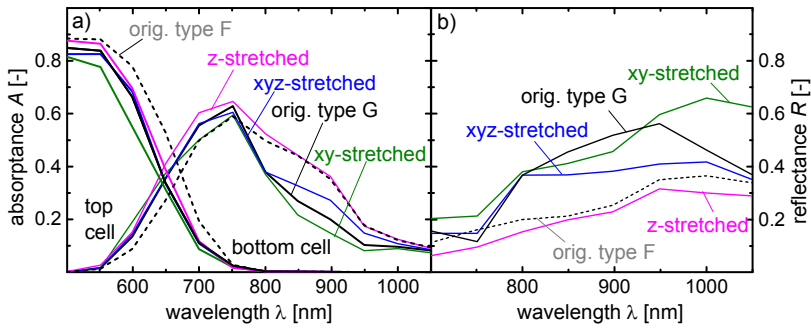
Figure 7.4.3: a) Simulated absorptance A by FDTD of tandem cells with IRL for various stretching modifications based on SnO_2:F (type G) front texture. b) Simulated reflectance R of tandem solar cells with IRL for a wavelength range between 700 nm and 1000 nm. Simulations using LPCVD ZnO:B (type F) texture (dashed lines) are shown as a reference. Simulated reflectance of a tandem cell without IRL on top of type F textures is shown as a dotted line.

Results of the simulated absorptance A of tandem solar cell sub-cells with IRL by FDTD for stretching modifications of type G TCO are shown in Figure 7.4.3 a). Very pronounced effects are observed in the bottom cell absorptance. The xy-stretching causes a flattening of the texture and led to a decrease of bottom cell A compared to the original texture of type G TCO. The xyz-stretching however, improves the absorptance in the bottom cell, which is due to an enhanced scattering of light with larger wavelengths. Finally, the most pronounced effects are observed for the z-stretched texture. Top and bottom cell absorptance computed for this modification of type G TCO are increased and even exceed the absorptance of solar cells with a type F texture (ZnO:B). The improvements compared to unmodified type G TCO in terms of short-circuit current density are presented in Figure 7.4.1 b). The $J_{EQE,\ top}$ -gain for the z-stretched texture amounts to 0.59 mA/cm², while for the unmodified type G textures only 0.38 mA/cm² was simulated. Accordingly, the $J_{EQE,\ bottom}$ -loss for the z-stretched texture amounts to -0.9 mA/cm² and for unmodified type G texture it is -1.24 mA/cm². The effectiveness of the IRL has been improved by a stretching of the applied textures. The simulated solar cell reflectance is shown in Figure 7.4.3 b). A strong dependency between the modified structures and the solar cell reflectance is seen. A strong decrease of the reflectance is observed for the z-stretched compared to simulation done for unmodified type G textures. In turn, the flattened xy-stretched structures show an enhanced cell reflectance. Simulated and experimental data shown in Figure 7.4.1 and Figure 7.2.7 b), where a

correlation between ΔJ_{EQE} and $\Delta R_{\mathrm{500\text{-}1100\,nm}}$ is seen, indicate that parasitic reflection of light from the IRL out of the solar cell is mainly responsible for the loss of bottom cell current, when comparing tandem solar cells with and without IRL. In this respect, the steepness of the texture is the most relevant measure. Similar effects are seen for the experimental data.

7.4.2 FDTD Simulations of Transmittance
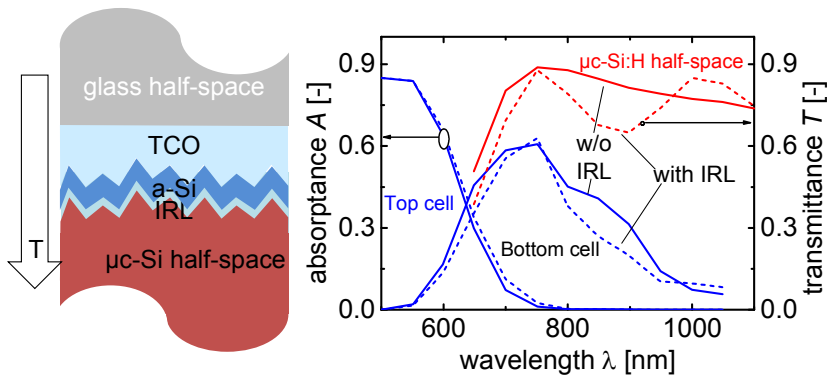
Figure 7.4.4: Simulated transmittance (red lines) from a top cell into a silicon half-space (see schematic drawing) as a comparison to the simulated bottom cell absorptance (blue lines). Dashed lines indicate the presence of an IRL. For simulations SnO$_2$:F (type G) textures were applied.

To distinguish the reflection effects caused by the IRL and the back reflector, transmittance through the top cell and IRL are simulated for the case in which the bottom cell is substituted by a silicon half-space, see Figure 7.4.4. It is seen that the transmittance is in agreement with the *EQE*. The same dip at ~850 nm is seen for the *EQE* as well as for the transmittance for the case with an IRL. It shows that the effect of the reduced *EQE* is in fact due to reflection losses from the IRL and not from the back reflector.

7.4 3 FDTD Simulations on the Influence of IRL Thickness

Figure 7.4.5: Simulated absorptance for $\lambda = 650$ nm ($A_{top,\,650nm}$) of a top cell with various thicknesses of the IRL applied for a LPCVD ZnO:B and an APCVD SnO$_2$:F texture.

To confirm the trends found for various thicknesses of the intermediate reflector layer d_{IRL} inside a tandem solar cell seen in Chapter 7.3, FDTD simulations were performed. These simu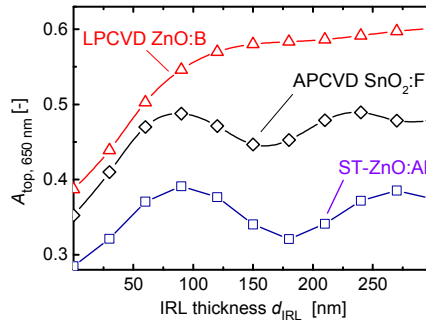lations cover a wider range of d_{IRL} (0 - 300 nm) compared to the experiments and were carried out in 30 nm steps. Here, only the absorptance of the top a-Si:H cell at a wavelength of 650 nm ($A_{top,\,650nm}$) was considered and it is supposed that this value gives a most representative measure for the evolution of the top cell short-circuit current density. The simulations are performed for solar cell stacks consisting of an a-Si:H top cell, an IRL and a µc-Si:H half space and are applied on LPCVD ZnO:B, APCVD SnO$_2$:F and single-textured ZnO:Al textures. The evolution of $A_{top,\,650nm}$ as a function of the IRL thickness for tandem cells on top of different textures are shown in Figure 7.4.5. The top cell absorptance for all cases increases in a steady slope to a $d_{IRL} = 60$ nm. When increasing d_{IRL} further an oscillation *for $A_{top,\,650nm}$* is seen. A Fabry-Pérot oscillation with formation of clear maxima and minima in the case of APCVD SnO$_2$:F and single textured ZnO:Al is observed. The $A_{top,\,650nm}$ is lager in the case of LPCVD ZnO:B texture for all d_{IRL} compared to other textures. Furthermore, the oscillation for larger d_{IRL} is much weaker. Clear maxima and minima are not seen here.

Similar trends are also seen from experimental results (Figure 7.3.2). They show a decrease of the top cell current densities after a maximum was observed for a certain IRL thickness. Nevertheless, the position of the maximum point in the case of experimental data for single textured ZnO:Al is located at $d_{IRL} = 70$ nm, while for simulation it is at 90 nm. Also, for LPCVD ZnO:B the maximum is seen more clearly in the experiment.

The discrepancies between experiments and simulations might be caused by optical input parameters for the simulations that vary from the experiments. Input parameters are for example absorption coefficient, refractive index and also layer thickness. For experiments d_{IRL} was calculated from the deposition time and deposition rate that was obtained by single layer depositions on flat glass substrates. Inside a solar cell device however, the growth conditions are different. It can be changed for example by the substrate material as well as the topography. Furthermore, in the experiments only a small number of data points are applied. It means that the location of the real maximum might differ from the maximum seen in the graphic. These error sources have to be taken into account when comparing those results. Still, the trend seen for experiments and simulations are clear in respect of showing an increasing $J_{EQE, top}$ with increasing d_{IRL} until a maximum is reached.

7.5.   Discussion and Conclusion

There has been a continuous interest of several research groups engaging in the question regarding the interplay between the front texture, the thickness of an IRL and the effectiveness of an IRL.

Pellaton-Vaucher et al. already investigated in early works 1998 the interplay between texture, IRL thickness and light management by experiments and simulations [81]. The cell reflectance was attributed to the texture's surface angle. Also, it has been predicted that the total current density is correlated to the cell reflectance.

Dominé et al. [82] made detailed investigations on the impact of the IRL thickness applying a three layer effective media approximation. They calculated that the top cell current density increases by 0.03 mA/cm² per additional nanometer of IRL thickness and the bottom cell current density decreases by 0.04 mA/cm² per nanometer until a maximum is reached at around $d_{IRL} = 90$ nm. An optimized LPCVD ZnO:B texture was applied and it was found that the gain and loss in the sub cells were almost linear until a plateau is reached. This study distinctly differs from the trends seen for flat solar cells, where Fabry-Pérot oscillation dominates the effect. The results from in Chapter 7.3 are in agreement with findings presented in ref. [82].

Rockstuhl et al. [83] also investigated the impact of a stretching in the z direction. Starting from randomly textured surfaces of SnO_2:F, ZnO:Al and ZnO:B they used a model consisting of a front TCO, an a-Si:H top cell and an IRL with various thicknesses. The investigations concentrate on the impact on the improvements in the top cell current density and due to simplifications in the model it was not possible to predict the effects on the bottom cell short-circuit current density. Nevertheless, key statements are in agreement with findings presented in this chapter. It came out that even though the ZnO:Al show a large haze, it does not scatter light into large angles and therefore, the improvement in the top cell is limited. The *ACL* of the SnO_2:F texture is stated to be too small (sub-wavelength range) that it is more likely to act as an effective medium instead of a light scattering structure. However, only a scattering into large angles, like in the case of ZnO:B texture, can enhance the top cell short-circuit current density. Rockstuhl et al. could also show further improvements due to increasing the roughness of the texture by a stretching into the *z*-direction.

Detailed simulations of tandem cell *EQE*s were also performed by Obermeyer et al. [78]. Their investigations consider periodic structures, which differ significantly in an optical point of view compared to randomized structures. Anyhow, a few findings are relevant for the understanding of tandem solar cells with an intermediate reflector. From a series of modified periodic pyramids it was proposed that an optimal structure size for a good light incoupling into the top cell was 300 – 400 nm and for a good light trapping in the bottom cell the optimal structure size was 1200 – 1600 nm. An optimal IRL should be 70 – 100 nm thick. Also, it was stated that single features cannot be optimized independently since the interaction of the interface textures determines the optics of a whole tandem cell device.

The most comprehensive paper to now on the texture and thickness related effects of intermediate reflectors was published by Kirner et al. [80]. The group carried out detailed investigations of tandem solar cells deposited on SnO_2:F, ZnO:Al and ZnO:B textures by simulations and experiments. The optical simulations were carried out using a finite-element method applying AFM-measured front textures. The thickness related sub cell short-circuit current densities are compared for different front textures. A large d_{IRL} dependency for the top cell short-circuit current density was observed for solar cells with a ZnO:B to a maximum, until further thickness incensement lead to Fabry-Pérot resonances. A weaker thickness dependency for solar cells deposited on SnO_2:F and ZnO:Al is seen, while the begin of the resonances occurs already for thinner IRLs. This is explained by the amount of light being reflected in the orthogonal direction, which increases in oscillation period. The comparison between simulated and measured results shows some quantitative discrepancy, but is qualitatively in a good agreement. Also, it has been predicted that small *ACL* are essential to a good IRL performance. These findings are in agreement of results described in Chapter 7.2 and 7.3.

Simulations obtained in this chapter use fewer simplifications as compared to other works in this field, which result in good agreements with experimental results. In contrast to other groups investigating randomized textures, the simulations carried out in Chapter 7.4 considered a broad wavelength range instead of focusing on only two or three wavelengths which renders possible to simulate *EQE*s.

In the current chapter the interplay between the various topographies and the performance of the intermediate reflector in thin-film silicon tandem solar cells were investigated. Differences in terms of morphology, light scattering and effectiveness of the IRL were observed. Experimental results show that high performances were achieved

with front textures with an *ACL* between 200 nm and 500 nm. The best IRL performance was found for double-textured ZnO:Al. Compared to single textured ZnO:Al the *ACL* is smaller and the feature steepness is higher. The steepening of a texture shows an enhancement of $J_{EQE, top}$ and a significant reduction of $J_{EQE, bottom}$ in tandem cells with an IRL. The enhanced $J_{EQE, top}$ is a result of improved light incoupling due to a better refractive index matching improving the antireflection effect and of enhanced light scattering into large angles. The improvement of the bottom cell is linked to a reduction of parasitic reflection of light from the IRL out of the solar cell. The comparison of the cell reflection between tandem cells with and without an IRL shows this effect clearly. A reduced reflectance also means that more light is trapped within the solar cell which leads to an improvement of the effectiveness of an IRL. It is shown that for the design of an optimized texture, steeper structures are preferred to achieve improved light management for both sub-cells in tandem solar cells.

The optical advantages of very steep structures might be companioned with a worsening of the electrical performance. As seen, the V_{oc} for solar cells deposited on double-textured ZnO:Al (type C TCO) and LPCVD ZnO:B (type F) are lower compared to other textures. A smoothening of the IRL would be beneficial to the V_{oc} and *FF*, as seen in references [89][92], and a trade-off between optical and electrical effects has to be taken into account.

The possibility to compute the sub-cell absorptance of tandem devices makes optical simulations by the FDTD method a powerful tool. They render possible the investigation of systematically modified structures. The steepness of a texture shows link to the improvement of $J_{EQE, top}$ and the reduction of the $J_{EQE, bottom}$-*loss*. The effect of reduced parasitic reflection has also been confirmed by systematic investigations considering various texture steepnesses. Findings on the effective utilization of light within a tandem solar cell with an intermediate reflector layer will contribute to the design of solar cells with higher conversion efficiencies.

Chapter 8
Electrical Issues at the TCO/p
and p/i Interface

8.1. Introduction

The improvement of electrical properties in thin-film silicon solar cells of various interfaces, particularly the improvement of the TCO/p and p/i interface has been receiving extensive attention. Those interfaces are marked in a sketch in Figure 8.1.1.
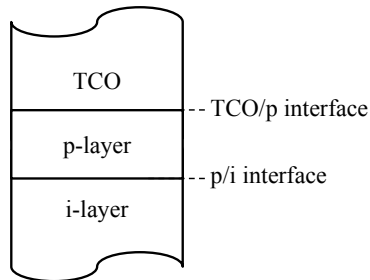
Figure 8.1.1: Sketch of the TCO/p and p/i interface of a solar cell in p-i-n configuration.

As a sensitive region for a solar cell at which holes and electrons recombine, the electrical contact between the TCO and p-layer is of special importance. The TCO/p contact for a-Si:H solar cells deposited on doped zinc oxide has been in the focus of research since early years [93] -[101]. The bad fill factor is a mandatory drawback when depositing a p-type a-SiC:H layer on top of ZnO:Al front contact. From the *JV*-curve a TCO/p interface problem is assumed. In reference [98] it is shown that in the case of a

SnO:F/(p) a-SiC:H contact a linear behavior of the dark *I-V* measurement indicate a low ohmic resistance, while in the case of ZnO:Al a nonlinear behavior was observed, see Figure 8.1.2.
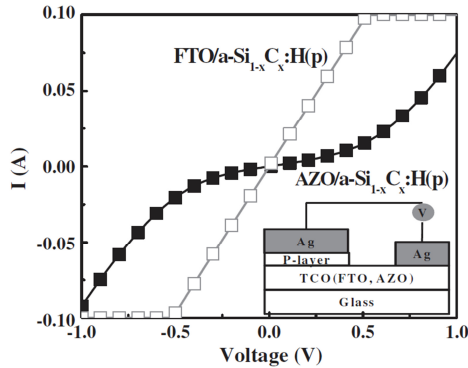

Figure 8.1.2: Dark *I-V* measurements of the TCO/(p) a-SiC:H interface. As TCOs ZnO:Al (aluminum doped zinc oxide AZO) and SnO:F (fluorine doped tin oxide FTO) are compared, Lee et al. [98].

Commonly, the formation of a Schottky-contact is used as a model for describing such behavior [96][97]. To overcome the contact resistivity or the energy barrier formed at the interface through band bending, the concept of an additional contact layer made of doped microcrystalline silicon (μc-Si:H) has been introduced [95] - [99]. Such a contact layer possesses the capability to have a much higher doping concentration and therefore, it allows a reduction of the energy barrier [95]. Also, more recent publications show an increased interest on the investigation and improvement of the TCO/p contact for the application in heterojunction solar cells [100][101]. One approach to improve the optical properties of thin-film silicon solar cells is to reduce the rather high absorption losses caused by the p-type μc-Si:H contact layer. Therefore, more transparent p-type microcrystalline silicon oxide (p-type μc-SiO$_x$:H) is implemented as a contact layer to substitute the p-type μc-Si:H layer.

In this chapter, the TCO/p contact of ZnO:Al and a-Si:H cells including a p-type μc-SiO$_x$:H layer by variation of various process parameters are investigated and discussed. Second, a lower V_{oc} was measured for a-Si:H solar cells with a p-type layer consisting of only a p-type μc-SiO$_x$:H layer. On the other hand, such a decrease of V_{oc} has not been observed for μc-Si:H solar cells. It is supposed that a different intrinsic layer and

therefore a different p/i- interface is responsible for this electrical behavior. There have been intensive efforts on the improvement of electrical properties of the p/i interface by insertion of an additional intrinsic silicon oxide [102] - [104] or intrinsic amorphous silicon carbide [105] as a buffer layer by various groups. Thus, in this chapter findings concerning the impact of various intrinsic buffer layers inserted between the p-type μc-SiO$_x$:H layer and the intrinsic a-Si:H absorber layer are presented and discussed.

Finally, the effect of the front contact morphology on the V_{oc} of a solar cell is investigated on various textured TCOs. It has been observed that a lower V_{oc} is measured for highly textured front TCOs. Especially for μc-Si:H solar cells these effects are crucial and are discussed in literature [106][107]. There, the deterioration of V_{oc} is explained by the formation on cracks and thus, nano-shunts in the solar cell. For a-Si:H solar cells similar effects are observed with very rough front TCOs [85] even though no crack formation is seen by electron microscopy [109]. In this paragraph the origin of voltage losses is discussed based on a series of solar cells deposited on top of various front textures while varying the thickness of the intrinsic layer of the solar cells.
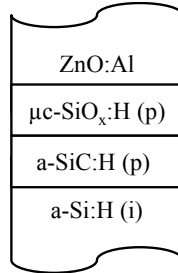
8.2.   TCO/p Contact in a-Si:H Solar Cells

Figure 8.2.1: Schematic drawing of thin-film silicon a-Si:H solar cells containing a p-type microcrystalline silicon oxide (μc-SiO$_x$:H) as a contact layer between the ZnO:Al and a-SiC:H p-layer.

In Figure 8.2.1 a sketch represents the p-layer configuration for an a-Si:H solar cell device containing p-type microcrystalline silicon oxide. Different shapes of the *JV*-curve are seen when applying different layer thickness for the p-type μc-SiO$_x$:H contact layer between the front contact (single textured ZnO:Al) and the amorphous silicon carbide p-layer (a-SiC:H). Figure 8.2.2 shows *JV*-curves of a-Si:H solar cells with varied thicknesses of p-type μc-SiO$_x$:H layers (2 nm to 8 nm). The layer thickness was calculated from the deposition rate of ~1 Å/s. The applied p-type μc-SiO$_x$:H contact layers have a band gap of 2.3 eV, a refractive index of 2.3 and a conductivity of 3×10^{-5} S/cm. A solar cell with a standard p-type μc-Si:H contact layer is shown as a reference. Also, a solar cell without any contact layers, i.e. only a p-type a-SiC:H layer, is presented. An "S"-shape behavior of the *JV*-curve of the solar cell without a contact layer is seen. Such an "S"-shape is seen as a result of band bending and formation of potential barriers at the TCO/p interface. It leads to a reduction of the fill factor. The reference solar cell with a p-type μc-Si:H contact layer has a fill factor of 68.2%. When replacing the standard contact layer by a p-type μc-SiO$_x$:H layer of different thicknesses, clear changes regarding the *FF* and the *JV*-curve shape can be seen. While a 2 nm thick p-type μc-SiO$_x$:H contact layer still result in a clear "S"-shape (*FF* = 57.1%), the fill factor of a-Si:H cells improved continuously with thicker contact layers. Finally, the "S"-shape vanishes. For the 8 nm thick p-type μc-SiO$_x$:H contact layer a *FF* of 68.1% is achieved. From the first derivative of the *JV*-curve those "S"-shaped curves are made even more

apparent. Inflection points in the *JV*-curve are transformed to maxima, revealing a cutoff between low-ohmic contacts and non-linear contact resistances, see Figure 8.2.3. Moreover, the open circuit voltage V_{oc} of solar cells is also affected by the quality of the TCO/p contact. With a p-type µc-SiO$_x$:H layer (0.93 V) the V_{oc} is similar to solar cells with a p-type µc-Si:H contact layer. Solar cells without a contact layer show a lower V_{oc} of 0.90 V.
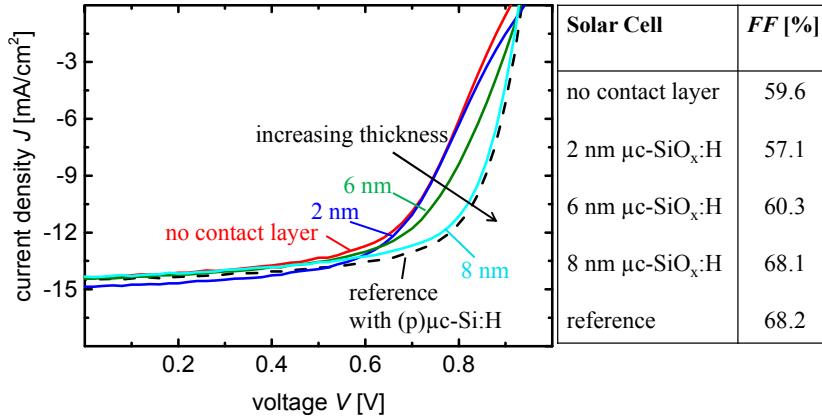

Solar Cell	FF [%]
no contact layer	59.6
2 nm µc-SiO$_x$:H	57.1
6 nm µc-SiO$_x$:H	60.3
8 nm µc-SiO$_x$:H	68.1
reference	68.2

Figure 8.2.2: *JV*-curves of a-Si:H solar cells under illumination with p-type µc-SiO$_x$:H contact layer of different thicknesses varying from 2 nm to 8 nm. For comparison an a-Si:H solar cell with p-type µc-Si:H contact layer (indicated as reference) and an a-Si:H solar cell without any additional contact layer (only p-type a-SiC:H) are shown.

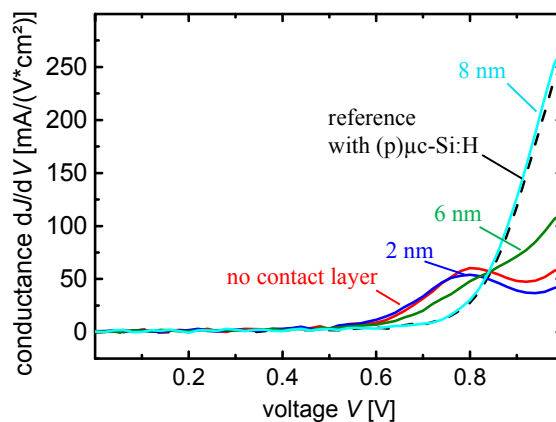Figure 8.2.3: First derivative of the *JV*-curve of a-Si:H solar cells under illumination with p-type µc-SiO$_x$:H contact layer of different thicknesses. The reference solar cells containing a p-type µc-Si:H contact layer is shown in black.

After finding of a suitable contact layer thickness parameter studies concerning the amount of TMB, used as a source for the p-type doping, are carried out. In Figure 8.2.4 the photovoltaic parameters (η, FF, V_{oc}, J_{sc}) of solar cells with p-type μc-SiO$_x$:H as window layer with TMB/SiH$_4$ ratio r_{TMB} varying from 0.0017 to 0.0052 are presented. The most pronounced effects are seen in terms of the fill factor. For the solar cell with a TMB/SiH$_4$-ratio of 0.0035 a maximum in FF was found. Also, the V_{oc} has a maximum at the same r_{TMB}. Both effects result in an efficiency improvement to 9.7% compared to the reference solar cell with 9.4%. Also, it is seen that J_{sc} decreases slightly with increasing r_{TMB}. It shows that r_{TMB} not only affects the doping level of the thin-film silicon, but also sensitively influences the electric properties of a solar cell when deposited on top of ZnO:Al.
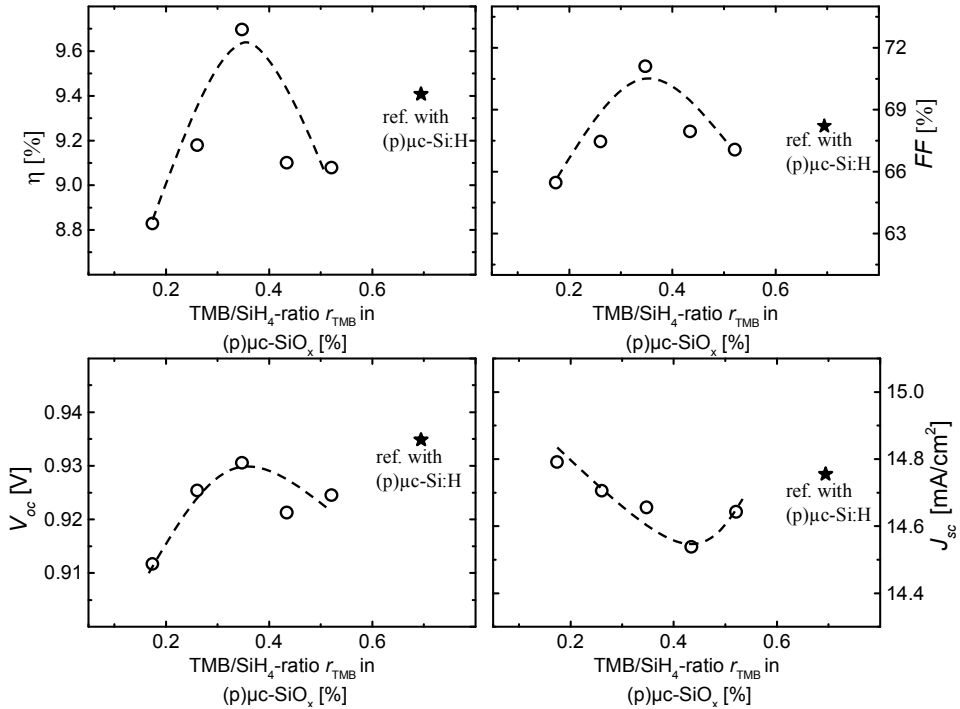

Figure 8.2.4: Conversion efficiency η, fill factor FF, open circuit voltage V_{oc} and short-circuit current density J_{sc} of a-Si:H solar cells containing a p-type μc-SiO$_x$:H contact layer with various TMB/SiH$_4$-ratios (r_{TMB}). The dashed lines are guides to the eye. The reference containing a p-type μc-Si:H layer is shown with a star symbol.

Finding optimal process parameters for a single layer is one approach to improve the electrical properties of a solar cell. Another strategy is the investigation of combinations of different p-layers. For example, p-layer stacks can be made of a-SiC:H, μc-Si:H or μc-SiO$_x$:H films. These layers have different properties with individual advantages and disadvantages. As an example p-type a-SiC:H has a relatively high transparency and provides a high V_{oc} for a-Si:H solar cells but when deposited on top of ZnO:Al a deterioration of the fill factor is seen. An additional p-type μc-Si:H layer between the ZnO:Al and the a-SiC:H layer can solve this problem, but that way rather large absorption losses are added to the system. The substitution of p-type μc-Si:H with more transparent p-type μc-SiO$_x$:H can reduce the optical loss (see Figure 6.1.6). Still, further improvements are possible. In Figure 8.2.5 four p-layer configurations sandwiched in between the TCO and the intrinsic layer of the solar cell are presented.

.

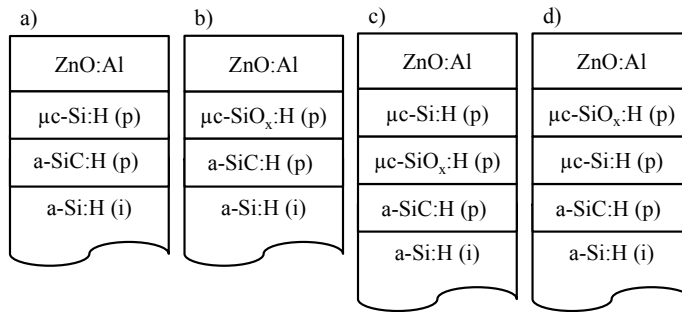| a)	b)	c)	d)
ZnO:Al	ZnO:Al	ZnO:Al	ZnO:Al
μc-Si:H (p)	μc-SiO$_x$:H (p)	μc-Si:H (p)	μc-SiO$_x$:H (p)
a-SiC:H (p)	a-SiC:H (p)	μc-SiO$_x$:H (p)	μc-Si:H (p)
a-Si:H (i)	a-Si:H (i)	a-SiC:H (p)	a-SiC:H (p)
		a-Si:H (i)	a-Si:H (i)

Figure 8.2.5: Schematic drawing of the TCO/p interface with different p-layer configurations for thin-film silicon a-Si:H solar cells. The p-layers consist of amorphous silicon carbide (a-SiC:H), microcrystalline silicon (μc-Si:H) or microcrystalline silicon oxide (μc-SiO$_x$:H).
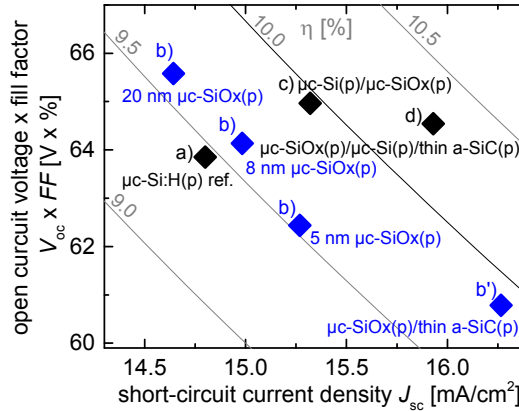
Figure 8.2.6: $V_{oc} \times FF$ versus J_{sc} diagram for a-Si:H solar cells with various p-layer configurations. All solar cells are deposited on top of single textured ZnO:Al and include a standard p-type a-SiC:H layer, if not described otherwise. Equi-conversion efficiency lines are displayed as diagonal lines.

Based on these four p-layer combinations solar cell results plotted in a $V_{oc} \times FF$ versus J_{sc} diagram are shown in Figure 8.2.6. This diagram provides an overview of the electrical properties as a function of the optical properties. Additionally, the equi-conversion efficiency lines are displayed as diagonals. Starting with the standard type consisting of a µc-Si:H and a-SiC:H p-layer (Figure 8.2.5 a)), moderate $V_{oc} \times FF$ values are achieved. A relatively low short-circuit current density (J_{sc} = 14.8 mA/cm²) is the disadvantage of that stack. By substitution of the µc-Si:H p-layer by a µc-SiO$_x$:H p-layer (Figure 8.2.5 b)) an improved J_{sc} was achieved with thin layers. While solar cells with a 5 nm and 8 nm thin µc-SiO$_x$:H layer exceed the J_{sc} of the reference a further increase leads to a lower J_{sc}. However, the $V_{oc} \times FF$ product improves with the enlargement of the layer thickness. All three cases showed an efficiency improvement compared to the solar cell with a reference µc-Si:H p-type layer. The highest value for $V_{oc} \times FF$ is obtained by a µc-Si:H/µc-SiO$_x$:H/a-SiC:H p-layer stack consisting of a thin µc-Si:H and a thin µc-SiO$_x$:H p-type layer (Figure 8.2.5 c)). Also J_{sc} is relatively high (15.3 mA/cm²) resulting in an improvement of the conversion efficiency to 9.95%. As an approach to increase the J_{sc} further, a thin µc-SiO$_x$:H p-layer was combined with a thin a-SiC:H p-type layer (half thickness of the standard). This is shown in point b'). Solar cells deposited with that configuration show the highest J_{sc} (>16.5 mA/cm²). A low V_{oc} however, result in the lowest value found for the $V_{oc} \times FF$ product and therefore, the conversion efficiency stagnates at 9.9%. Finally, a thin a-SiC:H p-type layer was applied in combination with a

µc-SiO$_x$:H and a µc-Si:H p-type layer (Figure 8.2.5 d)). All layers were kept thin resulting in a high J_{sc} of 16 mA/cm². Most importantly, solar cells with that layer stack show the highest $V_{oc} \times FF$ and a conversion efficiency of 10.3% was accomplished.

Discussion

In literature it is described that the formation of a Schottky barrier is induced through Fermi energy alignment and a related downward band bending at the ZnO:Al/(p) a-SiC:H interface [96]. Also, the down bending of energy bands is associated with the formation of a depletion layer at the interface increasing the electrical resistance. The introduction of a highly doped µc-Si:H layer as a contact layer is often applied to improve the contact resistance by narrowing the depletion zone [96][97]. A very plausible model is given by Ma et al. [95] who identifies the role of the contact layer by help of a band diagram shown in Figure 8.2.7. In that publication modifications of interface potentials by introduction of p-type µc-Si:H and µc-SiC:H are investigated. A Fermi level pinning effect induces the band bending at the TCO/p interface. That downward bended valence band now hinders the transport of holes which is quantified as a surface potential barrier $\Delta\Phi_p$. That way, a number of holes are forced to diffuse backwards leading to a reduction of charge carrier collection therefore, a reduction of the fill factor.
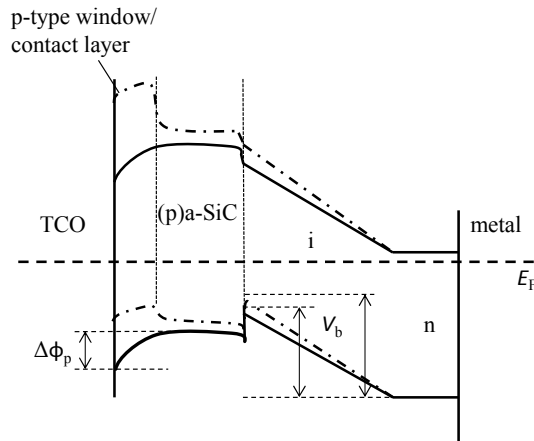

Figure 8.2.7: A schematic band diagram of an a-Si:H solar cell with a (p)a-SiC (solid lines) and p-type, wide bandgap contact layer (dashed lines) with emphasis of the TCO/p region. $\Delta\Phi_p$ is the surface potential barrier. V_b is the built in voltage. The band diagram is based on a publication on µc-SiC contact layers by Ma et al. [95].

By introducing a p-type µc-SiC:H layer with a hole concentration several orders of magnitude larger than in p-type a-SiC:H $\Delta\Phi_p$ is reduced. In the band diagram, this case is drawn as dashed-dotted lines. It is shown that the valence and the conduction band of the solar cells's p-side shift to higher energy levels. From measurements obtained by the transient photopotential method, where the solar cells contain different contact layer thicknesses, $\Delta\Phi_p$ decreased from 0.16 eV to 0.06 eV. At the same time, the built-in voltage V_b increases from 0.85 V to 1.05 V. Thus, a higher V_{oc} was achieved. The formation of a low-ohmic contact contributed to an improvement of the fill factor [95].

Compared to our systems, where p-type µc-Si:H or p-type µc-SiO$_x$:H are used as contact layers, similar effects are seen. The V_{oc} of 0.79 V for the case without a contact layer has been increased to 0.93 V when applying a contact layer. This can be attributed to an enlargement of the built-in voltage. Also, the *FF* is affected when varying the TMB flow that results in a shifting of the Fermi energy in the p-type layer, which affects the band bending at the TCO/p interface. Furthermore, the crystalline growth of µc-SiO$_x$:H is affected by the amount of TMB during the deposition which can also have an influence on the Fermi energy. The continuous improvement of the fill factor by increasing the layer thickness of p-type µc-SiO$_x$:H implies a reduction of the interfacial potential barrier $\Delta\Phi_p$.

8.3.   On the p/i Interface in a-Si:H Solar Cells

For the fabrication of highly efficient solar cells it is not only essential to provide an ohmic contact at the TCO/p interface. Moreover, it is crucial that the electrical losses which can occur at each interface are reduced to a minimum. Especially the p/i interface has been in the focus of investigations [102] - [105]. It is shown that electrical properties of solar cells could be improved by insertion of additional intrinsic buffer layers between the p-type and i-layer.

For the reduction of optical losses occurring at the p-type layer of thin-film silicon solar cells one attempt is to replace highly absorbing layers by more transparent layers. Like in the case of μc-Si:H solar cells the p-type μc-Si:H layer can be fully substituted by p-type μc-SiO$_x$:H leading to improvement of optical and electrical properties. However, this was not achieved for a-Si:H cells. When using a p-type μc-SiO$_x$:H layer without the a-SiC:H p-layer the V_{oc} was reduced to 790 mV. For enhancement of the V_{oc} different kinds of intrinsic buffer layers are investigated to improve the p/i-interface for a-Si:H solar cells with only a p-type μc-SiO$_x$:H layer.

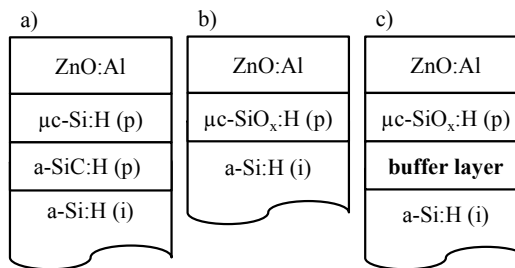| a)	b)	c)
ZnO:Al	ZnO:Al	ZnO:Al
μc-Si:H (p)	μc-SiO$_x$:H (p)	μc-SiO$_x$:H (p)
a-SiC:H (p)	a-Si:H (i)	**buffer layer**
a-Si:H (i)		a-Si:H (i)

Figure 8.3.1: Sketches of thin-film silicon a-Si:H solar cells including p-type layer stacks and buffer layers. a) A standard solar cell with a p-type μc-Si:H contact layer is used as a reference; b) only p-type μc-SiO$_x$:H is applied as a p-type layer; c) different intrinsic buffer layers are introduced between the p-type μc-SiO$_x$:H and i-layer. Those are: intrinsic a-SiO$_x$:H; intrinsic μc-Si:H; and intrinsic a-SiC:H layers.

In Figure 8.1.1 sketches of a-Si:H solar cells including different p-type layer stacks and buffer layers are shown. In Figure 8.3.2 the corresponding *JV*-curves of a-Si:H solar cells with a μc-SiO$_x$:H p-layer and various buffer layers intrinsic a-SiO$_x$:H, intrinsic μc-Si:H and intrinsic a-SiC:H H are shown.
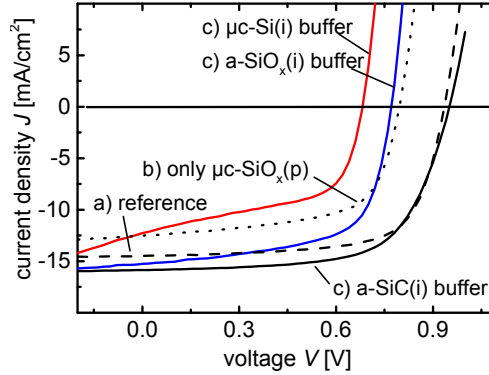
Figure 8.3.2: *JV*-curves of a-Si:H solar cells with a µc-SiO$_x$:H p-layer and various i-layers working as buffer layers ((i)a-SiO$_x$:H, (i)µc-Si:H and (i)a-SiC:H). A reference solar cell with a p-type µc-Si:H contact layer and an a-SiC:H p-layer is shown as a reference.

Table 8.3.1: Photovoltaic parameter of a-Si:H solar cells with a µc-SiO$_x$:H p-layer and various i-layers working as buffer layers ((i) a-SiO$_x$:H, (i) µc-Si:H and (i) a-SiC:H). A standard solar cell with a p-type µc-Si:H contact layer and an a-SiC:H p-layer is used as a reference.

buffer layer	η [%]	*FF* [%]	V_{oc} [mV]	J_{sc} [mA/cm^2]	R_s [Ω]
only µc-SiO$_x$(p)	7.1	64.4	790	14.0	4.5
+ a-SiO$_x$(i)	7.5	63.7	780	15.2	5.0
+ µc-Si(i)	4.7	56.4	685	12.2	5.1
+ a-SiC(i)	9.7	64.7	950	15.8	8
only a-SiC(p)	6.3	63.2	800	12.5	7
ref. with µc-Si(p)/a-SiC(p)	9.4	68.2	935	14.8	6.4

The photovoltaic parameters are presented in Table 8.3.1. A standard solar cell with an a-SiC:H p-layer with additional p-type µc-Si:H contact layer is presented as a reference. It shows a high V_{oc} amounting to 935 mV. When using only a µc-SiO$_x$:H p-type layer a decrease of the V_{oc} and the J_{sc} emerges. The V_{oc} is now only 790 mV. Comparing to that case an additional intrinsic µc-Si:H buffer layer after the µc-SiO$_x$:H p-type layer even decreases the V_{oc} further to 685 mV. Also the fill factor is reduced. An intrinsic a-SiO$_x$:H buffer layer improves the J_{sc} of the a-Si:H cell to 15.2 mA/cm² but also here, the V_{oc} is decreased to 780 mV. Anyhow, the implementation of an intrinsic a-SiC:H buffer layer pushes the V_{oc} of the a-Si:H solar cell to 950 mV. Also, higher J_{sc} of 15.8 mA/cm² was obtained and the conversion efficiency was improved to 9.7%, compared to the reference

(η = 9.3%). However, in the case of an additional a-SiC:H i-type buffer layer the fill factor is reduced to 64.7% which is linked to an increased series resistance.

Discussion

In Chapter 6 it is shown that the application of an p-type μc-SiO$_x$:H layer resulted in an improved V_{oc} in μc-Si:H solar cells. However, when using a p-type μc-SiO$_x$:H layer without the a-SiC:H p-layer in an a-Si:H solar cell the V_{oc} was reduced to 790 mV. This could be caused by an enhanced recombination of charge carriers at the p/i interface or an insufficient electric field. The insertion of various intrinsic buffer layers led to different V_{oc} values even though no changes were obtained concerning any doped layers. The insertion of an a-SiC:H buffer layer resulted in an improved V_{oc} to 950 mV. Therefore, it can be assumed that the reduction of the V_{oc} is caused by an enhanced recombination of charge carriers at the p/i interface. The low fill factor of 64.7% linked to the intrinsic a-SiC:H buffer layer shows that despite of the improvement of the V_{oc}, band offsets occurring at the p/i interface might still impair the conduction of charge carriers.

Intrinsic a-SiC:H layers already have been investigated in early years [105]. There, it is stated that wide gap materials are capable to block the back diffusion of electrons. Another publication reported on the improvement of V_{oc} for thin μc-Si:H solar cells by implementing an intrinsic μc-SiO$_x$:H buffer layer [102]. Here, it is specified that the limiting factor for thin-film solar cells is the recombination at the p/i- interface, while for thicker solar cells the quality of the bulk material becomes more relevant. From dark JV-measurements it is found that the buffer layer thickness had a positive effect on the reduction of shunt current density. That is explained by a reduced interface recombination which is linked to an improved V_{oc}. More recently, in reference [103] it is reported that efficiency improvements of a-Si:H and μc-Si:H solar cells were accomplished by inserting an additional buffer layer made of intrinsic μc-SiO$_x$:H. There, it was possible to improve V_{oc}, J_{sc} and FF. It is stated that inserting a buffer layer improves the bulk material quality by shunt quenching and inhibition of boron cross contamination from the p-type layer. More similar to our layer it is reported on the insertion of intrinsic a-SiO$_x$:H buffer layers between the p-type μc-SiO$_x$:H and intrinsic a-Si:H layer [104]. Beside an improvement of fill factor and J_{sc}, the V_{oc} could be increased from 825 mV to 910 mV.

This improvement is explained by the formation of a balance between the built-in voltage and interface recombination and is in agreement with findings obtained in this work.

The evaluation of our findings with published results in literature show rather large differences for comparable materials. Possibly the same material system are made by thin films that vary in terms of band position and thickness. Therefore, individual, sensitive parameter studies are required for finding optimal conditions for different PECVD systems. Generally, high potential is seen for conversion efficiencies improvements by optimization of the p/i interface.

8.4.   Impact of TCO front Side Texture on the V_{oc} of a-Si:H Solar Cells

Previous investigations of single- or multi-junction solar cell devices deposited on top of different TCO front textures pointed out differences in terms of electrical and optical properties. Regarding the short-circuit current density of a-Si:H solar cells high performances were achieved for type C (DT-ZnO:Al) and type G (SnO$_2$:F) front TCOs. This is driven by the, particularly for a-Si:H solar cells, highly suitable light scattering provided by its textures. Especially for type C ZnO:Al, which contains smaller and steeper crater structures in combination with an improved transparency, high conversion efficiencies of 11% initial were achieved for a-Si:H solar cells.

In this chapter the focus is on the electrical performance for solar cells deposited on various textures. Solar cells deposited on top of type C TCO show a reduced V_{oc} of approximately 30 mV. Also, when depositing solar cells on top of type G and type F (LPCVD ZnO:B) front textures a lower V_{oc} is measured comparing to flat textures. In literature it has been reported that a reduction of V_{oc}, especially for µc-Si:H solar cells, is caused by the formation of cracks occurring due to microcrystalline growth on very steep structures [106][107][108]. However, such cracks have not been observed for a-Si:H solar cells [109]. In this subchapter die origin of the V_{oc} dependency of a-Si:H solar cells on the front texture will be discussed.

Table 7.2.1: Overview of applied TCO front contacts, fabrication remarks and surface topography characteristics. (copy from Chapter 7 for the reader's convenience)

type	TCO material	Fabrication remark	ACL [nm]	σ_{RMS} [nm]	Mean angle [°]
A	ZnO:Al (1%)	Sputter; 35s HCl etched	715	110	23
B	ZnO:Al (1%)	Sputter; 20s HF / 10s HCl etched	470	80	25
C	ZnO:Al (0.5%)	Sputter; 90s HCl / 20s HF etched	380	70	27
D	ZnO:Al (0.5%)	Sputter; 90s HCl etched	855	125	24
E	ZnO:Al (0.5%)	Sputter; 120s HCl etched	1110	160	21
F	ZnO:B	LPCVD from EPFL	290	80	40
G	SnO$_2$:F	APCVD Asahi Glass Company	190	35	29
H	ZnO:Al (1%)	flat	5	5	-

The investigated front textures refer to Table 7.2.1 in Chapter 7 and include one additional front side TCO. The types of applied TCOs are: sputter-etched single-textured ZnO:Al with large and relatively flat crater-like features (type A). Type B, shows a slightly steeper and smaller crater-like structure compared to type A. Type C, is a sputter-etched double-textured ZnO:Al containing very steep sub-nanometer sized craters. Type F TCO is a ZnO:B deposited by low pressure chemical vapor deposition (LPCVD). Type G is SnO_2:F coated glass deposited by atmospheric pressure chemical vapor deposition (APCVD). Also, type G contains an additional thin ZnO:Al protection layer. Type H is a flat, as deposited sputtered ZnO:Al. The additional front TCO (marked as type HF ZnO) is a sputtered ZnO:Al(1%) and has been wet chemically etched for 20 s with hydrofluoric acid (HF). Similar to type C it contains very steep sub-nanometer sized craters.

Single junction a-Si:H solar cells with an i-layer thickness of 350 nm are deposited on top of various front textures. The solar cells contain a p-type µc-Si:H contact layer and an a-SiC:H p-layer. By AFM the topography of applied TCOs are measured for a size of 20×20 µm². The surface area of each texture has been calculated by AFM data and normalized to a flat surface. In Figure 8.4.1 the V_{oc} of solar cells deposited on various front textures is plotted versus the normalized solar cell surface area. The surface area of a type H is defined as 1 cm².
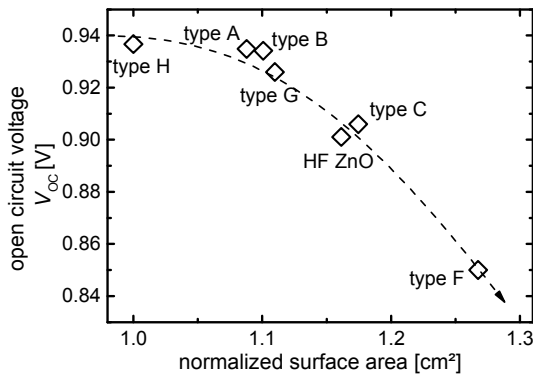

Figure 8.4.1: Open circuit voltage V_{oc} of a-Si:H solar cells as a function of the normalized surface area obtained by AFM measurement of different front TCOs. The surface area of a flat ZnO:Al is defined as 1 cm². The dashed line is a guide to the eye.

The highest V_{oc} is measured for a-Si:H solar cells deposited on type H, type A and type B and amounts to 935 mV. In the case of type G the V_{oc} is slightly reduced. For solar cells deposited on HF ZnO as well as for type C a decrease of the V_{oc} by 30 mV occurs. For type F the drop is almost 90 mV. The figure reveals that with a larger surface area the V_{oc} decreases continuously. A possible explanation for that coherence is an enhanced surface recombination through the larger interface area.

To investigate whether the V_{oc} drop is only driven by the enlarged surface area or also by an enhanced bulk recombination, an additional series of solar cells was fabricated containing various i-layer thicknesses. The a-Si:H cells containing the same standard p- and n-type layers were deposited with 100 nm; 200 nm; 300 nm and 400 nm thick i-layers. The applied front textures are type A; C; F; G; H and HF ZnO.
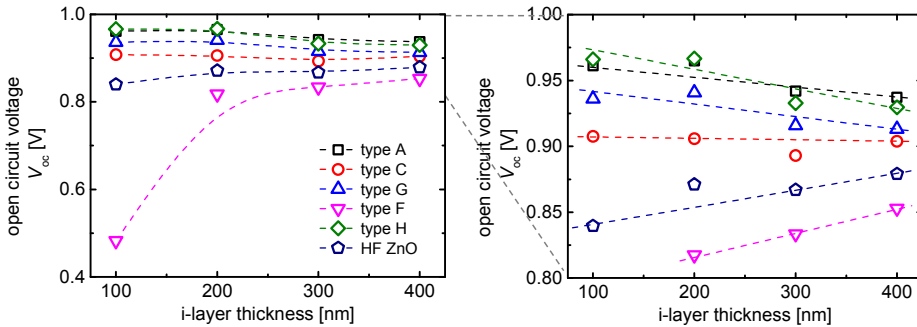

Figure 8.4.2: Open circuit voltage V_{oc} of a-Si:H cells as a function of i-layer thickness. The applied front textures are type A (HCl etched ZnO:Al); type C (double-textured ZnO:Al); type F (LPCVD ZnO:B); type G (APCVD SnO$_2$:F) ; H (flat ZnO:Al) and HF etched ZnO:Al. The right figure is a magnified section for a V_{oc} range between 0.8 V and 1.0 V.

In Figure 8.4.2 the V_{oc} of a-Si:H cells are shown as a function of the i-layer thickness. For the solar cells deposited on top of the front texture type A, G and H a continuous reduction of the open circuit voltage with increasing i-layer thickness is seen. The V_{oc} of solar cells deposited on type C TCO remains almost constant for different thicknesses. For HF ZnO and especially for type F front texture an increase of the V_{oc} is observed. The most pronounced difference occurs between solar cells with an i-layer thickness of 100 nm and 200 nm. The increase in the case of HF ZnO amounts to 40 mV and in the case of type F TCO to more than 330 mV.
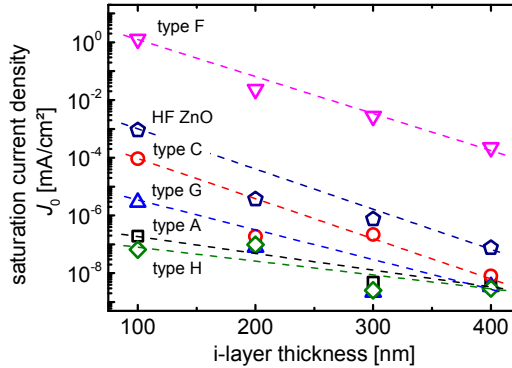
Figure 8.4.3: Reverse bias saturation current density J_0 of a-Si:H cells as a function of i-layer thickness plotted in an logarithmic scale. The applied front textures are type A (HCl etched ZnO:Al); type C (double-textured ZnO:Al); type F (LPCVD ZnO:B); type G (APCVD SnO$_2$:F) ; type H (flat ZnO:Al) and HF etched ZnO:Al.

In Figure 8.4.3 reverse bias saturation current density J_0 of a-Si:H cells deposited on various front textures plotted in an logarithmic scale are shown as a function of i-layer thickness. It is seen that with increasing i-layer thickness J_0 of all samples decreases. The differences in J_0 between thin and thick i-layer for a-Si:H solar cells are up to four orders of magnitude large. The high saturation current density of over 1 mA/cm² for 100 nm thick solar cells deposited on type F TCO implies a bad quality diode with a low parallel resistance. The difference between 100 nm thick and 200 nm thick i-layers in terms of J_0 are extraordinary large for solar cells deposited on type F, C and HF ZnO:Al and amount to two orders of magnitude. Contrarily, the difference seen for solar cells deposited on top of flat ZnO:Al is only 3×10^{-8} mA/cm². Even for 400 nm thick solar cells deposited on type F the saturation current density is several orders of magnitude larger than in the case of flatter textures. For type A, C, G and H TCOs the saturation current of 400 nm thick solar cells remain in the range of 10^{-9} mA/cm² and thus, implies a high quality diode. In the case of type G TCO consisting of small pyramids with a σ_{RMS} of 35 nm the reverse bias saturation current density is comparably high ($\sim 10^{-6}$ mA/cm²) for very thin i-layers. However, when increasing the thickness to 200 nm J_0 decreases to the order of 10^{-8} mA/cm². The minor difference to solar cells deposited on flat or single textured ZnO:Al has been equalized within only one step of i-layer thickness expansion from 100 nm to 200 nm.

Discussion

In this chapter it is seen that deterioration of the V_{oc} occurs when solar cells are deposited on very rough front contacts. The V_{oc} however, improves with increasing i-layer thickness for these samples. The low V_{oc} can be explained by the formation of nano-cracks or defective regions during the deposition on top a front texture with very steep features. The cracks which go through the entire i-layer provide a number of nano-shunts and therefore, reduce the V_{oc}. Solar cells which were deposited on top of flat front contacts show a decreasing V_{oc} with increasing i-layer thickness. It can be assumed that here only a small number of cracks and shunts are formed during the a-Si:H. This suggests on the other hand that for a solar cell deposited on rough type F TCO the steep features induces the formation of nano-cracks. Those are especially are present within first 100 nm - 200 nm of the i-layer. A large fraction of the cracks are then healed with the deposition of thicker i-layers reducing the shunting effect. In this case the V_{oc} also increases with increasing i-layer thickness. This effect is linked to a broadening of the depletion region occurring with an enlargement of the i-layer thickness, as for p-i-n solar cells the i-layer represents the depletion area. Therefore, the reduction of the saturation current density by increasing the i-layer thickness is seen. But still, bulk material containing defective regions within the first 200 nm leads to higher reverse bias saturation current density J_0 and also lower V_{oc}. In a-Si:H solar cells with thick i-layers the negative impact of the rough front contact and the enhanced shunting in the defective first 200 nm becomes less significant and the reduction of the V_{oc} will be dominated by an surface area related surface recombination. Thus, a correlation between the solar cell surface area and V_{oc} is seen (Figure 8.4.1).

Comparable results are reported in the literature for microcrystalline thin-film solar cells, where crack formation is more evident. Python et al. [106] discussed findings regarding the relation between surface textures and electrical properties on µc-Si:H solar cells using TEM images to quantify the crack density. Also, they reported on an equivalent circuit model by addition of a second diode to describe cracks as "non-linear shunts", as shown in Figure 8.4.4. By variable illuminated measurements and dark JV-measurements it was publicized that cracks counted by TEM images do not behave like ohmic parallel shunt resistance. They rather show a non-linear behavior and have to be modeled as diode-like shunts [106].
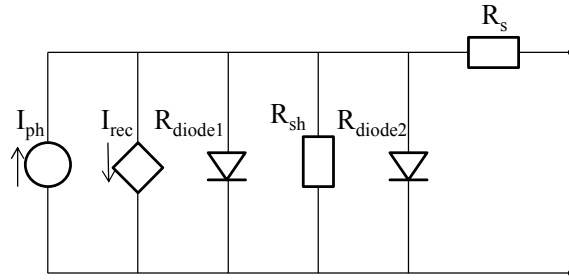
Figure 8.4.4: Equivalent circuit for µc-Si:H solar cells containing nano-shunts (cracks). Photo current I_{ph}; recombination current I_{rec}; shunt resistance R_{sh}; non-linear resistance related to nano-shunts R_{diode}; series resistance R_s as components in an equivalent circuit [106].

In that publication, solar cell results show a linear reduction of the V_{oc} with increasing crack density. The reversed saturation current density J_{02} calculated from this model (R_{diode2}) show a correlation to the crack density of the bulk material. Also, J_{02} is strongly dependent on the crack length to i-layer thickness ratio. When the length was only one third of the i-layer thickness, much lower reversed saturation currents where measured [106]. Those findings would confirm our interpretations, where it is stated that nano-cracks occur within the 100 nm to 200 nm are responsible for the deterioration of the V_{oc}.

8.5.   Conclusion

The formation of an "S" -shaped JV-curve seen in Chapter 8.2 is attributed to the Schottky barrier at the TCO/p- interface. The extent of the band bending and therefore, the height of the potential barrier is a function of the doping of the TCO and p-type layer and thus, related to the work function. By introducing of a p-type µc-Si:H or a p-type µc-SiO$_x$:H contact layer the potential barrier is reduced leading to an improved fill factor. A series of solar cells where the TMB/SiH$_4$-ratio r_{TMB} for the p-type µc-SiO$_x$:H layer was varied in small ranges (Figure 8.2.4) revealing a sensitive interaction between electrical properties of a solar cell and the doping of a µc-SiO$_x$:H p-type contact layer. There, it is shown that the optimum for the TMB/SiH$_4$-ratio resulted in an improvement of fill factor and therefore, in an improvement of the conversion efficiency. This study reveals the complexity of the subject. From another series it was found that not only the composition of process gases but also the thickness of the p-type µc-SiO$_x$:H affects the FF strongly, as shown in Figure 8.2.2. From the results it is seen that a certain thickness is essential for a low resistive ohmic contact between ZnO:Al and the p-type layer. Thicker layers cause additional absorptions and with that lower short-circuit current densities. In Figure 8.2.6, where $V_{oc} \times FF$ is plotted as a function of J_{sc}, a tradeoff between optical and electrical properties caused by various p-type layer stacks are shown. Besides, it reveals that a combined use of a (p)µc-SiO$_x$:H/(p)µc-Si:H/(p)a-SiC:H thin layer stack can improve the V_{oc} and FF significantly while maintaining a high transparency. That way, potential barriers arising between the p-type µc-SiO$_x$:H and p-type a-SiC:H layer can be reduced by the inset of an additional p-type µc-Si:H layer.

In Chapter 8.3 the impact of various intrinsic buffer layers between the p- and i-layer of a-Si:H solar cells on the electrical properties are investigated. Different buffer layers (intrinsic a-SiO$_x$:H, intrinsic µc-Si:H and intrinsic a-SiC:H) are applied at the (p)µc-SiO$_x$:H/(i)a-Si:H interface. In the case of intrinsic a-SiO$_x$:H and intrinsic µc-Si:H buffer layers a reduction of V_{oc} and J_{sc} is seen. An intrinsic a-SiC:H buffer layer could improve the V_{oc} to 950 mV and the J_{sc} to 15.8 mA/cm² resulting in an conversion efficiency improvement to 9.7%, compared to the reference with V_{oc} = 935 mV, J_{sc} = 14.8 mA/cm² and η = 9.4%. However, the fill factor was reduced from 68.2% to 64.7%. As an outlook, in order to minimize the fill factor loss, further parameter studies are required. A detailed investigation of various band structures would also be beneficial for

the design of an optimized p/i-interface. That way, a targeted band-engineering for development and fabrication of low-loss interfaces would be made possible.

In Chapter 8.4 it was observed that defective areas (nano-cracks) occur in amorphous silicon thin-film solar cells when deposited on top of very rough textures with steep features. Especially for very thin i-layers (< 200 nm) the impact on the electrical performance is large. However, by enlarging the i-layer thickness an increasing number of nano-cracks are healed out during the slow growing process of the a-Si:H layer. Therefore, the shunting effects are also reduced. It can be concluded that for solar cells deposited on very rough substrates nano-shunts and an enhanced bulk recombination are responsible for the reduction of V_{oc}. This is especially the case when the solar cell is thin and the nano-cracks pass through the entire i-layer. Surprisingly, when applying thick absorber layers the bulk effect becomes less dominant. This is caused by a changed proportion between defect rich and defect poor i-layers. In that case the effect of a surface area related recombination becomes dominant, as shown in Figure 8.4.1.

Chapter 9
Summary

The objective of this dissertation was to develop and characterize n- and p-type hydrogenated microcrystalline silicon oxides for thin-film silicon solar cell applications. Implemented at different positions in a solar cell those layers fulfill several functions at which approaches for conversion efficiency improvements are set up. The goal of this thesis was to find optima for optical and electrical material characteristics for different applications and to contribute to deeper insights of various aspects of a solar cell. This can be on the interplay between different layers in a solar cell or the interaction between topography and light management or electrical performance. In the following chapter the main findings are summarized.

n- and p-type μc-SiO_x:H

In Chapter 5 material characteristics like electrical conductivity, Raman crystallinity, optical band gap and refractive index of n- and p-type μc-SiO_x:H were studied. Also, the interplay between those different features by using different deposition parameters was discussed. In this work it is shown that n-type μc-SiO_x:H thin films with a conductivity of 10^{-2} S/cm and a crystalline volume fraction of 55% can be achieved by adjusting the SiH_4/H_2- and the CO_2/SiH_4-ratio. Also, the energy band gap was modified from 2.1 eV to 2.7 eV. Correspondently, the refractive index was reduced from 3.3 to 1.8. It is seen that the decrease of the SiH_4/H_2-ratio results in a shift to higher electrical conductivity, larger band gap and smaller refractive index. It was possible to obtain the conductivity at a solar grade level while keeping a high CO_2/SiH_4-ratio resulting in optically superior material. This was achieved by a high H_2-dilution.

Also for p-type μc-SiO_x:H layers adequate electrical properties were implemented with a conductivity up to more than 10^{-2} S/cm and a Raman crystallinity of over 60%. The optical properties of p-type μc-SiO_x:H were tuned over a broad range. Films with an E_{04} from 2.1 eV to 2.8 eV and $n_{1000\ nm}$ from 2.6 to 1.6 by adapting CO_2/SiH_4-ratio were fabricated. When optical properties are improved it is seen that the electrical conductivity declines. A trade-off between electrical and optical properties becomes apparent. Therefore, CO_2/SiH_4-ratio has to be adjusted carefully. It was shown that for p-type μc-SiO_x:H, prepared in this work, a CO_2/SiH_4-ratio of maximum 2.4 is crucial for applications in a solar cell. From RBS measurements it was shown that solar grade material have an oxygen/silane ratio $r_{O,RBS}$ of maximum 50%. By increasing the oxygen content in μc-SiO_x:H layers it is seen that the crystallinity is reduced. Also, an increase of the TMB amount resulted in a decrease of the crystallinity. This also sensitively affects the electrical conductivity since the crystalline fractions form highly doped and more conductive material. Therefore, an optimized amount of TMB/SiH_4-ratio is essential to provide a good fill factor. Finally, it was shown that the amount of oxygen that is bound into the matrix is highly dependent on the applied power density. Deposition parameters as pressure and temperature do not show large effects on the optical properties of the thin films, but can modify the crystalline growth behavior.

In this chapter it is presented that doped hydrogenated microcrystalline silicon oxide layers have versatile material properties. The multiplicity of process parameters like gas composition, power density, pressure, and temperature make the development and optimization a challenging task. The interplay between the intrinsic absorber layers and the doped μc-SiO_x:H layers is complex and individual for different PECVD systems. Moreover, deposition processes must be adapted to the applied transparent conductive oxides separately.

Window layers made of p-type μc-SiO_x:H

In Chapter 6 results on the newly developed p-type hydrogenated microcrystalline silicon oxide (μc-SiO_x:H) applied as a window layer in a-Si:H and μc-Si:H single junction solar cells are shown. A reduced parasitic absorption in the p-type layer was implemented by the replacement of the p-type μc-Si:H contact layer by a p-type μc-SiO_x:H layer. That way, a conversion efficiency improvement of a-Si:H solar cells from 9.4% to 9.6% was achieved driven by a higher fill factor and an enhancement in the blue response. The reduction of the p-type a-SiC:H layer thickness resulted in a further

improvement of the short-circuit current density and thus, conversion efficiency improvement to 10.3%. However, the p-type layer could not be fully substituted by p-type µc-SiO$_x$:H in the case of a-Si:H solar cells and was associated with a clear decrease of the open circuit voltage.

In the case of µc-Si:H solar cells the µc-Si:H p-type layer could be replaced by a p-type µc-SiO$_x$:H layer. This resulted in a clear improvement of the short-circuit current density from 23 mA/cm² to >25 mA/cm². Also, the V_{oc} was improved from 510 mV to 530 mV. The increase of the open circuit voltage is linked to a decrease of the crystalline volume fraction of the first few hundred nanometers of the intrinsic material which was also shown by an in-situ Raman measurement method. This resulted in an improvement of the conversion efficiency of µc-Si:H solar cells from 8.4% to 9.5% by a substitution of the standard µc-Si:H p-type layer by a p-type µc-SiO$_x$:H. After SiH$_4$/H$_2$-ratio and layer thickness of the intrinsic absorber layer were optimized the conversion efficiencies of µc-Si:H solar cells with a p-type µc-SiO$_x$:H layer were further improved resulting in a µc-Si:H solar cell with an η = 10.42%, J_{sc} = 25.35 mA/cm², V_{oc} = 568 mV and FF = 71.6%.

Intermediate reflector layers made of doped µc-SiO$_x$:H

n-type and p-type µc-SiO$_x$:H layers were successfully applied as intermediate reflector layers in a-Si:H/µc-Si:H tandem solar cells. IRLs made of n-type material with various layer thicknesses and refractive indices were investigated. A conversion efficiency improvement from 12.0% to 12.3% was achieved due to current matching. From *EQE* measurements it was seen that with lower refractive index and thicker layers the amount of light that is reflected back into the top cell was increased. With n = 1.9 the short-circuit current density could be improved by 1.2 mA/cm². The V_{oc} however, was not significantly affected by an additional interlayer. Similar trends for IRL with different thicknesses were also implemented with p-type µc-SiO$_x$:H.

Back reflectors with n-type μc-SiO$_x$:H

A third type of application of doped μc-SiO$_x$:H layers is to use it as part of a back reflector. In this Chapter 6.3 it was shown that the n-type μc-SiO$_x$:H/Ag reflector resulted in an improved optical performance of single junction and tandem solar cells. The improvements are caused by an enhanced red response in comparison with a-Si:H/Ag or μc-Si:H/Ag back reflectors. Similar to the application of ZnO/Ag back reflectors the improvements are explained by a reduction of plasmonic losses at the metal surface. The short-circuit current density of a-Si:H and tandem solar cells with an n-type μc-SiO$_x$:H/Ag back reflector surpassed the short-circuit current density of solar cells with the state-of-the-art back reflector. Tandem solar cells with an n-type μc-SiO$_x$:H/Ag back reflector show a similar conversion efficiency as compared to the state-of-the-art n-type a-Si:H/ZnO/Ag back reflector. Most importantly, the results show that a μc-SiO$_x$:H/Ag layer stack used as a back reflector makes it possible to cut the ZnO deposition step in the manufacturing process.

Interplay between topography and IRL performance

In Chapter 7 the interplay between various front side topographies and the effectiveness of the intermediate reflector layer in tandem solar cells were investigated. The effectiveness of IRL consider the top cell short-circuit current density improvement and the short-circuit current density loss in the bottom cell when comparing tandem solar cells with and without an IRL. The experimental results show that high efficiencies were achieved with front textures with a lateral feature size between 200 nm and 500 nm. The highest IRL effectiveness was seen for double-textured ZnO:Al front contact. This front texture consists of a mixture of large and small craters. The improved effectiveness is attributed to the small craters that are also steeper as compared to single textured ZnO:Al. The top cell short-circuit current density improvement is a result of enhanced light trapping between IRL and front texture. This is dependent on the amount of light scattered into large angles. The short-circuit current density loss in the bottom cell is linked to the amount of light that is reflected from the IRL out of the solar cell and therefore, kept away from the bottom solar cell. The comparison of the cell reflection between tandem cells deposited on different front textures with and without an IRL reveals this effect. It is shown that steeper structures are preferred in terms of light management for both sub-cells.

By use of rigorous optical simulations by FDTD method it was possible to generate and reproduce the *EQE*s of tandem devices applied on different front textures. This method renders possible the investigation of modified textures to overcome experimental limitations. The effect of reduction of solar cell reflection by increasing the steepness of the texture has been verified by simulations.

Electrical issues at the TCO/p and p/i-interface

In Chapter 8 approaches to overcome electrical losses occurring at the TCO/p and p/i-interface are discussed. From literature it is known that a downward band bending at the ZnO:Al/(p)a-SiC:H interface causes the formation of a Schottky barrier. The height of the potential barrier is dependent on the TCO material and also on the doping level of the p-type layer. Electrical losses at the TCO/p interface are determined as electrical resistance.

A series of a-Si:H solar cells was fabricated and the dopant of the p-type μc-SiO$_x$:H contact layer was varied in small steps. A sensitive interaction between electrical properties of a solar cell and the TMB/SiH$_4$-ratio of the contact layer was seen. The change in the *FF* was attributed to the band bending at the TCO/p interface. In another series it was seen that also the thickness of the p-type μc-SiO$_x$:H layer affects the *FF* in a strong way. It was shown that a certain thickness is essential to provide a low-ohmic contact between ZnO:Al and the p-type layer. However, thicker p-type layers cause additional absorptions and therefore, a reduction of the short-circuit current density. A tradeoff between optical and electrical properties becomes apparent. Further, an application of combined different p-type layer stack resulted in an improvement of V_{oc} and *FF* of a-Si:H solar cells. In combination of a high J_{sc} the a-Si:H solar cell showed a conversion efficiency improvement to 10.3%.

Next, the impact on electrical properties of a-Si:H solar cells by the application of various intrinsic buffer layers between the p- and i-layer were investigated. Intrinsic a-SiO$_x$:H, intrinsic μc-Si:H and intrinsic a-SiC:H buffer layers are applied between the interface between a μc-SiO$_x$:H p-layer and the a-Si:H i-layer to study the electrical impact on the p/i-interface. In the case of intrinsic a-SiO$_x$:H and intrinsic μc-Si:H buffer layers a reduction of V_{oc} and J_{sc} was observed. However, with an additional intrinsic a-SiC:H buffer layer a-Si:H solar cells showed an improvement of the V_{oc} to 950 mV resulting in an conversion efficiency of 9.7%.

TCO front texture on the V_{oc}

In Chapter 8.4 it was found that defective regions occur in amorphous silicon thin-film solar cells when deposited on very rough front textures. Especially for very thin i-layers (< 200 nm) the electrical deterioration was clear. When increasing the i-layer thickness it was seen that the nano-cracks in the absorber layer partially heal. Still, the bulk material include defective areas within the first 200 nm leading to higher reverse bias saturation current density J_0 and also a lower V_{oc}. In a-Si:H solar cells with thicker i-layers the negative impact of the rough front contact becomes less insignificant. Here, the reduction of the V_{oc} will be dominated by the surface recombination and a correlation between the solar cell surface area and reduced V_{oc} is seen.

To conclude, in this work improvements of conversion efficiencies of single- and multi-junction solar cells due to application of doped µc-SiO$_x$:H were realized. By using p-type µc-SiO$_x$:H window layers the external quantum efficiency was clearly enhanced. Also, it was shown that it is possible to obtain high quality contact layers between the TCO and p-type layer while improving the transparency. Moreover, deeper understanding on the optical and electrical loss mechanisms in thin-film silicon solar cells by the efficient usage of solar cell textures has been obtained. From experiments and simulations the impact of structure type and feature size on the enhancement of top cell current density and of current density loss in the bottom solar cell after implementation of an IRL in a tandem solar cell are investigated. Especially the steepness of the texture shows large effects on the utilization of incident light. On the other hand, very rough morphologies can worsen the electrical properties of a solar cell and a trade-off between electric and optical properties has to be taken in account.

Superior materials, advanced solar cell design and the usage of suitable topography can contribute to the realization of optically as well as electrically high performing and cost-effective thin-film silicon solar cells.

References

[1]   D.E. Carlson, and C.R. Wronski, "Amorphous Silicon Solar Cells", Appl. Phys. Lett. 28, pp. 671-673, 1976.

[2]   S. Guha, J.S. Payson, S.C. Agarwal, S.R. Ovshinsky, "Fluorinated amorphous silicon-germanium alloys deposited from disilane-germane mixture", Journal of Non-Crystalline Solids, vol. 97-98, pp. 1455 - 1458, 1987.

[3]   J. Meier, S. Dubail, R. Fluckiger, D. Fischer, H. Keppner and A. Shah, "Intrinsic microcrystalline silicon (μc-Si:H) - a promising new thin film solar cell material," 1st IEEE World Conference on Photovoltaic Energy Conversion (WCPEC), 1994.

[4]   J. Meier, S. Dubail, J. Cuperus, U. Kroll, R. Platz, P. Torres, J. Anna Selvan, P. Pernet, N. Beck, N. Pellaton Vaucher, C. Hof, D. Fischer, H. Keppner, A. Shah, "Recent progress in micromorph solar cells," Journal of Non-Crystalline Solids, vol. 227-230, pp. 1250 – 1256, 1998.

[5]   H. Tan, P. Babal, M. Zeman, A. H. Smets, "Wide bandgap p-type nanocrystalline silicon oxide as window layer for high performance thin-film silicon multi-junction solar cells," Solar Energy Materials and Solar Cells, vol. 132, pp. 597–605, 2015

[6]   D. L. Staebler, C. R. Wronski, "Reversible conductivity changes in discharge-produced amorphous Si," Applied Physics Letters, vol. 31, pp. 292-294, 1977.

[7]   P. Buehlmann, J. Bailat, D. Dominé, A. Billet, F. Meillaud, A. Feltrin, C. Ballif, "In situ silicon oxide based intermediate reflector for thin-film silicon micromorph solar cells," Appl. Phys. Lett., vol. 91, p. 143505, 2007.

[8]   R.E.I. Schropp, M. Zeman, "Amorphous and Microcrystalline Silicon Solar Cells: Modeling, Materials and Device Technology," Springer, Vol. 5, 1998.

[9]   P. Chabert and N. Braithwaite, "Physics of Radio-Frequency Plasmas" Cambridge University Press, 2011.

[10]   Reprinted from Publication A. Matsuda , M. Takai , T. Nishimoto, M. Kondo, "Control of plasma chemistry for preparing highly stabilized amorphous silicon at high growth rate," Solar Energy Materials and Solar Cells, Volume 78, pp. 3 – 26, 2003, with permission from Elsevier.

[11]   T. Tiedje, J. D. Joannopoulos, G. Lucovsky, "The Physics of Hydrogenated Amorphous Silicon II," Topics in Applied Physics, vol. 56, 1984.

[12]   X. Deng, and E.A. Schiff, "Handbook of photovoltaic science and engineering," John Wiley & Sons Chap. 12: Amorphous silicon-based solar cells, pp. 505 – 560, 2002.

[13]   N. Mott, "Conduction in Non-Crystalline Materials," Oxford University Press, Oxford, 1987.

[14]   R. A. Street, "Hydrogenated Amorphous Silicon," Cambridge University Press, Cambridge, 1991.

[15]   L. Houben, "Plasmaabscheidung von mikrokristallinem Silizium: Merkmale der Mikrostruktur und deren Deutung im Sinne von Wachstumsvorgängen, " Dissertation, Heinrich-Heine-Universität Düsseldorf, 1998.

[16]   L. Houben, M. Luysberg, P. Hapke, R. Carius, F. Finger, H. Wagner, "Structural properties of microcrystalline silicon in the transition from highly crystalline to amorphous growth," Philosophical Magazine A, vol. 77, pp. 1447 - 1460, 1998.

[17]   Reprinted from Publication O. Vetterl, F. Finger, R. Carius, P. Hapke, L. Houben, O. Kluth, A. Lambertz, A. Mück, B. Rech, H. Wagner, "Intrinsic microcrystalline silicon: A new material for photovoltaics," Solar Energy Materials and Solar Cells, vol. 62, pp. 97 - 108, 2000, with permission from Elsevier.

[18]   C. G. V. de Walle and R. A. Street, "Silicon-hydrogen bonding and hydrogen diffusion in amorphous silicon," Phys. Rev. B, vol. 51, pp. 10615 - 10618, 1995.

[19]   H. Branz, "Hydrogen collition model: Quantitative description of metastability in amorphous silicon," Phys. Rev. B, vol. 59, pp. 5498 - 5512, 1999.

[20]   S. Guha, in R.A. Street (Ed.), "Technology and Applications of Amorphous Silicon - Chap. Multijunction Solar Cells and Modules," Springer Series in Materials Science Volume 37, pp. 252 - 305, 2000.

[21]   S. M. Sze, K. Ng. Kwok, "Physics of Semiconductor Devices," Wiley & Sons, 3rd edition, 2006.

[22]   M. Hack, M. Shur, "Physics of amorphous silicon alloy p-i-n solar cells," Journal of Applied Physics, vol. 58, pp. 997 - 1020, 1985.

[23]   T. Tiedje, B. Abeles, D. L. Morel, T. D. Moustakas, C. R. Wronski, "Electron drift mobility in hydrogenated a-Si," Applied Physics Letters, vol. 36, pp. 695 - 697, 1980.

[24]   J. Liang, E. A. Schiff, S. Guha, B. Yan, J. Yang, "Hole-mobility limit of amorphous silicon solar cells," Applied Physics Letters, vol. 88, p. 063512, 2006.

[25]   T. Dylla, S. Reynolds, R. Carius, F. Finger, "Electron and hole transport in microcrystalline silicon solar cells studied by time-of-flight photocurrent spectroscopy," Journal of Non-Crystalline Solids, vol. 352, pp. 1093–1096, 2006.

[26]   J. P. Zheng, H. S. Kwok, "Low resistivity indium tin oxide films by pulsed laser deposition," Applied Physics Letters, vol. 63, pp. 1 - 3, 1993.

[27]   Asahi Glass Co., Ltd. Tco coated glass for thin film application (a-si/μcsi. http://www.agc-solar.com/glass-products/coated-glass/tco/tco-vu.html#uid_11_tech, accessed 19 March 2015.

[28]   N. Taneda, K. Masumoa, M. Kambe, T. Oyama, and K. Sato, "Highly Textured SnO_2 Films for a-Si/μc-Si Tandem Solar Cells," 23rd European Photovoltaic Solar Energy Conference and Exhibition, pp. 2084 - 2087, Valencia, Spain, 2008.

[29]   O. Kluth; B. Rech; L. Houben; S. Wieder; G. Schöpe; C. Beneking, "Texture etched ZnO:Al coated glass substrates for silicon based thin film solar cells," Thin Solid Films, vol. 351, pp. 247 - 253, 1999.

[30]   S. Faÿ, L. Feitknecht, R. Schlüchter, U. Kroll, E. Vallat-Sauvain, A. Shah, "Rough ZnO layers by LP-CVD process and their effect in improving performances of amorphous and microcrystalline silicon solar cells," Solar Energy Materials and Solar Cells, vol. 90, pp. 2960 - 2967, 2006.

[31]   E. Yablonovitch, "Statistical ray optics," J. Opt. Soc. Am. 72, pp. 899- 907,1982.

[32] H. W. Deckman, C. R. Wronski, H. Witzke, and E. Yablonovitch, "Optically enhanced amorphous silicon solar cells," Applied Physics Letters, vol. 42, pp. 968 - 970, 1983.

[33] B. Rech, H. Wagner, "Potential of amorphous silicon for solar cells," Applied Physics A: Materials Science & Processing, vol. 69, pp. 155 - 167, 1999.

[34] M. Berginski, J. Hüpkes, M. Schulte, G. Schöpe, H. Stiebig, B. Rech, M. Wuttig, "The effect of front ZnO:Al surface texture and optical transparency on efficient light trapping in silicon thin-film solar cells," J. Appl. Phys., vol. 101, p. 74903, 2007.

[35] T. Repmann, "Stapelsolarzellen aus amorphem und mikrokristallinem Silizium", Berichte des Forschungszentrums Jülich, 4082, Dissertation RWTH Aachen, 2003.

[36] B. Rech, T. Roschek, T. Repmann, J. Müller, R. Schmitz, and W. Appenzeller, "Microcrystalline silicon for large area thin film solar cells," Thin Solid Films, vol. 427, pp. 157 - 165, 2003.

[37] J. I. Owen, J. Hüpkes, H. Zhu, E. Bunte, S. E. Pust, "Novel etch process to tune crater size on magnetron sputtered ZnO:Al," phys. stat. sol. (a), vol. 208, pp. 109 - 113, 2011.

[38] S. Haas, A. Gordijn, H. Stiebig, "High speed laser processing for monolithical series connection of silicon thin-film modules", Progress in Photovoltaics: Research and Applications, vol. 16, pp. 195 - 203, 2008.

[39] S. Wemple, M. DiDomenico, "Behavior of the Electronic Dielectric Constant in Covalent and Ionic Materials", Phys. Rev. B, vol. 3, pp. 1338 - 1351, 1971.

[40] S. Wemple , "Refractive Index Behavior of Amorphous Semiconductors and Glasses", Phys. Rev. B, vol .7, pp. 3767 - 3777, 1973.

[41] W. B. Jackson, N. M. Amer, A. C. Boccara, D. Fournier, "Photothermal deflection spectroscopy and detection," Applied Optics, vol. 20, pp. 1333 - 1344, 1981.

[42] N. Höhne, "PDS als Charakterisierungsmethode für Dünnschichtsolarzellen aus amorphem Silizium." Diplomarbeit, RWTH Aachen, 1997.

[43] B. Holländer, H. Heer, M. Wagener, H. Halling, S. Mantl, "New high-precision 5-axes RBS/channeling goniometer for ion beam analysis of 150 mm Ø wafers," Nuclear Instruments and Methods in Physics Research Section B: Beam Interactions with Materials and Atoms, vol. 161-163, pp. 227 - 230, 2000.

[44] A. Lambertz, T. Grundler, F. Finger, "Hydrogenated amorphous silicon oxide containing a microcrystalline silicon phase and usage as an intermediate reflector in thin-film silicon solar cells," J. Appl. Phys., vol. 109, p. 113109, 2011.

[45] C. Smit, R. A. C. M. M. van Swaaij, H. Donker, A. M. H. N. Petit, W. M. M. Kessels, M. C. M. van de Sanden, "Determining the material structure of microcrystalline silicon from Raman spectra," J. Appl. Phys., vol. 94, pp. 3582 - 3588, 2003.

[46] P. Hapke, "VHF-Plasmaabscheidung von mikrokristallinem Silizium: Einfluss der Plasmaanregungsfrequenzen auf die strukturellen und elektrischen Eigenschaften," Dissertation, RWTH Aachen, 1995.

[47] F. Köhler, "Zur Mikrostruktur siliziumbasierter Dünnschichten für die Photovoltaik," Dissertation, RWTH Aachen, 2013.

[48] http://gwyddion.net/documentation/user-guide-en/statistical-analysis.html, accessed 19 March 2015.

[49] J. M. Bennett, L. Mattson, "Introduction to Surface Roughness and Scattering", Optical Society of America, 1999.

[50] M. Pelliccione, T.-M. Lu, "Evolution of Thin Film Morphology - Modeling and Simulations", Springer, 2008.

[51] W. Reetz, H. Stiebig, and T. Brammer, "Spectral responce of stacked solar cells based on a-Si:H," Proceedings of the 2nd ISEC-Europe Solar Congress, Eurosun98, p. V.1.5-1, 1999.

[52]   J. Metzdorf, "Calibration of Solar cells. 1: The Differential Spectral Responsivity Method," Applied Optics, vol. 26, pp. 1701–1708, 1987.

[53]   A. Taflove, S. C. Hagness, "Computational Electrodynamics: The Finite-Difference Time-Domain Method," Artech House, 2005.

[54]   A. F. Oskooi, D. Roundy, M. Ibanescu, P. Bermel, J. D. Joannopoulos, S. G. Johnson, "MEEP: A flexible free–software package for electromagnetic simulations by the FDTD method," Comp. Phys. Comm., vol. 181, pp. 687 - 702, 2010.

[55]   A. Hoffmann, K. Bittkau, C. Zhang, T. Merdzhanova, U. Rau, "Coupling Incident Light to Guided Modes in Thin-Film Tandem Solar Cells with Intermediate Reflector", IEEE J. Photovoltaics, vol. 5, pp. 3 - 8, 2014.

[56]   A. E. Ermes, "Optical near-field investigations of photonic structures for application in silicon-based thin film solar cells," Dissertation, RWTH Aachen, 2015.

[57]   T. Grundler, A. Lambertz, F. Finger, "N-type hydrogenated amorphous silicon oxide containing a microcrystalline silicon phase as an intermediate reflector in silicon thin film solar cells," Phys. Status Solidi C, vol. 7, pp. 1085 - 1088, 2010.

[58]   V. Smirnov, A. Lambertz, B. Grootoonk, R. Carius, F. Finger, "Microcrystalline silicon oxide (μc-SiO$_x$:H) alloys: A versatile material for application in thin film silicon single and tandem junction solar cells," Journal of Non-Crystalline Solids, vol. 358, pp. 1954 - 1957, 2012.

[59]   A. Lambertz, V. Smirnov, T. Merdzhanova, K. Ding, S. Haas, G. Jost, R. Schropp, F. Finger, U. Rau, "Microcrystalline silicon–oxygen alloys for application in silicon solar cells and modules," Solar Energy Materials and Solar Cells, vol. 119, pp. 134 - 143, 2013.

[60]   P. Cuony, M. Marending, D. T. L. Alexander, M. Boccard, G. Bugnon, M. Despeisse, C. Ballif, "Mixed-phase p-type silicon oxide containing silicon nanocrystals and its role in thin-film silicon solar cells," Appl. Phys. Lett., vol. 97, p. 213502, 2010.

[61]   M. Kubon, E. Böhmer, F. Siebke, B. Rech, C. Beneking, H. Wagner, "Solution of the ZnO/p contact problem in a-Si:H solar cells," Solar Energy Materials and Solar Cells, vol. 41-42, pp. 485 - 492, 1996.

[62]   B. Rech, "Solarzellen aus amorphem Silizium mit hohem stabilem Wirkungsgrad: Zum Einfluss des p/i-Grenzflachenbereichs und der intrinsischen Absorberschicht", Forschungszentrum Julich, Zentralbibliothek, Forschungszentrum Jülich. Institut fur Schicht- und lonentechnik, Thesis-RWTH Aachen, 1997.

[63]   V. Smirnov, A. Lambertz, S. Tillmanns, F. Finger, "p- and n-type microcrystalline silicon oxide (μc-SiO$_x$:H) for applications in thin film silicon tandem solar cells 1," Can. J. Phys., vol. 92, p. 932 – 935, 2014.

[64]   J. Müller, O. Kluth, S. Wieder, H. Siekmann, G. Schöpe, W. Reetz, O. Vetterl, D. Lundszien, A. Lambertz, F. Finger, B. Rech, H. Wagner, "Development of highly efficient thin film silicon solar cells on texture-etched zinc oxide-coated glass substrates," Solar Energy Materials and Solar Cells, vol. 66, pp. 275 - 281, 2001.

[65]   K. Schwanitz, S. Klein, T. Stolley, M. Rohde, D. Severin, R. Trassl, "Anti-reflective microcrystalline silicon oxide p-layer for thin-film silicon solar cells on ZnO," Solar Energy Materials and Solar Cells, vol. 105, pp. 187 - 191, 2012.

[66]   A. Lambertz, F. Finger, B. Holländer, J. Rath, R. Schropp, "Boron-doped hydrogenated microcrystalline silicon oxide (μc-SiOx:H) for application in thin-film silicon solar cells," Journal of Non-Crystalline Solids, vol. 358, pp. 1962 - 1965, 2012.

[67]   S. Muthmann, F. Köhler, M. Meier, M. Hülsbeck, R. Carius, and A. Gordijn "Monitoring of the growth of microcrystalline silicon by plasma-enhanced chemical vapor deposition using in-situ Raman spectroscopy," Phys. Status Solidi RRL, vol. 5, pp. 144 - 146, 2011.

[68] K. Yamamoto, A. Nakajima, M. Yoshimi, T. Sawada, S. Fukuda, T. Suezaki, M. Ichikawa, Y. Koi, M. Goto, T. Meguro, T. Matsuda, M. Kondo, T. Sasaki, Y. Tawada, "A high efficiency thin film silicon solar cell and module," Solar Energy, vol. 77, pp. 939 - 949, 2004.

[69] J. Kuhs "Microcrystalline Silicon Oxide Alloys as Back Reflectors in Thin Film Silicon Solar Cells" Master thesis, Carl von Ossietzky Universität Oldenburg, 2014.

[70] J. Springer, A. Poruba, L. Müllerova, O. Kluth, B. Rech, "Absorption loss at nanorough silver back reflector of thin-film silicon solar cells," Journal of Applied Physics, vol. 95, pp. 1427 - 1429, 2004.

[71] U. Palanchoke, V. Jovanov, H. Kurz, P. Obermeyer, H. Stiebig, and D. Knipp, "Plasmonic effects in amorphous silicon thin film solar cells with metal back contacts," Opt. Express, vol. 20, pp. 6340 - 6347, 2012.

[72] V. Demontis, C. Sanna, J. Melskens, R. Santbergen, A. H. M. Smets, A. Damiano, M. Zeman, "The role of oxide interlayers in back reflector configurations for amorphous silicon solar cells," J. Appl. Phys., vol. 113, no. 6, p. 64508, 2013.

[73] M.N. van den Donker, B. Rech, R. Schmitz, J. Klomfass, G. Dingemans, and F. Finger "Hidden parameters in the plasma deposition of microcrystalline silicon solar cells," J. Mater. Res., vol. 22, pp. 1767 - 1774. 2007.

[74] S. Hänni, G. Bugnon, G. Parascandolo, M. Boccard, J. Escarré, M. Despeisse, F. Meillaud, C. Ballif, "High-efficiency microcrystalline silicon single-junction solar cells," Progress in Photovoltaics: Research and Applications, vol. 21, pp. 821 - 826, 2013.

[75] M. Boccard, M. Despeisse, J. Escarre, X. Niquille, G. Bugnon, S. Hanni, M. Bonnet-Eymard, F. Meillaud, C. Ballif, "High-Stable-Efficiency Tandem Thin-Film Silicon Solar Cell With Low-Refractive-Index Silicon-Oxide Interlayer," IEEE J. Photovoltaics, vol. 4, pp. 1368 – 1373, 2014.

[76] P. D. Veneri, L. V. Mercaldo, I. Usatii, "Improved micromorph solar cells by means of mixed-phase n-doped silicon oxide layers," Prog. Photovolt: Res. Appl., vol. 21, pp. 148 – 155, 2013.

[77] K. Ding, U. Aeberhard, F. Finger, and U. Rau, "Silicon Heterojunction solar cell with amorphous silicon oxide buffer and microcrystalline silicon oxide contact layers", Phys. Status Solidi RRL, vol. 6, pp. 193 - 195, 2012.

[78] P. Obermeyer, C. Haase, H. Stiebig, "Advanced light trapping management by diffractive interlayer for thin-film silicon solar cells," Appl. Phys. Lett., vol. 92, p. 181102, 2008.

[79] C. Rockstuhl, F. Lederer, K. Bittkau, T. Beckers, and R. Carius, "The impact of intermediate reflectors on light absorption in tandem solar cells with randomly textured surfaces," Appl Phys. Lett., vol. 94, p. 211101, 2009.

[80] S. Kirner, M. Hammerschmidt, C. Schwanke, D. Lockau, S. Calnan, T. Frijnts, S. Neubert, A. Schopke, F.Schmidt, J.-H. Zollondz, A. Heidelberg, B. Stannowski, B. Rech, R. Schlatmann, "Implications of TCO Topography on Intermediate Reflector Design for a-Si/μc-Si Tandem Solar Cells-Experiments and Rigorous Optical Simulations," IEEE J. Photovoltaics, vol. 4, pp. 10 - 15, 2014.

[81] N. Pellaton Vaucher, J.-L. Nagel, R. Platz, D. Fischer, A. Shah, "Light management in tandem cells by an intermediate reflector layer," Proceedings of 2nd WCPEC, 1998.

[82] D. Domine, J. Bailat, J. Steinhauser, A. Shah, "Micromorph solar cell optimization using a ZnO layer as intermediate reflector," Proceedings of 4th WCPEC, 2006.

[83] C. Rockstuhl, S. Fahr, K. Bittkau, T. Beckers, R. Carius, F.-J. Haug, T. Söderström, C. Ballif, and F. Lederer, "Comparison and optimization of randomly textured surfaces in thin-film solar cells," Optics Express, vol. 18, pp. A335-A341, 2010.

[84] A. Čampa, M. Meier, M. Boccard, L. V. Mercaldo, M. Ghosh, C. Zhang, T. Merdzhanova, J. Krč, F.-J. Haug, M. Topič, "Micromorph silicon solar cell optical performance: influence of intermediate reflector and front electrode surface texture" Solar Energy Materials and Solar Cells, 130, pp. 401 - 409, 2014.

[85] C. Zhang, M. Meier, A. Lambertz, V. Smirnov, B. Holländer, A. Gordijn, T. Merdzhanova, "Optical and Electrical Effects of p-type μc-SiOx:H in Thin-Film Silicon Solar Cells on Various Front Textures," International Journal of Photoenergy, vol. 2014, pp. 1 - 10, 2014.

[86] G. Jost, T. Merdzhanova, T. Zimmermann, J. Hüpkes, "Process monitoring of texture-etched high-rate ZnO:Al front contacts for silicon thin-film solar cells," Thin Solid Films, vol. 532, pp. 66 - 72, 2013.

[87] H. Zhu, J. Hüpkes, E. Bunte, J. Owen, S. Huang, "Novel etching method on high rate ZnO:Al thin films reactively sputtered from dual tube metallic targets for silicon-based solar cells," Solar Energy Materials and Solar Cells, vol. 95, pp. 964 - 968, 2011.

[88] M. Sever, B. Lipovšek, J. Krč, A. Čampa, G. Sánchez Plaza, F.-J. Haug, M. Duchamp, W. Soppe, M. Topič, "Combined model of non-conformal layer growth for accurate optical simulation of thin-film silicon solar cells," Solar Energy Materials and Solar Cells, vol. 119, pp. 59 - 66, 2013.

[89] M. Boccard, C. Battaglia, N. Blondiaux, R. Pugin, M. Despeisse, C. Ballif, "Smoothening intermediate reflecting layer for tandem thin-film silicon solar cells," Solar Energy Materials and Solar Cells, vol. 119, pp. 12 - 17, 2013.

[90] A. Hoffmann, "Light management by intermediate reflectors in silicon-based tandem solar cells," Dissertation, RWTH Aachen, 2015.

[91] A. Hoffmann, K. Bittkau, C. Zhang, M. Meier, R. Carius, U. Rau, "Photon Tunneling in Tandem Solar Cells with Intermediate Reflector," IEEE J. Photovoltaics. (under revision)

[92] M. Boccard, T. Soderstrom, P. Cuony, C. Battaglia, S. Hanni, S. Nicolay, et al., "Optimization of ZnO Front Electrodes for High-Efficiency Micromorph Thin-Film Si Solar Cells," IEEE J. Photovoltaics, vol. 2, pp. 229 - 235, 2012.

[93] F. Sánchez-Sinencio, R. Williams, "Barrier at the interface between amorphous silicon and transparent conducting oxides and its influence on solar cell performance," Journal of Applied Physics, vol. 54, pp. 2757 - 2760, 1983.

[94] F. A. Rubinelli, J. K. Arch, S. J. Fonash,"Effect of contact barrier heights on a-Si:H p-i-n detector and solar-cell performance," Journal of Applied Physics, vol. 72, pp. 1621 - 1630, 1992.

[95] W. Ma, T. Saida, C.C. Lim, S. Aoyama, H. Okamoto, Y. Hamakawa, "The utilization of microcrystalline Si and SiC for the efficiency improvement in a-Si solar cells," Photovoltaic Energy Conversion, Conference Record of the Twenty Fourth. IEEE Photovoltaic Specialists Conference, vol.1, pp. 417 - 420, 1994.

[96] M. Kubon, E. Boehmer, F. Siebke, B. Rech, C. Beneking, H. Wagner, "Solution of the ZnO/p contact problem in a-Si:H solar cells," Solar Energy Materials and Solar Cells, vol. 41/42, pp. 485 – 492, 1996.

[97] E. Böhmer, F. Siebke, H. Wagner "New insights into the ZnO/a-SiC:H(B) interface using XPS analysis," Fresenius' Journal of Analytical Chemistry, vol. 358, pp. 210-213, 1997.

[98] Reprinted from Publication J. E. Lee, J. H. Park, J.-S. Cho, J.-W. Chung, J. Song, D. Kim, J. C. Lee, "Analysis on the interfacial properties of transparent conducting oxide and hydrogenated p-type amorphous silicon carbide layers in p–i–n amorphous silicon

thin film solar cell structure," Thin Solid Films, vol. 18, pp. 6007 - 6011, 2012, with permission from Elsevier.

[99]   P.-K. Chang, F.-J. Tsai, C.-H. Lu, C.-H. Yeh, N.-F. Wang, M.-P. Houng, "Improvement of AZO/p-a-SiC:H contact by the p-μc-Si:H insertion layer and its application to a-Si:H solar cells," Solid-State Electronics, vol. 72, pp. 48 - 51, 2012.

[100] M. Bivour, S. Schröer, M. Hermle, "Numerical Analysis of Electrical TCO / a-Si:H(p) Contact Properties for Silicon Heterojunction Solar Cells," Energy Procedia, vol. 38, pp. 658 - 669, 2013.

[101] R. Rößler, "Transparente leitfähige Oxide (TCO) in Silizium-Heterostruktur-solarzellen: Elektronische Eigenschaften des TCO/a-Si:H Kontakts," Dissertation - Technische Universität Berlin, 2014.

[102] G. Yue, B. Yan, C. Teplin, J. Yang, S. Guha,"Optimization and characterization of i/p buffer layer in hydrogenated nanocrystalline silicon solar cells," Journal of Non-Crystalline Solids, 19-25, pp. 2440 - 2444, 2008.

[103] G. Bugnon, G. Parascandolo, S. Hänni, M. Stuckelberger, M. Charrière, M. Despeisse, F. Meillaud, C. Ballif, "Silicon oxide buffer layer at the p–i interface in amorphous and microcrystalline silicon solar cells," Solar Energy Materials and Solar Cells, vol. 120, pp. 143 - 150, 2014.

[104] J. Fang, Z. Chen, N. Wang, L. Bai, G. Hou, X. Chen, C. Wei, G. Wang, J. Sun, Y. Zhao, X. Zhang, "Improvement in performance of hydrogenated amorphous silicon solar cells with hydrogenated intrinsic amorphous silicon oxide p/i buffer layers," Solar Energy Materials and Solar Cells, vol. 128, pp. 394 - 398, 2014.

[105] B. Rech, C. Beneking, H. Wagner, "Improvement in stabilized efficiency of a-Si:H solar cells through optimized p–i-interface layers," Solar Energy Materials and Solar Cells, vol. 41–42, pp. 475 - 483, 1996.

[106] M. Python, E. Vallat-Sauvain, J. Bailat, D. Dominé, L. Fesquet, A. Shah, C. Ballif, "Relation between substrate surface morphology and microcrystalline silicon solar cell performance," Journal of Non-Crystalline Solids, vol. 354, pp. 2258 - 2262, 2008.

[107] D. Y. Kim, R. Santbergen, K. Jäger, M. Sever, J. Krč, M. Topič, S. Hänni, C. Zhang, A. Heidt, M. Meier, R. A. C. M. M. van Swaaij, M. Zeman, "Effect of Substrate Morphology Slope Distributions on Light Scattering, nc-Si:H Film Growth, and Solar Cell Performance," ACS applied materials & interfaces, vol. 24, pp. 22061 - 22068, 2014.

[108] H. B. Li, R. H. Franken, J. K. Rath, R. E. Schropp, "Structural defects caused by a rough substrate and their influence on the performance of hydrogenated nano-crystalline silicon n–i–p solar cells," Solar Energy Materials and Solar Cells, vol. 93, pp. 338 - 349, 2009.

[109] M. Boccard, C. Battaglia, S. Hänni, K. Söderström, J. Escarré, S. Nicolay, F. Meillaud, M. Despeisse, C. Ballif, "Multiscale transparent electrode architecture for efficient light management and carrier collection in solar cells," Nano letters, vol. 3, pp. 1344 - 1348, 2012.

Abbreviations and symbols

Abbreviation	Designation
A	absorptance
A	integrated area
α	absorption coefficient
ACL	autocorrelation length
AFM	atomic force microscopy
Ag	silver
AGC	Asahi Glass Company
AM	air-mass
APCVD	atmospheric pressure chemical vapor deposition
a-Si	amorphous silicon
a-Si:H	hydrogenated amorphous silicon
a-SiC:H	hydrogenated amorphous silicon
ASTM	American Society for Testing and Materials
B	boron
CCl_4	carbon tetrachloride
CdTe	cadmium telluride
CH_4	methane
CIGS	copper indium gallium selenide
CO_2	carbon dioxide
c-Si	crystalline silicon
d_{IRL}	thickness of IRL
DSR	differential spectral response
DT	double-textured
e^-	electron
E	photon energy
EELS	electron energy loss spectroscopy
E_c	conduction band energy
E_F	Fermi energy
EFTEM	energy filtered TEM

E_{osc}	oscillation energy
EPFL	École polytechnique fédérale de Lausanne
E_v	valence band energy
EQE	external quantum efficiency
$EQE_{top,\ 650nm}$	EQE value of top cell for λ = 650 nm
f	frequency
FDTD	finite-difference time-domain
FF	fill factor
ϕ_{H2}	H_2-flow
ϕ_{CO2}	CO_2-flow
ϕ_{SiH4}	SiH_4-flow
ϕ_{TMB}	TMB-flow
$\phi(\lambda)$	photon flux density
$\phi(x, t)$	Spatial and time dependent potential distribution
H	hydrogen
H+	hydron
He	helium
HHCF	height-height correlation function
HCl	hydrogen chloride
HF	hydrogen fluoride
HR-TEM	high Resolution Transmission Electron Microscopy
I	current
i	intrinsic
I_c	Raman intensity ratio
I_{dark}	dark current
I_{diode}	diode current
I_{ph}	photo current
IQE	Internal Quantum Efficiency
ITO	indium tin oxide
IRL	intermediate reflector layer
J	current density
J_0	saturation current density
J_{sc}	short-circuit current density
$J_{sc,\ EQE}$	integrated short-circuit current density from EQE
$J_{EQE,\ top}$	integrated short-circuit current density from EQE for top cell
$J_{EQE,\ bottom}$	integrated short-circuit current density from EQE for bottom cell

$J_{\text{EQE, total}}$	sum of sub cell $J_{\text{sc, EQE}}$
ΔJ_{EQE}	difference of $J_{\text{sc, EQE}}$ for tandem cell with and without IRL
J_{MPP}	current density at MPP
k	Planck constant
λ	wavelength
LA	large area
LPCVD	low pressure chemical vapor deposition
μ	mobility
μc-Si:H	hydrogenated microcrystalline silicon
μc-SiO$_x$:H	hydrogenated microcrystalline silicon oxide
MPP	maximum power point
n	refractive index
n	diode ideality factor
n_{IRL}	refractive index of IRL
ω	angular frequency
P	phosphorus
p	deposition pressure
(p)	p-type
ψ	power density
PC	process cambers
PDS	Photothermal Deflection Spectroscopy
PECVD	Plasma Enhanced Chemical Vapor Deposition
PH$_3$	phosphine
P_{MPP}	maximum power
q	elementary charge
R	reflectance
RBS	Rutherford Backscattering Spectrometry
ΔR	integrated difference between cell reflectance of tandem cells with and without IRL
r_{d}	deposition rate
RF	radio Frequency
$r_{O,RBS}$	oxygen/silicon ratio measured by RBS
r_{CO2}	CO$_2$/SiH$_4$ gas flow ratio
r_{PH3}	PH$_3$/SiH$_4$ gas flow ratio
r_{SiH4}	SiH$_4$/H$_2$ gas flow ratio
r_{TMB}	TMB/SiH$_4$ gas flow ratio

R_s	series resistance
R_{sh}	shunt resistance
$S(\lambda)$	spectral response
sccm	standard cubic centimeter
Si	silicon
SiH_3	silicon trihydride
SiH_4	silicon tetrahydride (silane)
SiO_x	sub-stoichiometric silicon oxide
$SnO_2{:}F$	fluorine-doped tin oxide
σ_{RMS}	root mean square roughness
T	transmittance
t	time
T	temperature
τ	lifetime
TEM	transmission electron microscopy
TMB	trimethylborane (B(CH3)3)
TCO	transparent conductive oxides
TRJ	tunnel-recombination junction
T_s	substrate temperature
UV-VIS-NIR	ultraviolet–visible–near-infrared
V	voltage
V_0	potential at RF-electrode surface
V_{MPP}	voltage at MPP
V_{oc}	open circuit voltage
V_p	plasma potential
x	stoichiometry number
x	spatial coordinate
xy-stretching	stretching in lateral 2D coordinates
xyz-stretching	stretching in 3D coordinates
z_M	average surface height
z-stretching	stretching in 1D coordinate (height)
ZnO:Al	aluminum doped zinc oxide
ZnO:B	boron doped zinc oxide

Curriculum Vitae

Personal details

Family name:	Zhang
Surname:	Chao
Date of birth:	February 7th, 1985
Place of birth:	Shaanxi, VR China
Nationality:	Germany

Education

1991 – 1995	Primary school: Gemeinschaftsgrundschule Nord in Jülich
1995 – 2004	High school: Siegtalgymnasium in Eitorf
2005 – 2011	University studies: "Environmental- and Bio Engineering Science" at Universität-Bayreuth with focus on biological and chemical process engineering
2012 – 2015	Ph.D. studies: thin-film silicon solar cells at Institut für Energie-und Klimaforschung IEK-5 in Jülich

List of publications

C. Zhang, M. Meier, A. Lambertz, V. Smirnov, A. Gordijn, T. Merdzhanova, "Development of P-Type µc-SiOx:H for Thin-Film Silicon Solar Cells on Sputtered ZnO:Al," 28th European Photovoltaic Solar Energy Conference Proceedings, pp. 2554 - 2557, 2013.

C. Zhang, M. Meier, A. Lambertz, V. Smirnov, B. Holländer, A. Gordijn, T. Merdzhanova, "Optical and Electrical Effects of p-type µc-SiO$_x$:H in Thin-Film Silicon Solar Cells on Various Front Textures," International Journal of Photoenergy, vol. 2014, pp. 1 - 10, 2014.

C. Zhang, M. Meier, A. Hoffmann, W. Zhang, K. Bittkau, G. Jost, U. W. Paetzold, A. M. Ermes, T. Merdzhanova, "Influence of Interface Textures on Light Management in Thin-Film Silicon Solar Cells With Intermediate Reflector," IEEE J. Photovoltaics, vol. 5, pp. 33 - 39, 2015.

C. Zhang, T. Merdzhanova, M. Meier, N. Sommer, O. Astakhov, "Impact of TCO Front Side Texture on the open-circuit voltage of a-Si:H Solar Cells" Physica Status Solidi (a), 213, pp. 1942-1948, 2016.

A. Čampa, M. Meier, M. Boccard, L. Mercaldo, M. Ghosh, C. Zhang, T. Merdzhanova, J. Krč, F.-J. Haug, M. Topič, "Micromorph Silicon Solar Cell Optical Performance: Influence of Intermediate Reflector and Front Electrode Surface Texture," Solar Energy Materials and Solar Cells, vol. 130, pp. 401–409, 2014.

D. Y. Kim, R. Santbergen, K. Jäger, M. Sever, J. Krč, M. Topič, S. Hänni, C. Zhang, A. Heidt, M. Meier, René A. C. M. M. van Swaaij, M. Zeman, "Effect of Substrate Morphology Slope Distributions on Light Scattering, nc-Si:H Film Growth, and Solar Cell Performance," ACS Appl. Mater. Interfaces, vol. 6, pp. 22061- 22068, 2014.

A. Hoffmann, U. W. Paetzold, C. Zhang, T. Merdzhanova, A. Lambertz, C. Ulbrich, K. Bittkau, U. Rau, "Advancing Tandem Solar Cells by Spectrally Selective Multilayer Intermediate Reflectors," Opt. Express, vol. 22, p. A1270, 2014.

A. Hoffmann, K. Bittkau, C. Zhang, T. Merdzhanova, U. Rau, "Coupling Incident Light to Guided Modes in Thin-Film Tandem Solar Cells With Intermediate Reflector," IEEE J. Photovoltaics, vol. 5, pp. 3-8, 2015.

A. Hoffmann, K. Bittkau, C. Zhang, M. Meier, R. Carius, U. Rau, "Photon Tunneling in Tandem Solar Cells with Intermediate Reflector," IEEE J. Photovoltaics, vol. 6, pp. 597-603, 2016.

L. V. Mercaldo, I. Usatii, E. M. Esposito, P. D. Veneri, J. W. Schüttauf, E. Moulin, F. J. Haug, C. Zhang, M. Meier, "Metal versus Dielectric Back Reflector for Thin-Film Si Solar Cells with Impact of Front Electrode Durface Texture," Progress in Photovoltaics, vol. 24, pp. 968-977, 2016.

Acknowledgements

Band / Volume 347
**On model and measurement uncertainty in
predicting land surface carbon fluxes**
H. Post (2016), xviii, 135 pp
ISBN: 978-3-95806-190-3

Band / Volume 348
Bipolarplattenmaterialien für Polymer-Elektrolyt-Membran Elektrolyse
M. Langemann (2016), I-III, 189, IV-XVIII pp
ISBN: 978-3-95806-192-7

Band / Volume 349
**Modellbasierte Ansteuerung räumlich ausgedehnter Aktuator-
und Sensornetzwerke in der Strömungsregelung**
M. Dück (2016), XIII, 153 pp
ISBN: 978-3-95806-193-4

Band / Volume 350
TRENDS 2015 – Transition to Renewable Energy Devices and Systems
ed. by D. Stolten and R. Peters (2016), 200 pp
ISBN: 978-3-95806-195-8

Band / Volume 351
**Dual Phase Oxygen Transport Membrane
for Efficient Oxyfuel Combustion**
M. Ramasamy (2016), VIII, 136 pp
ISBN: 978-3-95806-196-5

Band / Volume 352
**Transport, co-transport, and retention of functionalized
multi-walled carbon nanotubes in porous media**
M. Zhang (2016), VII, 112 pp
ISBN: 978-3-95806-198-9

Band / Volume 353
Untersuchungen zur Luftqualität in Bad Homburg
C. Ehlers, D. Klemp, C. Kofahl, H. Fröhlich, M. Möllmann-Coers
und A. Wahner (2016), IV, 93 pp
ISBN: 978-3-95806-199-6

Band / Volume 354
**Herstellung thermisch gespritzter Schichten
mit optimierten Spannungseigenschaften**
M. Mutter (2016), VI, 142, VII-XXII, xxvi pp
ISBN: 978-3-95806-200-9

Schriften des Forschungszentrums Jülich
Reihe Energie & Umwelt / Energy & Environment

Weitere *Schriften des Verlags im Forschungszentrum Jülich* unter
http://wwwzb1.fz-juelich.de/verlagextern1/index.asp

JÜLICH
FORSCHUNGSZENTRUM